Measurements of the K-shell Opacity in Solid-density Plasmas heated by an X-ray Free Electron Laser



Thomas Robert Preston

St. John's College

University of Oxford



A thesis submitted for the degree of

Doctor of Philosophy

Hilary Term 2017

Abstract

The advances achieved using X-ray Free Electron Lasers such as the Linac Coherent Light Source (LCLS), have revolutionised the routine production of uniform solid-density plasmas. Pulses of X-rays above 1 keV and with durations shorter than 100 fs attaining intensities on target of around $10^{17}\,\mathrm{Wcm}^{-2}$ are now routinely created. Through simple single-photon photoionization events with atoms in ambient solid conditions, it is possible to create uniform samples that are simultaneously hot, dense, and highly ionized which may be easily modelled.

This thesis describes measurements of the spectrally-resolved X-rays emitted from solid-density magnesium targets of varying sub-μm thicknesses isochorically heated by an X-ray laser. The data exhibit a thickness-independent source function, allowing the extraction of a measure of the opacity to K-shell X-rays within well-defined regimes of electron density and temperature, extremely close to Local Thermodynamic Equilibrium conditions by fitting to the simple 1D slab solution of the equation of radiative transfer. The deduced opacities at the peak of the K-α transitions of the ions are consistent with those predicted by detailed atomic-kinetics calculations.

The extracted opacities transpire to be robust to a plethora of variations in X-ray drive conditions, including the shape, pulse-length, and energy content. Furthermore the approximations in using the 1D slab solution are examined in detail and found to be good.

A full three-dimensional model of the plasma is advanced which includes attenuation, line-of-sight effects, full longitudinal and transverse gradients, and photon time-of-flight effects. The results from this model are found to also agree with the simpler 1D slab solution.

This novel method of elucidating opacities may complement other methods based on absorption and could be important for further benchmarking of opacities in solar-interior relevant conditions.

To Mum,
For making me who I am today.

Acknowledgements

> *No man is an Iland, intire of it selfe; every man is a peece of the Continent, a part of the maine;* – John Donne, Devotions upon Emergent Occasions, 1624

Whilst frequently an aphorism that all people are connected and dependent on other people, the original *Devotions* covered (near-)death, but more importantly rebirth. Both associations are apt.

Science at the cutting edge of laser experiments is intrinsically a collaborative process; this work would never have been achieved without the diligence and devotions of many people, and I should like take this opportunity to thank some of them here.

First and foremost I would like to thank my supervisor, Justin Wark, for his patience, the crucial (sometimes excitable) insights he has afforded, his wealth of knowledge, and his advice over the years. Furthermore, I would like to thank Orlando Ciricosta and Sam Vinko for their pioneering work that underpins this work, their assistance in getting to grips with SCFLY and modelling of data, and useful discussions cultivating my research. I would also like to thank Peter Norreys for his kind words and belief in me.

Much gratitude goes to those collaborators who were involved in the experimental campaign, especially our Czech collaborators, and the staff at SLAC. Furthermore, on the modelling aspects Hyun-Kyung Chung and Dick Lee, for their work on SCFLY which they have written and maintain.

In the Simon Room, that office eternally devoid of natural light, I thank Gavin Cheung for his *MATLAB* wizardry and cat calendar graffiti, and Patrick Hollebon for his unwavering willingness to talk about my research. Those who have been for many coffees with me over the last few years, outside of my immediate research group: Joe, both Alexs, Archie, Chris, and those who have come and gone, new and old, and those I've invariably

missed. Also, to those who never[1] show up: Naren, Luke, and (sometimes) Jimmy – your enthusiasm is infectious! It remains to say, I'm looking forward to working somewhere with windows.

Outside of physics, I would like to thank those who have lived with me, particularly Helen and Charlotte (as well as the whirlwind that is Jimmy), for enduring my complaints, feeding me, watering me, etc. You have been invaluable. Further, to Greg for his boundless knowledge of programming, and gentle exasperation at my efforts – I only wish I had the patience and wherewithal to learn to write code properly. To Marina for her kindness and support and Dean for conciliatory pints to moan about undergrad students. Special thanks goes to my three other musketeers: Duncan, Alex, and David; and all my other close friends from our Undergraduate days. On top of that, I am grateful to Alex and Nabil for reading the near complete manuscript, and of course to those who started reading but didn't make it to the end. Additionally, all the innumerable people I have met because of this degree at conferences and dinners and experiments. Essentially, if at any point we shared a drink – I am grateful you deemed me interesting enough to drink with.

Special gratitude goes to all my peers, tutors, and the staff at St. John's College. It has been my home for eight years and I will miss it. Furthermore, the boat club community past and present will also occupy a special place in my memories of this marvellous city.

Finally, to my family. To my mother for her enduring love and belief, her support and guidance, despite not having a clue what I do and why it matters; always remember that I'll do it so long as *I* know why. To my grandparents for their financial support throughout my University degrees, and glowing pride whatever happens. To Lucy and Alan, who despite their sheer bafflement with Physics, Maths, and all pursuits academic, still enjoy bragging to whoever will listen that they know me.

And last but not least[2] to Mikey for his encouragement. I still wish I had written that thesis on Laser cats; it might have been more colourful and interesting to a wider audience than this. Thanks for always reminding me that I am a strong, confident Kitty Cat.

[1] Citation needed.

[2] I lied when I said finally.

The author is grateful to AWE for support under the Oxford Centre for High Energy Density Science (OxCHEDS) collaboration. Portions of this research were carried out on the SXR Instrument at the Linac Coherent Light Source (LCLS), a division of SLAC National Accelerator Laboratory and an Office of Science user facility operated by Stanford University for the U.S. Department of Energy. The SXR Instrument is funded by a consortium whose membership includes the LCLS, Stanford University through the Stanford Institute for Materials Energy Sciences (SIMES), Lawrence Berkeley National Laboratory (LBNL), University of Hamburg through the BMBF priority program FSP 301, and the Center for Free-Electron Laser Science (CFEL).

Contents

Abstract i
Acknowledgements iii
List of Figures viii
List of Symbols and Acronyms x

1 Introduction **1**
1.1 X-ray Free Electron Lasers 1
1.2 Use of FELs to create solid-density plasmas 5
1.3 SCFLY - a super-configuration atomic-kinetics code 14
1.4 Structure of Thesis 19
1.5 Author Contributions 20

2 An experimental platform to benchmark hot-dense Opacities **22**
2.1 The need for a benchmark for hot-dense opacities 22
2.2 The advantages of using an X-ray FEL 27
2.3 Radiation Transport 33

3 Creation of Optically-Thin Solid-Density Plasmas using LCLS **39**
3.1 Experimental Setup 39
3.2 Data Analysis 40
3.3 Experimental Results 43
3.4 Zero-dimensional SCFLY simulations 54
3.4.1 Opacity 54
3.4.2 Source Function 59
3.4.3 Population evolution 61
3.4.4 Temperature and density evolution 68
3.5 Conclusions 71

4 Robustness of deduced Opacity to variations in conditions 73
4.1 Modifications to the X-ray drive . . . 73
4.1.1 Pulse shape . . . 74
4.1.2 Pulse length . . . 79
4.1.3 X-ray fluence . . . 84
4.2 Assumptions of the fit to Radiation Transfer . . . 88
4.2.1 Time-integration of the intensity . . . 88
4.2.2 Linear variations in the emissivity and opacity . . . 92
4.3 Conclusions . . . 97

5 Three-dimensional modelling of spectra 100
5.1 Geometric effects . . . 100
5.2 Three-dimensional SCFLY simulations . . . 106
5.2.1 Towards saturable absorption . . . 110
5.3 Photon Time-of-flight effects . . . 114
5.4 Conclusions . . . 117

6 Conclusions and Future Work 118
6.1 Summary and Conclusions . . . 118
6.2 Future Work . . . 122

A Derivation of limit as a linear variation in opacity tends to zero 125

Bibliography 127

List of Figures

1.1 Peak brightness of different light sources 3
1.2 K-α emission spectra of Aluminium 7

2.1 Contributions to solar opacity 24
2.2 Element of emitting and absorbing material interacting with a beam of radiation 36

3.1 Experimental setup 41
3.2 Shot-to-shot scatter 42
3.3 Experimental X-ray emission spectra for Mg 44
3.4 Photoionization and recombination chain 45
3.5 Normalised experimental emission spectra and fitted emissivity 50
3.6 Intensity as a function of thickness with 0D simulations 52
3.7 Fitted opacity and emissivity 53
3.8 Fitted opacity versus 0D integrated opacity 55
3.9 Fitted source function 60
3.10 Charge state distribution compared to LTE 63
3.11 Deviation from LTE conditions 65
3.12 Populations of higher charge states 66
3.13 Populations producing line VII 69
3.14 Mean temperature and density 71

4.1 Pulse shapes 75
4.2 Charge state distribution compared with flat pulse 77
4.3 Emission spectrum compared with flat pulse 78
4.4 Integrated opacity compared with flat pulse 79
4.5 Charge state distribution with changed pulse lengths 80
4.6 Emission spectra with changed pulse lengths 82
4.7 Integrated opacity with changed pulse lengths 84
4.8 Emission spectra with changed pulse energy 85

4.9 Integrated opacity with changed pulse energy 86
4.10 Effect of time-integration to functional form of the radiative transfer solution 90
4.11 Effect of linear variations in η and κ on the functional form of the radiative transfer solution 94

5.1 General schematic of geometry 103
5.2 Intensity as a function of thickness with 3D simulations 107
5.3 Comparison of conditions at front and back surface of target 109
5.4 Intensity as a function of thickness with 3D simulations and the laser intensity doubled 111
5.5 Fitted opacity versus 3D integrated opacity 112
5.6 Comparison of conditions at front and back surface of target with the laser intensity doubled 113
5.7 General schematic of photon time-of-flight geometry 115
5.8 Intensity as a function of thickness with 3D simulations and the laser intensity doubled including photon time-of-flight effects 116

List of Symbols and Acronyms

$\alpha(\nu)$	Photoionization cross-section
ϵ_0	Permittivity of free space
$\mathrm{erf}(x)$	Error function
γ	Lorentz factor
Γ_L	Natural broadening
κ_R	Rosseland mean opacity
λ_D	Plasma Debye Length
λ_u	Undulator period
$\mathrm{erfi}(x)$	Imaginary error function
$\overline{z}$	Mean charge state
θ_F	Inclination of FEL beam direction to normal: 45°
θ_S	Line-of-sight viewing angle: 20°
Ξ	Partition function
A_{ul}	Spontaneous radiative recombination rate (also A-rate)
$B(\nu, T)$	Planckian black-body function
B_0	Undulator peak magnetic field
c	Speed of light
d_S	Line-of-sight thickness: $d/\cos(\theta_S)$
e	Electron charge

f_{lu}	Oscillator strength
h	Planck's constant
K_0	Undulator magnetic deflection parameter
k_B	Boltzmann Constant
m_e	Electron mass
n_i	Ion density
T	Electron temperature
z	Charge state of ion
z^*	Degree of ionization: $\langle z_i^2 \rangle / \langle z_i \rangle$
A	Auger recombination process
AR	Radiative recombination process
CCD	Charge Coupled Device
CR	Collisional recombination process
DAQ	Data Acquisition Software
DFT	Density Functional Theory
EK	Ecker and Kröll
FEL	Free Electron Laser
FWHM	Full-Width-Half-Maximum
GMD	Gas Monitor Detector
HDM	Hot Dense Matter
HWHM	Half-Width-Half-Maximum
ICF	Inertial Confinement Fusion
IPD	Ionization Potential Depression
KBO	Kirkpatrick-Baez Optics

KL	Radiative recombination process
LCLS	Linac Coherent Light Source
LLNL	Lawrence Livermore National Laboratory
LTE	Local Thermodynamic Equilibrium
MEC	Matter in Extreme Conditions instrument
NIF	National Ignition Facility
PI	Photoionization process
SASE	Self-Amplified Spontaneous Emission
SP	Stewart and Pyatt
SXR	Soft X-ray material science instrument
XFEL	X-ray Free Electron Laser
XUV	Extreme Ultraviolet

Chapter 1

Introduction

This thesis exemplifies some of the work performed by the author on spectroscopic measurements of the opacity from ultra-thin Mg targets heated using X-ray pulses from a Free Electron Laser. As such it is a modest contribution to the pioneering first experiments using hard X-rays on these machines. This introductory chapter describes X-ray Free Electron Lasers, their operation, and relevance to the work in this thesis. Then, previous work using X-ray FELs to isochorically heat matter, that predicates the work in this thesis, are described in some detail. The structure of the rest of this thesis is outlined as well as the contributions of the author and others to the work presented herein.

1.1 X-ray Free Electron Lasers

The advances achieved through 4th generation light-sources, known as X-ray Free Electron Lasers, have revolutionised the routine production of uniform solid-density plasmas by creating pulses of X-rays above 1 keV and with durations shorter than 100 fs attaining intensities on target of around $10^{17}\,\mathrm{Wcm}^{-2}$. Now it is possible to create uniform samples that are simultaneously hot, dense, and highly ionized through simple single-photon photoionization events with atoms in ambient solid conditions.

The intensities are such that each atom may absorb many photons throughout the laser pulse, before any hydrodynamic expansion occurs and can allow a probing of these dense plasmas on short femtosecond timescales similar to the evolution of its thermodynamic properties, and fundamental electronic interaction processes such as collisional ionization or Auger decay.

To date there are four operating Free Electron Lasers in use, the first being the Free Electron LASer in Hamburg (FLASH), Germany in 2005 [1, 2] which operates in the extreme ultraviolet (XUV) region, followed by the Linac Coherent Light Source (LCLS) in Stanford, USA in 2009 [3, 4] which was the first truly hard X-ray FEL. The experiments described in this thesis were performed at LCLS and the focus of this section will be this machine and its unique attributes that facilitated this research. Further, there is another XUV FEL named FERMI in Trieste, Italy [5], and an X-ray FEL named SACLA in Kouto, Japan [6] which achieved first lasing in 2010. These will be complemented later in 2017 by both the European XFEL in Hamburg, Germany [7], and the SwissFEL in Würenlingen, Switzerland [8], which achieved lasing in the XUV (at 24 nm) at the end of 2016. Finally, the PAL-XFEL in Pohang, South Korea [9] achieved lasing in hard X-rays (0.15 nm) at the end of 2016. A selection of light sources are shown in Fig. 1.1.

Lasing in the X-ray regime is accomplished by forcing relativistic electrons from a linear accelerator (linac) to pass through a periodic transverse magnetic field, called an undulator, and was first envisioned as a concept in 1971 [10]. These oscillating electrons then emit stimulated bremsstrahlung at a resonant wavelength λ along the longitudinal axis [11]:

$$\lambda = \frac{\lambda_u}{2\gamma^2}\left(1 + \frac{K_0^2}{2}\right), \tag{1.1}$$

where λ_u is the period of the undulator and is 3 cm for LCLS [4], γ is the electron's gamma-factor defined as the ratio of the electron's energy to its rest energy, and K_0 is the dimensionless undulator magnetic deflection parameter and for LCLS is 3.5. It

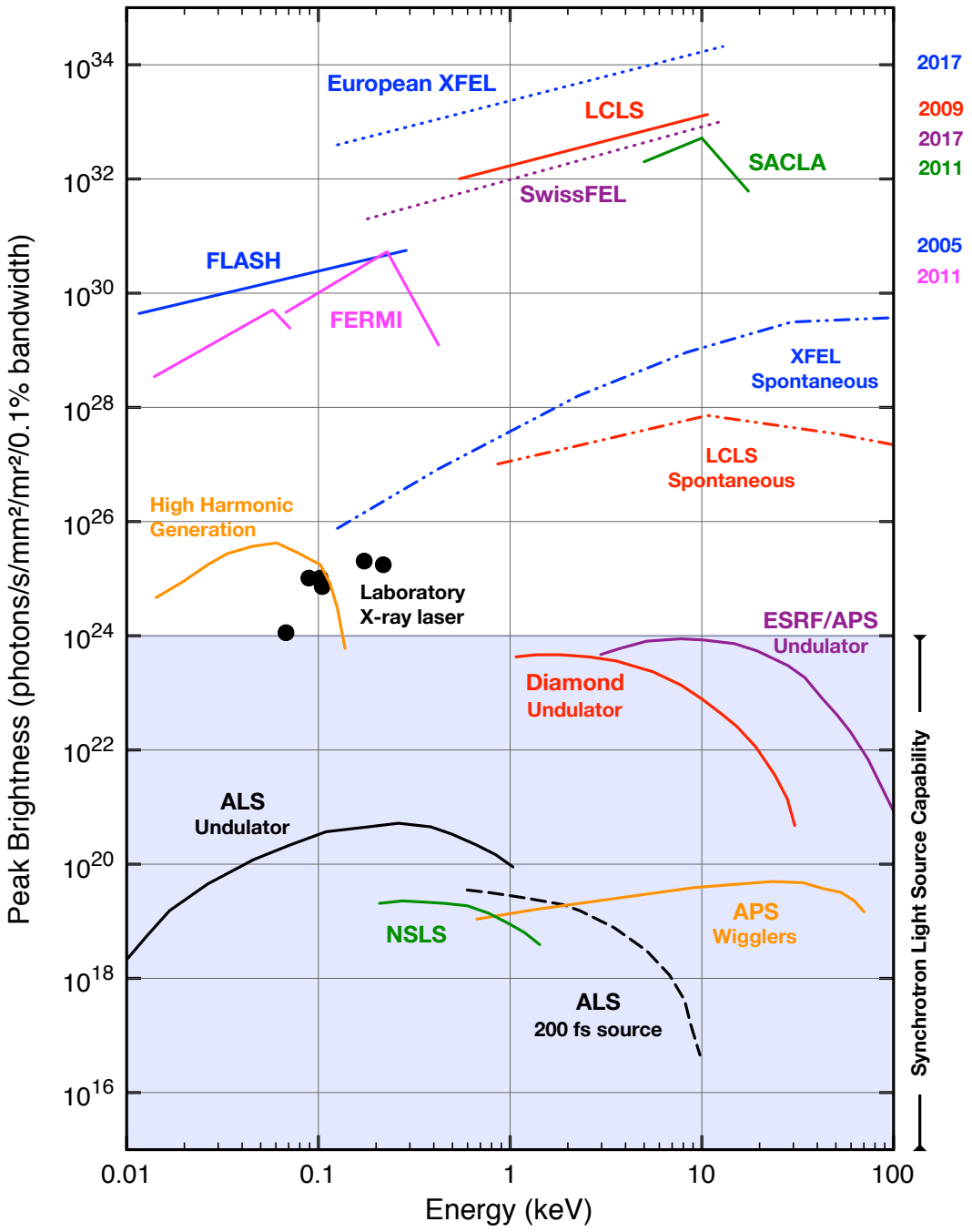

Figure 1.1: A plot of peak brightness versus XUV or X-ray energy for a number of different light sources. The lower portion lists synchrotron light sources (third generation light sources) and the limit of their capability. The upper part includes high harmonic generation, laboratory X-ray lasers, and fourth generation light sources comprised of a linac and undulator. To date only the European XFEL and SwissFEL are not yet operational; the year on the right corresponds to the start of that light source's operations. Note that the SwissFEL has lased in soft X-rays at an energy of $\sim 50\,\mathrm{eV}$. Reproduced courtesy of S. M. Vinko.

is defined as a function of the peak magnetic field:

$$K_0 = 0.934 B_0 \lambda_u, \tag{1.2}$$

with B_0 measured in Tesla and λ_u in cm [11]. For LCLS $B_0 = 1.25\,\mathrm{T}$ [4].

Much of the FEL's utility derives from the ability to tune the energy of the incoming electron bunch and correspondingly tune the wavelength of the emitted X-ray radiation that emerges from the undulator. However, the provenance of the nine orders of magnitude jump in peak brightness, as compared with a synchotron light source detailed in Fig. 1.1, that enables the experiments in this thesis, is the use of a sufficiently bright electron beam and sufficiently long undulator allowing an FEL to exhibit high-gain. In this regime the interaction of the electrons with their emitted X-rays leads to microbunching, essentially where the faster electrons catch up with the slower electrons, and the microbunched beam emits coherent radiation [11]. An input seed signal may be amplified exponentially along the 132 m of undulator [4] at LCLS without the requirement for any optical cavities or a highly ionized plasma as a gain medium [12]. Indeed, even the spontaneous undulator radiation can be amplified into intense quasicoherent radiation by what is known as Self-Amplified Spontaneous Emission (SASE process) [13, 14, 15].

The Linac Coherent Light Source is a remarkable machine and reaches saturation in the undulator, producing through the SASE process short pulses of X-rays from 280 eV to 10 keV at pulse energies from 0.1-3 mJ depending on the length of the electron bunch. The addition of a high brightness electron injector and two bunch compressors to the old Stanford Linear Accelerator allows the routine creation of high quality GeV electron bunches, with a tunable length in the range 10-100 fs, and a high peak current before injection into the undulator at a repetition rate of 120 Hz [4]. Future work envisages the use of sub-100 attosecond pulses by chirping

the electron bunch [16].

The X-rays are delivered to one of six end-stations (instruments) with different diagnostics and operating ranges; the instrument that is relevant to the work in this thesis is the Soft X-ray Material Science (SXR) which accepts X-ray photons from 280 eV to 2 keV – ideal for probing the K-edges of low atomic number (low-Z) materials and heating them into the Hot Dense Matter (HDM) regime. It should be noted here that the instrument specifically designed for HDM studies is MEC (Matter in Extreme Conditions) with an operating range of 4-10 keV – much too high to probe the K-edges of the simple-structured low-Z elements investigated in this thesis. More details specifically about the SXR end-station may be found in Schlotter et al. [17].

It remains now to discuss what exactly is Hot Dense Matter and how LCLS may be used to heat materials to phenomenal temperatures in a fraction of a second.

1.2 Use of FELs to create solid-density plasmas

Hot Dense Matter is characterised by its high density, of the same order as the ambient solid ($\sim 1\,\mathrm{gcm}^{-3}$) with ion densities $n_i \sim 10^{23}\,\mathrm{cm}^{-3}$, and high temperatures of order 100 eV. They pose a difficult problem to model since, unlike an ideal plasma, at these high densities the inter-particle Coulomb interactions are comparable to the thermal energy [18] which is itself also very large. They therefore also cannot be treated with a solid state theory approach either.

Two examples where HDM is relevant are Inertial Confinement Fusion ICF studies [19, 20] and in the interiors of stars. As will become clear later, the ability to accurately model the opacity properties of the hohlraum walls, usually manufactured from gold [21], is crucial for the indirect-drive approach to fusion. Furthermore the convection zone/radiative zone boundary in the sun is of profound interest for its heat conduction, radiation transport and models for its evolution and structure [22, 23].

Additionally, models of its opacity, accurately engendering all its complexities, are in high demand [24, 25, 26]. These will be discussed in much more detail in Ch. 2.

Since 2012, a new use for X-ray Free Electron Laser was found: the "Creation and diagnosis of a solid-density plasma with an X-ray free-electron laser" [27]. In this work, the authors create, in a highly repeatable way, an aluminium plasma at temperatures in excess of 10^6 K on timescales over which it remains inertially confined. The authors tuned the FEL to energies at and above the cold Al K-edge, training 10^{12} photons per 80 fs long pulse into a small spot of 9.1 μm^2. As the incoming photon energy is tuned, K-α emission from successively higher charged ions is observed arising from a dense system. Their recorded emission spectrum is reproduced in Fig. 1.2 and shows the emergence of emission from higher states as the FEL energy increases. These charge states are labelled above the plot of Fig. 1.2 according to their ionization stage [28]. The emission from single K-shell holes and double K-shell holes are labelled as well as the line corresponding to resonant transitions.

The K-shell is the innermost atomic shell ($n = 1$) which only contains an s-orbital ($1s$), whilst the L-shell corresponds to the $n = 2$ shell which has an s-orbital and p-orbital ($2s$ and $2p$). The use of an FEL preferentially[1] photoionizes a K-shell electron creating a hollow atom with a vacancy in its K-shell (a single K-shell hole) when probed above the material's cold K-edge. If another K-shell electron is photoionized before the first vacancy is filled then the ion of interest will have a double K-shell hole. Emission is recorded from the filling of these vacancies with an electron from the L-shell ($2p - 1s$ transitions). A set of separate transitions exist, labelled as resonant transitions, where the FEL excites an electron from the K-shell to the L-shell and the spontaneous emission from filling this hole is recorded with the same energy.

As the FEL photon energy is increased the K-α lines from successively higher charge states appear as ionization thresholds, known as K-edges, are crossed. The

[1] L-shell electrons are also photoionized by X-rays near the K-edge, but with a lower cross-section.

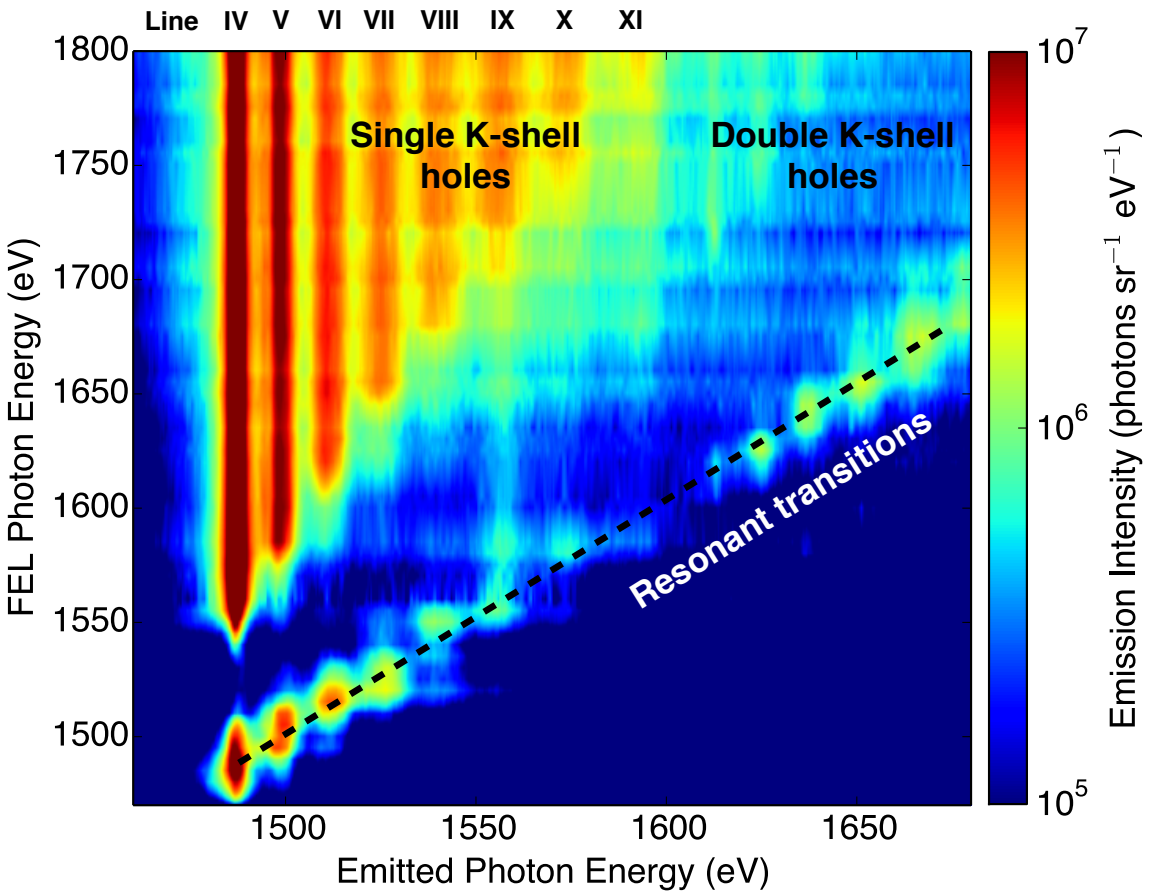

Figure 1.2: A plot of K-α emission spectra from Al at different pump FEL photon energies. The colour bar on the right indicates the emission intensity on a logarithmic scale. Labelled are single K-shell holes, double K-shell holes, and resonant transitions. As the FEL energy is increased K-shell electrons from successive higher charge states can be photoionized leading to higher energy K-α lines. Reproduced from Vinko [29].

position of these edges transpires to be very important, and further work shows that the choice of model for the Ionization Potential Depression (IPD), or Continuum lowering is crucial to accurately calculate their positions [30]. Continuum lowering is an environmental effect on the electrostatic potential of an ion in a plasma. Due to the interaction with surrounding particles, both ions and electrons, the threshold required to ionize an electron is reduced compared with an isolated ion. The amount that the ionization potential is reduced is known as the IPD. As a simple example, consider aluminium: in the ambient solid the outermost three electrons, which for the isolated ion would occupy the M-shell, are unbound and form a conduction band.

Ergo, the ionization potential for solid density Al is depressed sufficiently by the IPD that these states become part of the continuum.

The most commonly used model for the IPD is that set out by Stewart and Pyatt in Stewart and Pyatt, Jr. [31], hereafter SP. The details of their derivation are not reproduced here but essentially they consider the interaction of their ion of interest with other point ions and a time-averaged, spherically symmetric electron charge density. The resulting IPD may be expressed as:

$$\Delta I_{SP} = \frac{k_B T}{2(z^*+1)} \left\{ \left(\frac{3(z^*+1)ze^2}{4\pi\epsilon_0 \lambda_D k_B T} \right)^{2/3} - 1 \right\}, \tag{1.3}$$

where λ_D is the plasma Debye length including both electrons and ions [31, 32]. In this equation z indicates the charge state of the atom after the ionization process has taken place, i.e. $z = 1$ for the neutral atom. The degree of plasma ionization is determined by the parameter $z^* = \langle z_i^2 \rangle / \langle z_i \rangle$ where the brackets denote an average over all charge states z_i present in the plasma weighted with their populations and is determined by the specific temperature T and density of the plasma. Finally, e is the electronic charge, k_B is Boltzmann's constant, and ϵ_0 is the permittivity of free space.

The Debye length is the screening length in Poisson's equation for the electric potential $\Phi(\mathbf{r})$ (Gauss's law) and may be derived as follows. First, Poisson's equation is defined as:

$$\epsilon_0 \nabla^2 \Phi(\mathbf{r}) = -\sum_j q_j n_j(\mathbf{r}), \tag{1.4}$$

for discrete charges q_j with density n_j [33]. Separating the right hand side into ions with charge $z_j e$ and electrons with charge $-e$, the density of each is given by the Boltzmann distribution:

$$n_j(\mathbf{r}) = n_j^0 \exp\left(-\frac{q_j \Phi(\mathbf{r})}{k_B T} \right), \tag{1.5}$$

with n_j^0 the mean density of the species. The electronic density in the limit that $e\Phi(\mathbf{r}) \ll k_B T$, i.e. for a weakly coupled plasma is given by,

$$n_e\Big(1 + \frac{e\Phi(\mathbf{r})}{k_B T}\Big). \tag{1.6}$$

Similarly the weakly coupled ionic density is:

$$n_j^0\Big(1 - \frac{z_j e\Phi(\mathbf{r})}{k_B T}\Big). \tag{1.7}$$

Note that it is assumed that the ions and electrons are in thermal equilibrium, both at temperature T. The resulting Poisson-Boltzmann equation is:

$$\nabla^2\Phi(\mathbf{r}) = \frac{e^2 n_e \Phi(\mathbf{r})}{\epsilon_0 k_B T} + \sum_j \frac{z_j^2 e^2 n_j^0 \Phi(\mathbf{r})}{\epsilon_0 k_B T} + \frac{e n_e}{\epsilon_0} - \sum_j \frac{e z_j n_j^0}{\epsilon_0}. \tag{1.8}$$

Finally, assuming charge neutrality,

$$n_e = \sum_j z_j n_j^0, \tag{1.9}$$

the Poisson-Boltzmann equation may be expressed,

$$\nabla^2\Phi(\mathbf{r}) = \frac{\Phi(\mathbf{r})}{\lambda_D^2}, \tag{1.10}$$

defining the Debye length,

$$\lambda_D = \sqrt{\frac{\epsilon_0 k_B T}{e^2 n_e + \sum_j z_j^2 e^2 n_j^0}}, \tag{1.11}$$

as the screening length in the solution to Eqn. 1.10. Note, the classical Debye length including only electrons may be found by assuming in Eqn. 1.7 that the ions are stationary and so only given by n_j^0. The Debye length is then $\lambda_D = \sqrt{\epsilon_0 k_B T / e^2 n_e}$.

The SP formula for IPD in the weakly-coupled regime (high temperature and low density) reduces to that of Debye and Hückel [33]:

$$\Delta I_{DH} = \frac{ze^2}{\lambda_D}, \tag{1.12}$$

and in the strongly coupled regime to the ion-sphere model:

$$\Delta I_{IS} = \frac{3}{2}\frac{ze^2}{r_{IS}}, \tag{1.13}$$

where the ion-sphere radius is the radius of a sphere surrounding a central ion of charge z containing a uniform electron density, $r_{IS} = (3z/4\pi n_e)^{1/3}$.

Prior to the work of Stewart and Pyatt [31], another model was proposed by Ecker and Kröll [34], hereafter EK, that instead of the ion-sphere radius a more relevant length to determine IPD at high densities includes the ion density n_i as well, and is instead:

$$r_{EK} = \Big(\frac{3z}{4\pi(n_e + n_i)}\Big)^{1/3}. \tag{1.14}$$

Their IPD is then given by:

$$\Delta I_{EK} = C_{EK}\frac{ze^2}{r_{EK}}, \tag{1.15}$$

with the constant $C_{EK} = (r_{EK}/\lambda_D)_{n=n_c}$ defined at the critical density n_c to tie the solution of Eqn. 1.15 to the Debye-Hückel solution of Eqn. 1.12 at low density. The critical density is defined as [32]:

$$n_c = \frac{3}{4\pi}\Big(\frac{4\pi\epsilon_0 k_B T}{Z^2 e^2}\Big)^3, \tag{1.16}$$

where Z is the charge on the nucleus of the species under consideration, e.g. $Z = 13$ for Al.

Crucially, the two forms of the IPD in Eqns. 1.3 and 1.15 have different scalings

with respect to charge state z for a fixed temperature and density: the Stewart and Pyatt model predicts a scaling of $z^{2/3}$ compared with the larger z scaling for the Ecker and Kröll model.

Ciricosta et al. [30] found that by tuning through FEL energies, much like in Fig. 1.2, with a narrow bandwidth they were able to step through the charge states of Al and measure when an ionization threshold is reached, thus quite simply measuring the IPD. Their work found that the IPD scales with z and they were better able to model their data incorporating continuum lowering as described by Ecker and Kröll [34] albeit with a different constant $C_{EK} = 1$. This has profound and deep repercussions for the field of plasma physics more generally: previous work on hot plasmas driven by optically lasers almost ubiquitously modelled the continuum lowering using Stewart and Pyatt's model, such that it became an innate standard. Spectroscopic diagnosis of many laser-driven plasmas [35, 36, 37, 38] relies on the presence of higher order lines, for example β-lines ($3p - 1s$) or γ-lines ($4p - 1s$) which are optically-thin to infer temperature and density [39]. However, the additional scaling of $z^{1/3}$ in the EK model can result in the upper levels involved in these transitions being depressed out by the IPD. For example, in Al at temperatures in excess of 500 eV and densities greater than solid, the modified EK model (with $C_{EK} = 1$) predicts no recombination of the M-shell, whereas in the SP model the β-line transitions from the M-shell persist beyond 3 times solid density [32]. To summarise, knowledge of the IPD is crucial to define the number of bound states available in an atom as well as the charge state distribution (how ionized it is) and its temperature.

Much discussion was motivated by these results: β-lines were observed in very thin Al foils embedded in plastic and diamond which were compressed and heated to inferred temperatures of 600 eV and densities around 2 times solid density (6 gcm^{-3}) indicating better modelling of this plasma using the SP model [40, 41]. Although technically this measurement was made at conditions where the IPD is in the ion-

sphere limit of Eqn. 1.13, importantly it is inconsistent with the EK model.

There have been attempts to explain the difference between these incongruent results by including more excitations in the atomic model [42] and through discourse to Density Functional Theory (DFT), whereby the system is modelled self-consistently from first-principles accounting for the full quantum mechanical structure of the valence electrons [43], as well as a deluge of other work [44, 45, 46]. In the DFT model, the ionization potentials are calculated directly from the effect of the surrounding plasma on a central ion in a direct way without the need for an external model to correct the ionization potential as used in analytical approaches [43]. The amelioration of the two contravening results [30, 40] is achieved somewhat in this article, where the authors observe the formation of a quasi-atomic $3s$ line and the onset of atomic-like $3p$ features in the density of states as the temperature is increased in agreement with the work of Hoarty et al. [40], although they struggle to reach the same high temperatures as the computational costs balloon. A more complete treatment is achieved here since whether a state is bound or not due to IPD is no longer a binary feature as in the analytical models discussed above; the inevitable variance in the local distribution of charges surrounding an emitting ion are handled self-consistently as in a real plasma. Furthermore, whilst these quasi-atomic features appear, it is found that at over the entire temperature range that the LCLS data is taken (up to around 100 eV) they are not significantly populated and so would not affect the central ion of interest – only the bound K and L-shells affect this ion's viewed potentials – and the calculated IPDs match those found experimentally [30]. Interestingly, the radial density for electrons around the central ion at low temperatures looks similar to that of an atomic valence density, and as the temperature increases it tends towards the limit of an average valence density, where the electrons are not associated with any ions in particular and are homogeneously distributed. This corresponds well with the work on Orion at higher temperatures [40] where their IPDs matched the ion-sphere

formula which assumes a homogeneous electron density.

On the other hand, the inclusion of a bound M-shell with the SP model, as suggested by Iglesias [42], which allows the line positions to be modified by satellite lines with spectator M-shell electrons that could be misinterpreted as K-α lines from higher ionization states, is found to not offer an explanation for the data. This is because ionization and K-M resonant excitation have different signatures in the charge state distribution, absorption cross-sections and emission rates [47]. The result of this is that the emission spectra using the SP model do not match the line intensities for several emission peaks, and furthermore, the measured K-edge corresponds solely to K-shell ionization, and not to some combination of ionization and K-M resonant transitions. The authors note that "this is not a trivial observation, as there is no a priori reason nor requirement for the thresholds to be K-edges, and indeed in some IPD models (i.e., SP for high charge states) they are not" [47].

Finally, all of the above work using an FEL has considered continuum lowering as a function of temperature with the density set to be perfectly solid in its pure form. It is possible to also consider ions in different density regimes by using not only pure elements but also compounds of elements [48]. Here, the data set was extended by considering not only pure Mg, Al, and Si, but also compounds of Al_2O_3, SiO_2, and mica ($KAl_3Si_3O_{12}H_2$), which may be isochorically heated in the same way[2] but with the density around a factor of two lower. Using mixtures is found to make no difference to the K-edges matching neither of the two models discussed above which modulate the IPD with density. Instead, a "neutral atom approximation" is put forward where the edges are calculated simply by the following method. First, excited electrons (including the free electrons) are placed in the M-shell for an isolated (and consequently neutral) atom. Then the ionization energies are given by the K-M excitation energies. Since the M-shell is unbound and always lies in the continuum, this

[2]Note, the other elements (K, O, and H) have a low absorption cross-section around the K-edges of Al, Mg, and Si.

K-M excitation energy is always larger than the measured K-M ionization threshold. Subsequently, they conclude that this should be expected for a cold, solid-density material, where the atomic properties of the elements in a crystal determine the location of the valence band from the overlap of atomic orbitals on different sites [49]. And so there is strong evidence that this holds when the material is heated with the ions on their original lattice sites: the cold binding between, say, an Al ion and an O ion in a crystal is determined by their atomic binding energies and overlap of their valence bands, and is maintained regardless of subsequent heating. This corresponds well to the DFT treatment discussed earlier [43], where the radial electron density appears similar to the atomic valence band at low temperatures. Clearly as a function of temperature there is some transition point between these two regimes.

Finally, it is prudent to mention that whilst the above discussion has considered a few analytical models for the IPD, in tandem with a more complete treatment through DFT, none of these models should be believed as gospel as they do not capture the full physics over a wide range of temperatures and charge state. To quote Ciricosta et al. [30]: "both . . . models are simple, semiclassical models, ultimately both unlikely to capture fully the complex physics of atomic systems embedded within dense plasma environments over wide ranges of plasma conditions and charge states. However, . . . this work . . . ought to spur further efforts to produce more sophisticated self-consistent models of the IPD within dense plasmas".

1.3 SCFLY - a super-configuration atomic-kinetics code

Almost all of the modelling of spectra expatiated in the previous section relied on comprehensive modelling using the SCFLY atomic-kinetics code [50]. This is a collisional-radiative code based on the popular FLYCHK [51] simulation code but which has been

heavily modified to ensure its suitability to be applied to modelling problems using an X-ray FEL. The code is zero-dimensional and handles opacity effects using an escape factor formalism [52].

The work in this thesis will focus exclusively on magnesium which is a prime candidate for use with SCFLY. Much like the early work on Al [27], magnesium is also a prototypical metal with a simple atomic structure which in the ambient solid only has 10 bound electrons in two shells, the K and L-shell. The free electrons are unbound and form an electron gas which is well described by Fermi-Dirac statistics at low temperature; high electron densities and temperatures may be expeditiously obtained through heating with an X-ray FEL, allowing their statistics to be described by the Maxwell-Boltzmann distribution.

The procedure to generate emission spectra is split into two steps. First, the super-configuration[3] populations and plasma conditions (temperature, density, etc.) are calculated by SCFLY using a time-dependent X-ray pulse to drive the simulation and will be described in detail below. Next, at each output time-step, these super-configuration populations and plasma conditions are post-processed by the spectral module to calculate the emissivity, opacity, and an emission spectrum. Importantly, a more detailed set of atomic levels is used in the spectral module which provides the required level of detail to match the simulated emission spectrum to that observed experimentally. As an example, the He-like super-configurations are K^2L^0, K^1L^1, and K^0L^2, but the spectral module considers terms due to fine structure. Between the first two of these super-configurations, this would result in emission from a resonance line ($1s2p\ ^1P_1 - 1s^2\ ^1S_0$), and intercombination line ($1s2p\ ^3P_J - 1s^2\ ^1S_0$, where $J = 0, 1, 2$), as well as other 'forbidden' transitions involving a $2s$ electron.

Some key enhancements to SCFLY over FLYCHK in general are the following. Firstly, SCFLY uses super-configurations in order to make calculations tractable for

[3]These are described in more detail in Ch. 3.4.1.

mid-atomic number elements. The principal quantum number n is limited in SCFLY to be 10, but as discussed above higher orbitals will be depressed out by continuum lowering, and so for the work in this thesis only the K and L-shell ($n = 1, 2$) are required. The configurations are further extended by considering multiply-excited configurations with vacancies in the K-shell that are essential for modelling photoionization by X-rays. Further additions are the inclusion of autoionizing decay channels and dielectronic recombination (which is its inverse process). An example of a dielectronic recombination is:

$$K^2L^N + e^- \rightarrow K^1L^{N+1}X^1 \rightarrow K^2L^NX^1 + h\nu, \tag{1.17}$$

where an initial ground state K^2L^N with 2 electrons in the K-shell and N in the L-shell absorbs an electron into its X-shell (where X could be the L-shell, M-shell, N-shell, etc – any shell with a vacancy), and the excess energy is used to simultaneously excite another electron in the ion (in the case described from the K into the L-shell). In the second step, this doubly-excited ion relaxes to its ground state by emitting a photon $h\nu$. The transfer shown is for an electron moving down from the L-shell but the second step of Eqn. 1.17 could equally be achieved by the electron moving from the X-shell. FLYCHK also includes these processes, but does not allow modifications to the population of the K-shell (hollow atoms). At high densities, and with multiply excited ions, accurately modelling this decay channel can be extremely important, as the plasmas are highly collisional in their dynamics [53].

Specific to this work, the only bound shells are the K and L-shell because of the choice of model for continuum lowering [48] discussed above. Therefore the super-configurations used are: K^2L^N, K^1L^N, K^0L^N, where $N = 0 - 8$. Consequently, the only autoionizing channel open is Auger recombination from the L-shell (see Eqn. 3.2); all other choices for the X-shell described in Eqn. 1.17 are unavailable and

not included.

SCFLY has another benefit over FLYCHK in that it calculates entirely self-consistently the plasma evolution from an input X-ray pulse. This is simplified over optical laser experiments by the trivial relationship between absorption and modification of internal energy: a single photon is absorbed by an ion and its state changes through ionization or excitation.

A time-dependent non-LTE (Local Thermal Equilibrium) calculation is launched in the following way. First, the initial electron density $n(0)$, temperature $T(0)$ and population array $N_i(0)$ are specified at time $t = 0$ corresponding to the initial conditions of the material. For the case of interest here, the population array is initially populated with the ground state configurations of ions for a cold sample. The user also provides an X-ray pulse as an input in frequency and time $I(\omega, t)$. SCFLY calculates the number of available states n_{eq} up to a maximum principal quantum number accounting for continuum lowering – in this thesis the continuum lowering is calculated using the neutral atom model which provides an excellent match to data [48]. It also calculates the rates R_{ij} of all possible transitions between configurations as a function of the density, temperature, and X-ray pulse at that time. The system is allowed to then evolve to a time $t + dt$ by solving the n_{eq} coupled rate equations:

$$\frac{N_i(t+dt) - N_i(t)}{dt} = \sum_{j \neq i}^{n_{eq}} R_{ij} N_j(t) - N_i(t) \sum_{j \neq i}^{n_{eq}} R_{ji}, \tag{1.18}$$

where the summations are taken over all states j up to the maximum available state n_{eq} and the first term includes transitions from states $N_j(t)$ into $N_i(t)$ and the second term is transitions out of the state $N_i(t)$. The solution to Eqn. 1.18 yields the populations $N_i(t + dt)$.

For an isochorically heated plasma, where the ion density is fixed, the electron

density is found from:

$$n(t+dt) = \sum_{i=1}^{n_{eq}} N_i(t+dt) z_i, \tag{1.19}$$

where z_i is the ionization of the configuration i.

Each transition results in some transfer of energy $\epsilon_{ij}(t)$ and so the bulk energy transfer rate in a time step may be calculated from the rates and populations,

$$\frac{dE}{dt} = \sum_{j=1}^{n_{eq}} R_{ij} \epsilon_{ij} N_j, \tag{1.20}$$

at each time step. This allows one to then calculate the temperature:

$$\frac{3}{2} n(t+dt) k_B T(t+dt) = \frac{3}{2} n(t) k_B T(t) + \frac{dE}{dt} dt - \Delta E_{int}, \tag{1.21}$$

where ΔE_{int} is the difference in the internal energy stored in the ions as excitation or ionization of bound electrons simply obtained as a matter of accounting for the energy required to change a super-configuration's population in a time dt.

All of this together yields a new $[n(t), T(t), N_i(t)]$ with which to initialise another pass through Eqns. 1.18-1.21 and provides a completely self-consistent evolution in time.

Note that in the above, the ion temperature is not mentioned at all: this is because for the simulations in this thesis it is assumed to be fixed to the cold value, i.e. the absorption occurs on timescales significantly faster than the electron-phonon coupling time [54]. SCFLY is also able to handle expanding plasmas, where the ion (or mass) density changes and for systems where the ion temperature is the same as the electron temperature. It is also assumed as a matter of simplicity that the electrons thermalise immediately [47] which transpires to be a reasonable assumption (see Ch. 2.2), and that there is no loss or hydrodynamic motion of material. The code has also been further modified for the work on compounds [48] to solve the rate

equations simultaneously for multiple materials.

1.4 Structure of Thesis

A detailed commentary on all the work undertaken by the author during his D. Phil. would be difficult and not least quite tedious; instead this thesis attempts to focus on one aspect of it elucidated by its title. The cornerstone of this thesis is an experiment taken on ultra-thin foils of magnesium at LCLS and the use of spectroscopy to perform measurements of the opacity from these targets. The work is organised into six chapters arranged in the following way.

Chapter 1 introduces previous experimental campaigns to isochorically heat matter using an X-ray FEL. It first characterises the concept of an FEL and how ultra-bright X-ray pulses may now routinely be created. This is then augmented by linking into an X-ray FEL's utility for isochorically heating matter on rapid timescales. Previous scientific achievements using this method are described in detail, as well as the non-LTE code used to accurately model these exotic plasmas. The author of this thesis participated in some of this previous work, and is an author on Refs. [32, 47, 48, 53]. This chapter ends with this structural description and an outline of the author's contribution to each aspect of this thesis.

Chapter 2 introduces the historical need to benchmark hot-dense opacities and the scientific rationale behind a campaign since the earliest observations of solar plasmas. It then segues into why using an FEL may complement these earlier approaches using optical lasers and how many of the caveats of the historical approach can be overcome. It also includes an explanation of how radiation transport will be handled in the later chapters.

Chapters 3 to 5 are the core of the work presented in this thesis. Chapter 3 describes the experiment on ultra-thin Mg foils and data obtained using K-α spec-

troscopy. A fit using the solution to the radiation transfer equation is introduced and an opacity inferred from this which then matches zero-dimensional modelling of the plasma using SCFLY. Details of the modelling are examined and their specific relevance discussed. The results from this chapter have been submitted for publication in *Physical Review Letters*.

Chapter 4 examines the robustness of this technique of measuring opacities under a number of different variations in conditions. It examines the consequences of modifying the X-ray drive both temporally and in energy content. It also identifies the fundamental assumptions to the fit described in chapter 3.3 and comments on their effectiveness and robustness under variations in the fit parameters.

Chapter 5 presents modelling of the spectra using a three-dimensional model. Specifically, geometric and attenuation effects are identified and a model built to post-process an array of zero-dimensional simulations into a more detailed model. This model is further extended to include photon time-of-flight effects.

Finally, chapter 6 concludes this thesis with a summary of the work presented, what one may conclude from it, and discusses contemporaneously related work, and future work relevant to this thesis.

1.5 Author Contributions

Experiments performed at large user facilities such as the X-ray FEL at LCLS are notoriously complex and require a sizeable collaboration. The distinct contributions made by the author can be identified and are outlined in detail here, as well as the specific and relevant contributions from collaborators.

All the SCFLY simulations described in this thesis were performed by the author. Whilst that may be so, they were dependent on the prior efforts of others. The SCFLY code was written by R. W. Lee, and H-.K. Chung, with modifications to

solve for mixtures by O. Ciricosta; their assistance in using this code and fixing bugs has been invaluable. The recipe to process individual simulations into an accurate model of the target is due to O. Ciricosta and is described in Ciricosta et al. [47]. The concept for the three-dimensional model of chapter 5 is based on a program written by D. S. Rackstraw published in Rackstraw et al. [55]; although the specific formulation of the model used in this thesis should be attributed to the author as it was written from scratch by the author.

The author was involved in experimental work upon which this thesis hinges at every stage, from preliminary simulations for the proposal, through to execution, and processing of raw data into spectra. Some of the basic library routines written to process data from the experiment were written by collaborators at LCLS (US), though more specific data processing of CCD images of spectra was originally written by O. Ciricosta and S. M. Vinko. The author heavily modified their routines, rewriting some of them, in order to automate the process and improve the precision that individual shot-to-shot images may be straightened and spectra obtained. All processing of images into spectra and energy calibration from this experimental campaign was performed by the author.

The interpretation of results in chapters 3 to 5, driven by the author's processing of raw data in spectra, and work modelling the data using SCFLY simulations, is the culmination of detailed discussions between the author and O. Ciricosta, S. M. Vinko, and J. S. Wark: to attribute individual ownership of ideas would be exceedingly difficult and improprietous. Their contribution was vital to the advancement of this thesis, and should be attributed equally.

Chapter 2

An experimental platform to benchmark hot-dense Opacities

2.1 The need for a benchmark for hot-dense opacities

Historically, there has been a strong impetus to characterise opacities of plasmas at solar-interior relevant conditions [56], not only for modelling stellar interiors, but also inertial confinement fusion [19, 20], and plasmas created using Z-pinches such as the Z Facility at Sandia National Laboratories [57]. Most previous work has focussed on mid-atomic number (mid-Z) elements such as iron [58, 59], germanium [60], or gold [21] in the 100-300 eV temperature range, however atomic models for these ions are complex owing to the colossal number of transitions that must be accounted for.

The frequency-resolved opacity is in general a rapidly varying process. Just concentrating on the Sun as an example, in a typical window of interest where the change in emission with respect to temperature is large (the weighting function dB/dT defined in Eqn. 2.1), there are contributions to the opacity from a range of free-free (inverse bremsstrahlung), bound-free (such as edges, photoionization etc), and bound-

bound (internal atomic transitions) processes for a plethora of different elements, some of which are unimportant to the opacity, and some which are very important. A diagram explaining some of these processes and the contributions of hydrogen, oxygen, and iron to the frequency-resolved opacity is shown in Fig. 2.1. Clearly, the free-free opacity dominated by hydrogen is only important at low frequency, and at higher frequencies the K-edge of oxygen and a forest of L-shell bound-bound transitions in iron dominate its features. Evidently, opacities of mixtures must be understood in terms of their individual contributions in isolation, as well as the combination of the effects scaled by their abundances. Using oxygen as a pertinent example, its mass fraction is less than 1% that of hydrogen (estimated from spectroscopy and meteorite analysis [61]), yet its contribution to the Rosseland mean opacity is roughly a quarter as it is not fully ionized [62]. For iron, there is much structure around 500 eV but it is swamped by the contributions from hydrogen and oxygen. If one is to accurately constrain stellar abundances of "metals" (all elements other than H an He), and fully understand their contribution to stellar processes, then clearly one needs accurate benchmark measurements of their individual opacities in very controlled conditions. Going deeper than just the total abundance, another application of the frequency-resolved opacity is radiative levitation of metals in stars, which may give rise to surface abundance anomalies [63]. Given that for some applications it is necessary to have detailed knowledge of the frequency resolved opacity, it is judicious to measure this in benchmark experiments.

Fortuitously, simulations of photon transport may be performed without discourse to a detailed spectral model. A simple estimate of the opacity may be made from the Rosseland mean opacity κ_R defined as the weighted mean of the inverse opacity [33]:

$$\frac{1}{\kappa_R} = \int_\nu \frac{1}{\kappa(\nu)} \frac{dB}{dT} d\nu \Big/ \int_\nu \frac{dB}{dT} d\nu, \tag{2.1}$$

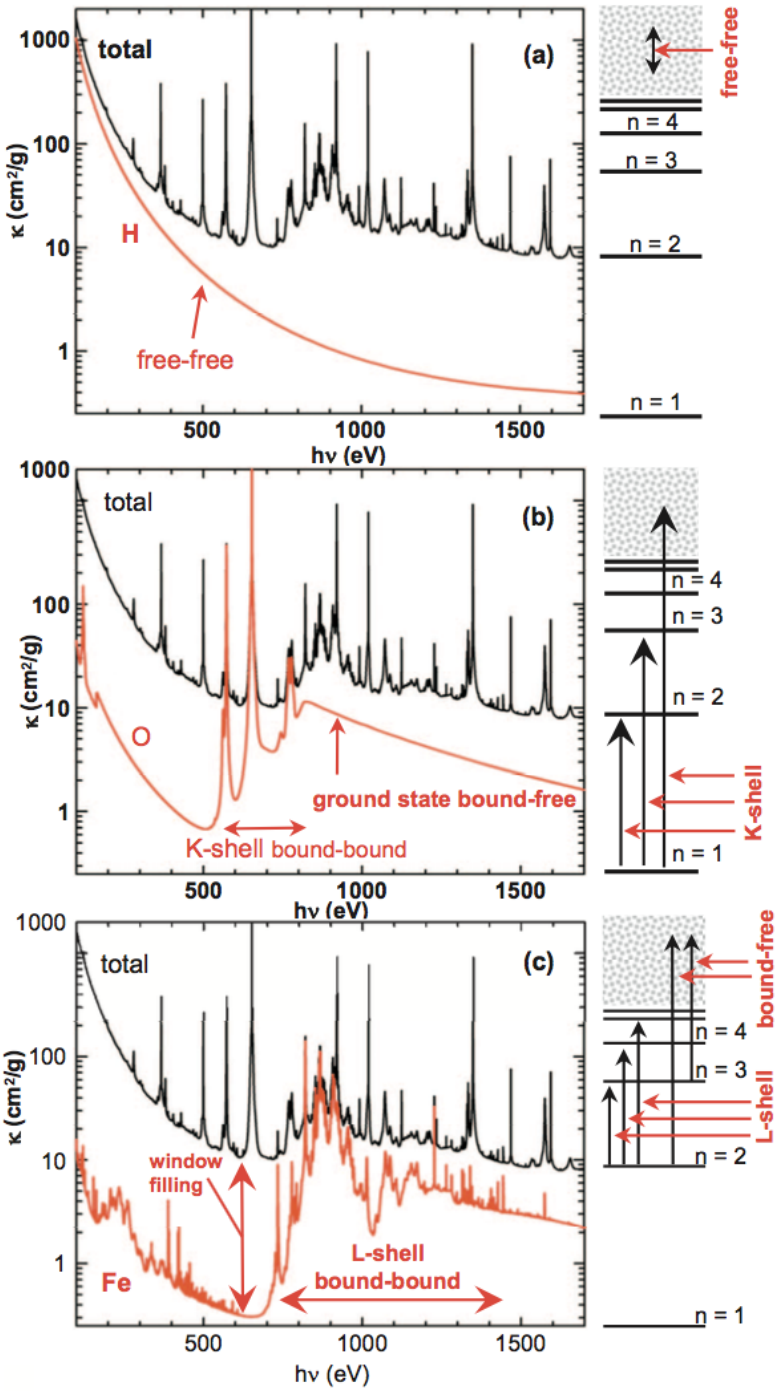

Figure 2.1: The contributions of the free-free opacity of hydrogen; K-shell bound-bound and K-edge bound-free opacity of oxygen; and L-shell bound-bound opacity of iron to the frequency-resolved solar opacity at conditions relevant to the base of the solar convection zone. Reproduced from Bailey et al. [62].

where $\kappa(\nu)$ is the opacity as a function of frequency ν and the weighting function is the derivative of the Planck function $B(\nu, T)$ with respect to temperature T. Planck's law is defined as:

$$B(\nu, T) = \left(\frac{2h\nu^3}{c^2}\right)\left[\exp\left(\frac{h\nu}{k_B T}\right) - 1\right]^{-1}, \tag{2.2}$$

where h is Planck's constant, c the speed of light, and k_B is Boltzmann's constant [64]. Whilst much of the physics of the frequency-resolved opacity $\kappa(\nu)$ are lost in using this harmonic mean, it transpires to be irrelevant for most simulations of photon transport; individual opacity models may reproduce the same solar Rosseland mean opacity with wildly different frequency-resolved opacities, but fortunately most of the important results for photon transport are the same [65].

Previous work in the field of opacity measurements has relied on achieving volumetrically uniform plasmas on macroscopic scales through use of low-Z (for example CH) tamper layers which are uniformly heated, for example by using a Hohlraum [21, 66]. Once the material of interest attains the required conditions it is imaged using a sufficiently bright X-ray backlighter in order to swamp the plasma's self-emission. Two spectra are recorded, the first attenuated through the tamper layers not containing the sample of interest $I_0(\nu)$, and the second through all layers including the sample $I(\nu)$. The backlighter should be chosen to be as uniform (Planckian) as possible and the tamper layer is chosen to be low-Z so that it will apply minimal features in the region of interest. The frequency-resolved intensities in the two cases may be compared to give opacity per unit mass $\kappa_\rho(\nu)$, usually measured in units of $\mathrm{cm^2 g^{-1}}$, by solving:

$$I(\nu) = I_0(\nu)\, \exp(-\kappa_\rho(\nu)\rho x), \tag{2.3}$$

where ρ is the mass density, and x is the line-of-sight optical path through the plasma. The transmission $I(\nu)/I_0(\nu)$ as a function of frequency is usually quoted as the figure of merit in these studies.

One limitation of this method is the availability of bright, uniform X-ray backlighters. In early pioneering work by Foster et al. [60], this was achieved by focussing a short-pulse ($< 200\,\mathrm{fs}$) Nd-glass laser down onto a small "glass fiber target" which had been coated with a high-Z element. The timing of the firing of this is chosen such that the target of interest, in this case Germanium, has attained the required temperature and density at the moment it is backlit. The novelty of this method relied on the creation of a short-duration, near-point backlighting source in order to take advantage of point-projection-spectroscopy [67].

This geometry and backlighting method is still being used with great success to compare experimental absorption spectra with opacity codes, for example in experiments performed using the HELEN laser with Nd as the target of choice [68]. Further comparisons with opacity codes [69] are made for lower-Z elements, for example against Al [70] at solid density and $20 - 60\,\mathrm{eV}$, however this time using a deposited high-Z layer on the target as the backlighter, known as an "integrated backlighter". Great strides have been made in the field in terms of target construction, laser control, and backlighter, as well as shot-to-shot repeatability culminating in the measurement of a higher-than-predicted iron opacity in 2015 by Bailey et al. [59], and the corresponding attempts to reconcile this measurement's discrepancies with opacity models [24, 25, 26, 71].

Another important aspect of these experiments is the diagnosis of their temperature and density at the time of measurement of the opacity. This is typically achieved through the addition of further dopants with a lower-Z, for example magnesium in the iron opacity measurement [59], and then by using their K-shell absorption spectra as a diagnostic. These dopants are chosen to be low-Z as generally the models used to simulate K-shell spectra are much simpler, as there are fewer electrons and consequently transitions, and more complete atomic models including effects such as autoionization or doubly-excited states may be incorporated more completely [72], or

at least with a greater consensus on implementation [73]. Furthermore, the lines shift in energy with ionization allowing facile identification of lines from different ionization stages at first glance – an effect that was exploited in the work on FELs described in Ch. 1. The appearance of individual lines is incredibly sensitive to the electron temperature which determines the degree of ionization, and their Stark-broadened width is a standard diagnostic for the electron density [39, 74]. In general, the broadening increases with principal quantum number and the opacity decreases making these lines optically thin. The corollary of this is that these lines are weaker and may be measured less accurately. There needs to be a trade-off, and as many lines as are available accounting for continuum lowering are measured. For the "enigmatic" work on iron it was especially important to ensure that uncertainties in the conditions from the choice of model for Mg were not responsible for their discrepancy between measured and calculated opacities [75].

Finally, perhaps the most difficult prerequisite to make accurate laboratory measurements is to heat a material to a sufficiently high temperature and density that it exists in Local Thermal Equilibrium (LTE). Only then can a true comparison be made with the Sun where LTE is enforced by its strong radiation field [59].

2.2 The advantages of using an X-ray FEL

The fundamental requirements for a standard experiment to measure the opacity can be summarised as the following [62, 76]. Firstly, the sample must undergo minimal hydrodynamic expansion, essentially remaining confined on the timescales that the measurement is made. Secondly, it must be have uniform conditions during the measurement, with minimal thermal and density gradients. Thirdly, the plasma must be independently characterised with information on the temperature, density, uniformity, and deviation from LTE. Finally, the absorption spectrum must be measured

accurately with a spectrally uniform backlighter.

The proposition of this thesis is that all of these requirements may be overcome through heating with an X-ray FEL. The method will be the following: to heat solid density foils rapidly and isochorically before any hydrodynamic expansion can occur. The sample will have uniform conditions along the longitudinal heating axis, though not in the transverse direction. This non-uniformity will be characterised by measuring the focal spot profile with ablative imprints [77]. Moreover, its temperature and density will be calculated by modelling the simple X-ray absorption with the atomic-kinetics code SCFLY. The only required diagnostic is the sample's emission spectrum which is gated in time by the X-ray FEL: emission lines are only recorded when a K-shell hole is created by an X-ray photon from the FEL, thus ensuring diagnosis of the sample plasma in its inertially confined heating phase. Modulating the thickness of the created plasmas by using a selection of targets with different thicknesses allows a fit of the emission spectra to be made to the 1D slab solution of the equation of radiative transfer and the emissivity and opacity to then be deduced without recourse to a backlighter or measurement of the absorption spectrum. However, care must be taken to ensure that even for the thickest targets the heating remains uniform longitudinally, and that any gradients along the X-ray beam direction due to attenuation are comprehensively evaluated.

It is in this context that the advantages of using an FEL begin to become clear. The first limitation of the aforementioned opacity methods is the need to constrain the hydrodynamic expansion of the target during the heating and measurement stage. Moreover, it is not even sufficient to mediate this effect but also to then quantitatively measure it. Again, in the campaign to measure opacity of iron, point-projection radiography was employed irradiating the sample along its edge to measure sample expansion and thus deduce its density [62]. The use of an FEL eliminates this requirement: the femtosecond heating achieved allows the target to be heated isochor-

ically [27] and diagnosed before any hydrodynamic expansion has occurred. Another benefit of this approach is that the electron density may be attained accurately without recourse to Stark-broadened lines given solely by the degree of ionization of the plasma determined by the electron temperature. The M-shell (states with a principal quantum number of $n = 3$) for these plasmas has been shown to be unbound for all ionization stages in Al [47], and so only the α-lines comprising transitions from $n = 1$ to $n = 2$ exist making Stark-broadening an unattractive diagnostic for FEL-created plasmas.

A potential caveat of heating with an FEL is the large transverse gradients within the focal spot owing to the heating with an intensely focussed beam of X-rays. The longitudinal gradient due to the focussing is small – the FEL has a measured Rayleigh range of order 10 mm [78] – and any gradients in the longitudinal direction will depend on the attenuation length of the target to X-rays [55]. Simultaneous measurements of the beam's transverse profile will be made through ablative imprints in Lead Iodide (PbI_2) and a super-gaussian beam profile is used for modelling [77]. The simulation work in this thesis closely follows that in Ciricosta et al. [47] by dividing the target into 26 zero-dimensional intensity simulations with an intensity profile:

$$I_n(\omega, t) = I_0(\omega, t)\, \exp\big(-2n^2/100\big), \tag{2.4}$$

where I_0 is the focal intensity profile which is Gaussian in FEL frequency ω and time t, and $n = 0, ..., 25$. Using an appropriate weighting with the beam profile across the target, these 26 zero-dimensional simulations may be combined to give modelled spectra that are an excellent match to the data [47]. The simulation work is covered in detail in Ch. 3, and provides a self-consistent calculation of the temperature and density at any point in the plasma's evolution and spatially across the focal spot following the recipe of Ch. 1.3.

Another possible issue is the loss of fast electrons (either those directly photoionized from the L-shell or Auger electrons) from a locally small zero-dimensional SCFLY simulation. These could travel transversely through the target at speeds in excess of $20\,\mathrm{nm\,fs^{-1}}$. The effect of these electrons on the veracity of the calculated plasma conditions, such as electron temperature and density, therefore merits some consideration. In fact, it is found that this should not have an effect and instantaneous thermalisation transpires to be a reasonable assumption. It has been investigated previously in the following way [47]. The population array $N_i(t)$ (defined in Eqn. 1.18) was extended, adding a bin for each Auger transition $N_k(t)$, thus separating the fast Auger electrons with energy $E_k \sim 1\,\mathrm{keV}$ from the thermal electrons. This bin was then allowed to depopulate by collisional processes with both ions and electrons separately, transferring each fast electron to the thermal electron distribution. Incorporating this extra step was found to have no effect on the predicted temperature and density evolution and, whilst the primary recombination mechanism of a K-shell hole is the Auger recombination channel, it was found that at no point did the population of the sum of these Auger bins, $N_k(t)$, exceed 0.2% of the total number of free electrons [47]. Assuming that the population of electrons directly photoionized from the L-shell are similar or lower[1] then even if one were to assume no thermalisation, and that these electrons were lost completely to neighbouring simulations, then it would not drastically affect the calculated plasma conditions. It is worth noting that the electrons photoionized from the K-shell have kinetic energies $< 240\,\mathrm{eV}$ and so travel a much shorter distance before thermalising with the free electrons through collisions. Therefore, given that each Auger electron is necessarily created following a K-shell photoionization, then the number of these electrons will also be small.

Opacity related effects have already been inferred using an FEL following the pre-

[1]In fact one could argue significantly lower because of the much lower absorption cross-section versus K-shell photoionization, and the fact that each photoionized K-shell electron yields 0.97 Auger electrons.

scription described earlier – by measuring the transmission through a target. In Rackstraw et al. [79], saturable absorption in a 1 μm thick solid Al foil was observed from the transmission through the target recorded on a photodiode. Traditionally, saturable absorption is observed by photoionizing a sample rapidly and at a much faster rate than it can relax through recombination processes. Prior to this work, saturable absorption in this fashion was observed in the XUV (around the L-edge of Al) at FLASH [1, 80] and as such was only observed with X-rays for atoms [81], molecules [82], and nanoscale clusters of atoms [83]. The technique of Rackstraw et al. [79] differs from that above by exploiting the tunability of the FEL, much like in the IPD work [30] discussed in the previous chapter. When the FEL is tuned between the edges of two ionization stages of Al, it will heat the sample through photoionization up until the point at which the K-edge of the next ionization stage now lies at an energy exceeding the X-ray photon energy. Subsequently the material becomes transparent to these X-rays and the absorption saturates; it may now only absorb photons through L-shell photoionization with a much lower cross-section [79].

The effect of this heating is such that there is not the expected marked drop in transmission above the cold K-edge of Al that would be expected if the sample were to remain cold, followed by a gradual increase in transmission as the cross-section changes (see Eqn. 4.1). Instead, as the FEL is tuned above the K-edge, the transmission slowly drops as a direct result of the transparency occurring later and later in the pulse as it takes longer to burn through charge states up to the point where one is probing below the next K-edge. Eventually, as the photon energy is tuned to exceed all the edges, the experimental transmission approaches that expected by the cold case.

This method has its own limitations though. The measurement with a photodiode is inherently a time and space integrated measurement, and the specific mechanisms through which opacity effects arise are deduced from time and space resolved sim-

ulations matching the experimentally observed diode transmission once integrated. Instead, in this thesis, a different method will be expounded relying on emission spectroscopy which, due to the absorption mechanism changing over time, intrinsically provides time and space resolved information in the appearance of each K-α emission line. This will allow more confidence in the correct extrication of competing temporal and geometric (across the focal spot) effects.

This is perhaps the most important difference between the method advanced through this thesis and traditional methods of measuring opacity. In previous work, the use of a broadband backlighter gives information on the steady-state opacities across a wide frequency range containing many lines, gated by the backlighting time [57, 62, 66, 68]. Therefore, the opacity is found for the entire lineshape, over a system of lines [59, 60, 70], and the plasma heating is engineered such that the conditions remain uniform and constant over the measurement time [21, 58]. It is in this context that the method applied to HDM in this thesis is very different. Here, the opacity will be found for the optically-thick regions (near a line centre) only, and for each K-α line of magnesium in very different conditions. The highly-transient nature of heating with an X-ray FEL and the exotic, non-thermal nature of the emission provides a gated probe, both temporally and spatially. Each part of the spectrum will be probed in conditions, close to LTE, and that maximise both the line opacity and line emission as the upper and lower states appear contemporaneously. Through the use of SCFLY simulations the temperature and electron density of the measurement will be constrained by the size of the emitting region (temporally and spatially) for each line.

The extraction of the emissivity and opacity in each spectral window where each emission line emits will be achieved by fitting to the 1D slab solution of the equation of radiative transfer for plasmas of different thicknesses under well characterised conditions given by the SCFLY simulations. However, this 1D slab solution assumes no

longitudinal gradients along the heating axis. In reality, heating above the K-edge, in order to view all K-α emission lines, leads to significant absorption of X-rays such that attenuation of X-rays can become problematic for thicker targets. This is taken into account by the move to a three-dimensional model of the plasma in Ch. 5 that will allow the attenuation of the X-ray FEL to be handled consistently and its effect on the fit to the opacity to be quantified.

2.3 Radiation Transport

The opacity measurements that follow in the rest of this thesis will rely on solving (or in this case, bypassing) a fundamentally difficult problem: the coupling of radiation to atoms as it transits through a plasma – radiation transport. Generally, in a dense emitting plasma radiation will be re-absorbed and re-emitted as it transits from region to region. Often, this will have a strong effect on the populations involved at the frequency of the radiation.

Consider first a general rate equation for some upper state n_u. It will involve non-radiative terms C, spontaneous emission A_{ul}, and a stimulated emission B_{ul} and absorption B_{lu} term driven by the radiation field $I(\nu)$ between it and the lower state n_l. The rate equation is:

$$\frac{dn_u}{dt} = C - n_u A_{ul} - n_u B_{ul} I(\nu) + n_l B_{lu} I(\nu). \tag{2.5}$$

Computationally, this problem is not trivial and often requires fine spatial gridding and a simultaneous calculation of the atomic-kinetics and radiation transport causing computing costs to grow. Instead, most atomic-kinetics codes use an escape factor formalism, where the effect of the internal radiation field driving a transition is ac-

counted for by a reduction in the A-rate by a factor of P_e, defined as:

$$P_e n_u A_{ul} = n_u A_{ul} + n_u B_{ul} I(\nu) - n_l B_{lu} I(\nu), \tag{2.6}$$

making the rate equation then,

$$\frac{dn_u}{dt} = C - P_e n_u A_{ul}. \tag{2.7}$$

The escape factor incorporates the size and shape of the emitting plasma allowing radiation trapping to be correctly handled [52]. The length that should be provided to do this in a zero-dimensional code[2] is the mean chord[3] which depends on the geometry of the plasma, and is different to the line-of-sight through the plasma. For example, in a planar plasma the mean chord is twice the line-of-sight thickness corresponding to a ray passing at an angle of 60° to the surface normal [52]. There have been many different forms suggested for the escape factor [84, 85, 86, 87], and a comparison of them is made in Phillips et al. [52]. In general, the form of the escape factor should be a function of the lineshape, which is often Voigt involving a convolution of Lorentzian and Gaussian processes. Nevertheless, the form used in SCFLY, accounting for a range of emission depths, is formulated as:

$$P_e(\tau_0) = \begin{cases} 1 - \tau_0/2 & \tau_0 < 0.01, \\ c(\arctan[d\tau_0 + e] - f)/\tau_0 & 0.01 \leq \tau_0 < 5.18, \\ (a + b\sqrt{\ln \tau_0})/\tau_0 & \tau_0 \geq 5.18. \end{cases} \tag{2.8}$$

as a function of the line centre optical depth τ_0, and the constants $a - f$ are as given in Phillips et al. [52]. Note that some errors in this paper have been corrected here. For more details on the derivation of escape factors see Phillips et al. [52].

[2]An atomic-kinetics code that has no information on the geometry of the problem.
[3]Found by averaging over all lines of sight.

Furthermore, the use of an escape factor works most effectively when the plasma has minimal temperature and density gradients and the geometry is known. When this is not the case, discourse must be made to a self-consistent treatment of the populations and radiation field such as in the CRETIN code [72]. Nevertheless, good agreement is found between the escape factors of Eqn. 2.8 and CRETIN. As will be made clear later, for FEL driven plasmas the escape factor effect on the populations is small and they are affected predominantly by the driving X-rays [55], thus the problem of solving the radiation transport is extricated from the atomic-kinetics and its calculation then becomes one of accounting the emission through the plasma.

Now that the populations have been accurately found, it remains to propagate the plasma emission out along the line-of-sight. The derivation below follows that of Mihalas [64].

Consider the specific intensity $I(\nu, t, \mathbf{r}, \mathbf{n})$ of radiation at position $\mathbf{r}$, which travels in the direction $\mathbf{n}$, at a frequency ν, and at a time t. This may be defined as the amount of energy dE which is transported through a surface dS into a solid angle $d\omega$:

$$dE = I(\nu, t, \mathbf{r}, \mathbf{n})\ \mathbf{n} \cdot \mathbf{dS}\ d\omega\ d\nu\ dt, \tag{2.9}$$

where $\mathbf{n} \cdot \mathbf{dS} = dS\cos(\theta)$, and θ is the angle between the surface normal and direction of propagation of the radiation. Without loss of generality, the surface normal may be chosen to be parallel to the ray.

As the radiation passes through a volume of material with area dS and length $d\lambda$ its intensity will increase due to emission in the volume with emissivity $\eta(\nu, t, \mathbf{r}, \mathbf{n})$, and decrease due to absorption with opacity $\kappa(\nu, t, \mathbf{r}, \mathbf{n})$. The energy that emerges at

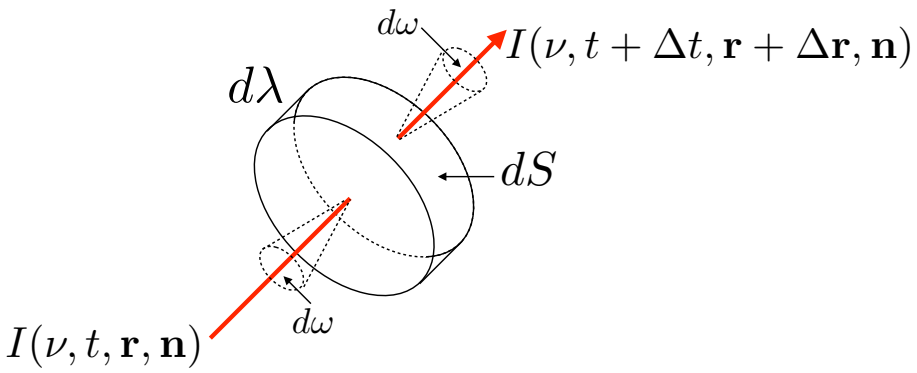

Figure 2.2: An element of emitting and absorbing material with surface dS and path length $d\lambda$ through which a beam of radiation passes with solid angle $d\omega$. The radiation's intensity is initially $I(\nu, t, \mathbf{r}, \mathbf{n})$ and then Δt later when it exits at $\mathbf{r} + \Delta\mathbf{r}$ is $I(\nu, t + \Delta t, \mathbf{r} + \Delta\mathbf{r}, \mathbf{n})$.

the front surface at position $\mathbf{r} + \Delta\mathbf{r}$ along the ray at a later time of $t + \Delta t$ will be:

$$\begin{aligned}[I(\nu, t + \Delta t, \mathbf{r} + \Delta\mathbf{r}, \mathbf{n}) - I(\nu, t, \mathbf{r}, \mathbf{n})]\ dS\ d\omega\ d\nu\ dt \\ = \ [\eta(\nu, t, \mathbf{r}, \mathbf{n}) - \kappa(\nu, t, \mathbf{r}, \mathbf{n}) I(\nu, t, \mathbf{r}, \mathbf{n})]\ d\lambda\ dS\ d\omega\ d\nu\ dt,\end{aligned} \tag{2.10}$$

and is shown diagrammatically in Fig. 2.2.

The change in intensity can be separated into partial derivatives in time and space along the path taken by the ray. If the ray is oriented parallel to the surface normal then the path length along the ray is $\Delta t = \Delta\lambda/c$ and the emergent intensity is,

$$I(\nu, t + \Delta t, \mathbf{r} + \Delta\mathbf{r}, \mathbf{n}) = I(\nu, t, \mathbf{r}, \mathbf{n}) + \left[c^{-1}\frac{\partial I}{\partial t} + \frac{\partial I}{\partial \lambda}\right] d\lambda. \tag{2.11}$$

The ray travels in some direction $\mathbf{n}$ relative to an orthogonal coordinate system and so $\partial/\partial\lambda = \mathbf{n} \cdot \nabla$.

Dropping all extraneous derivatives, Eqn. 2.10 becomes:

$$\left[c^{-1}\frac{\partial}{\partial t} + \mathbf{n} \cdot \nabla\right] I(\nu, t, \mathbf{r}, \mathbf{n}) = \eta(\nu, t, \mathbf{r}, \mathbf{n}) - \kappa(\nu, t, \mathbf{r}, \mathbf{n}) I(\nu, t, \mathbf{r}, \mathbf{n}). \tag{2.12}$$

This is the completely general radiative transfer equation.

Next it is useful to make some generalisations relevant for a one-dimensional planar slab of plasma with uniform conditions. It is assumed that the slab is semi-infinite in the $x-y$ plane, and is bounded in the z-direction. The radiation emerges at an angle θ to the z-direction, therefore $\mathbf{n}\cdot\nabla = \cos(\theta)\partial/\partial z$. Eqn. 2.12 becomes:

$$\Big[c^{-1}\frac{\partial}{\partial t} + \cos(\theta)\frac{\partial}{\partial z}\Big] I(\nu,t,z,\theta) = \eta(\nu,t) - \kappa(\nu,t)I(\nu,t,z,\theta), \tag{2.13}$$

and in the time-independent case, dropping the explicit (ν,t,z,θ) dependence, is then:

$$\cos(\theta)\frac{\partial I}{\partial z} = \eta - \kappa I. \tag{2.14}$$

This first order differential equation is solved simply using an integrating factor of $\exp(\kappa z/\cos(\theta))$. Multiplying through Eqn. 2.14 with this gives:

$$\Big[\cos(\theta)\frac{\partial I}{\partial z} + \kappa I\Big]\exp(\kappa z/\cos(\theta)) = \frac{\partial}{\partial z}\Big[\cos(\theta)\exp(\kappa z/\cos(\theta))I\Big] = \eta\exp(\kappa z/\cos(\theta)), \tag{2.15}$$

with solution assuming the slab is bounded by planes at $z=0$ and $z=d$,

$$\int_{z=0}^{d}\partial\Big[I\cos(\theta)\exp(\kappa z/\cos(\theta))\Big] = \int_0^d \eta\exp(\kappa z/\cos(\theta))dz, \tag{2.16}$$

and performing the integration:

$$I(d)\cos(\theta)\exp(\kappa d/\cos(\theta)) - I(0)\cos(\theta) = \frac{\eta}{\kappa}\cos(\theta)\Big[\exp(\kappa d/\cos(\theta)) - 1\Big]. \tag{2.17}$$

Rearranging for $I(d)$ gives:

$$I(d) = I(0)\exp(-\kappa d/\cos(\theta)) + \frac{\eta}{\kappa}\Big[1-\exp(-\kappa d/\cos(\theta))\Big]. \tag{2.18}$$

Finally, reinserting the dependencies on (ν, t, θ) and assuming that the slab is not illuminated at $z = 0$ so that $I(0) = 0$, yields the final solution in terms of the source function $S = \eta/\kappa$:

$$I(\nu, t, d, \theta) = S(\nu, t)[1 - \exp(-\kappa(\nu, t)d/\cos(\theta))]. \tag{2.19}$$

The 1D slab solution of Eqn. 2.19 will be used at length in the following chapters and a fundamental assumption will be that the emerging radiation from the targets obeys the form of this equation.

Chapter 3

Creation of Optically-Thin Solid-Density Plasmas using LCLS

In this Chapter the results from the LCLS experiment on ultra-thin foils are described. Spectrally-resolved measurements of the X-ray emission from thin foils of solid magnesium heated with an X-ray FEL (XFEL) within 200 fs to peak electron temperatures of order 180 eV are presented. From the thickness-dependent emission, frequency-resolved time-averaged opacities are extracted that are a good measure of the peak opacity present within the system. Simulations of time-integrated spectra using SCFLY allows an estimate the temperature and density conditions at which the opacity is measured. The frequency-dependence of the time-integrated source function can also be reconstructed, and the results for both opacity and source function are in good agreement with atomic-kinetics calculations.

3.1 Experimental Setup

The experiment was performed at the SXR endstation [17] of LCLS. Targets comprising thin ($d = 24\,\text{nm} - 487\,\text{nm} \pm 2\,\text{nm}$) foils of Mg mounted onto Si wafers and coated

with 60 ± 20 nm of CH to protect against oxidation were irradiated by 100 fs pulses[1] of X-rays, focussed using Kirkpatrick-Baez Optics (KBO). The nominal pulse energy was measured by a gas monitor detector (GMD) to be 1.4 - 2.2 mJ prior to transmission through the beamline focussing optics. The FEL photon energy was varied between 1315 and 1700 eV from just above the cold K-edge (1305 eV) to energies in excess of the threshold for observation of Ly-α (hydrogenic K-α) line emission.

The results described here are for the specific case of the FEL pump photon energy at 1540 eV, with a pulse energy of 1.8 mJ, which is then reduced to around 30% of its upstream nominal value by the beamline focussing optics [88]. This is sufficient for observation of K-α lines from the cold through to the He-α (helium-like K-α) line.

The main diagnostic was K-α spectroscopy recorded by means of a flat crystal Bragg spectrometer employing a Beryl $(10\bar{1}0)$ crystal ($2d = 15.96$ Å). Each shot was taken on a fresh portion of target which was oriented at an angle of $\theta_F = 45°$ to the incident X-ray beam, and with the spectrometer observing at an angle of $\theta_S = 20° \pm 2°$ to the target normal, recording X-rays on a Princeton Instruments CCD camera. For a diagram of the experimental setup see Fig. 3.1.

The spatial distribution of X-ray intensities on target was determined *ex situ* via imprint measurements in Lead Iodide (PbI_2), as described in Chalupský et al. [77], and the focal spot on target had an effective area of 8.5 μm^2, corresponding to a peak irradiance around 10^{17} Wcm^{-2}.

3.2 Data Analysis

The SXR endstation is equipped with Data Acquisition Software (DAQ) which allows the collection, on a shot-to-shot basis, of the FEL pulse energy (from a GMD upstream) and the FEL photon energy, as well as spectra from the CCD camera.

The nominal FEL photon energy was varied between 1315 eV and 1700 eV, whilst

[1] Assumed to be equal to the duration of the electron bunch [47].

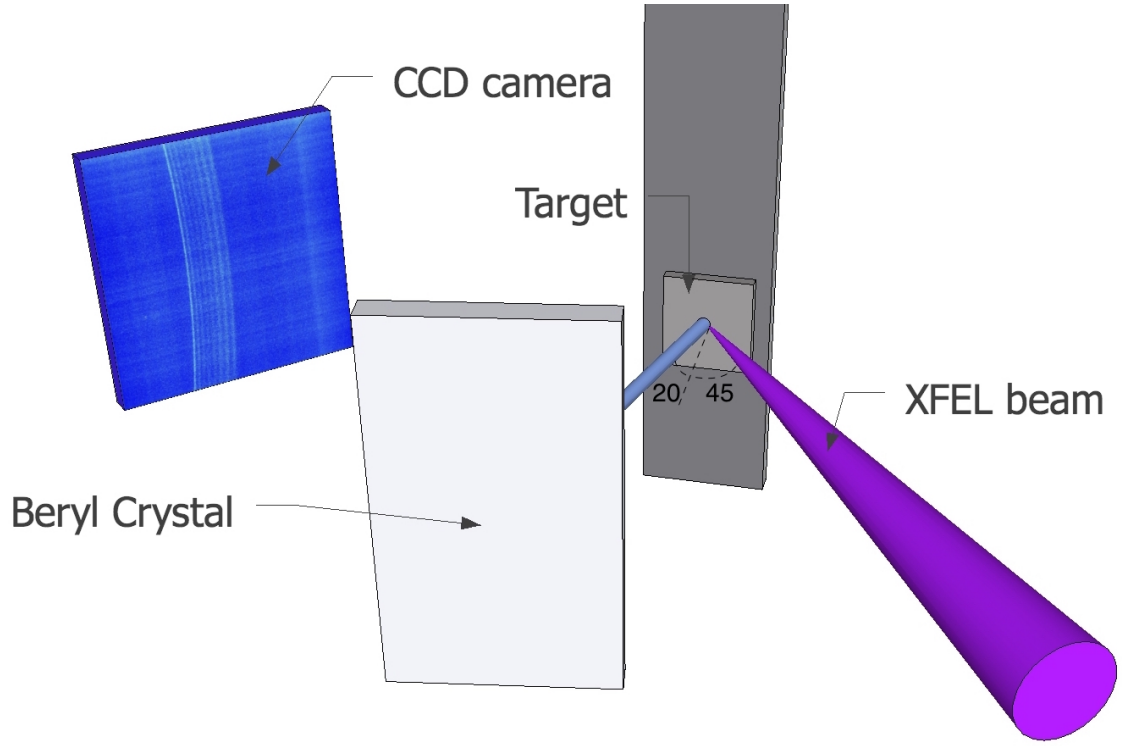

Figure 3.1: Experimental setup showing target, Beryl crystal, CCD camera with a typical CCD image, and the direction of the FEL beam. As labelled in the figure, the target was irradiated at an angle of 45°, and the spectrometer observed emission at an angle of 20° to the target normal.

the pulse energy was kept constant. For the results discussed here the FEL photon energy was fixed around 1540 eV and a narrow spread was observed in both the photon energies and pulse energies actually delivered to the target.

At each FEL photon energy at least 10 shots were taken on each target, and more on the thinner targets (up to 123 shots) which emit fewer photons. Firstly, shots were selected as having a pulse energy within 20% of the mean pulse energy for that batch. Individual images were checked for a good level of signal and for dead pixels; where these occur, these were normally corrected to the background level, or if irreparable, this shot was discarded. The number of shots discarded through this method was small ($< 5\%$ of shots).

Next, the background image is subtracted from each image and the image is then straightened to counteract the curvature of the cone of emission from the target

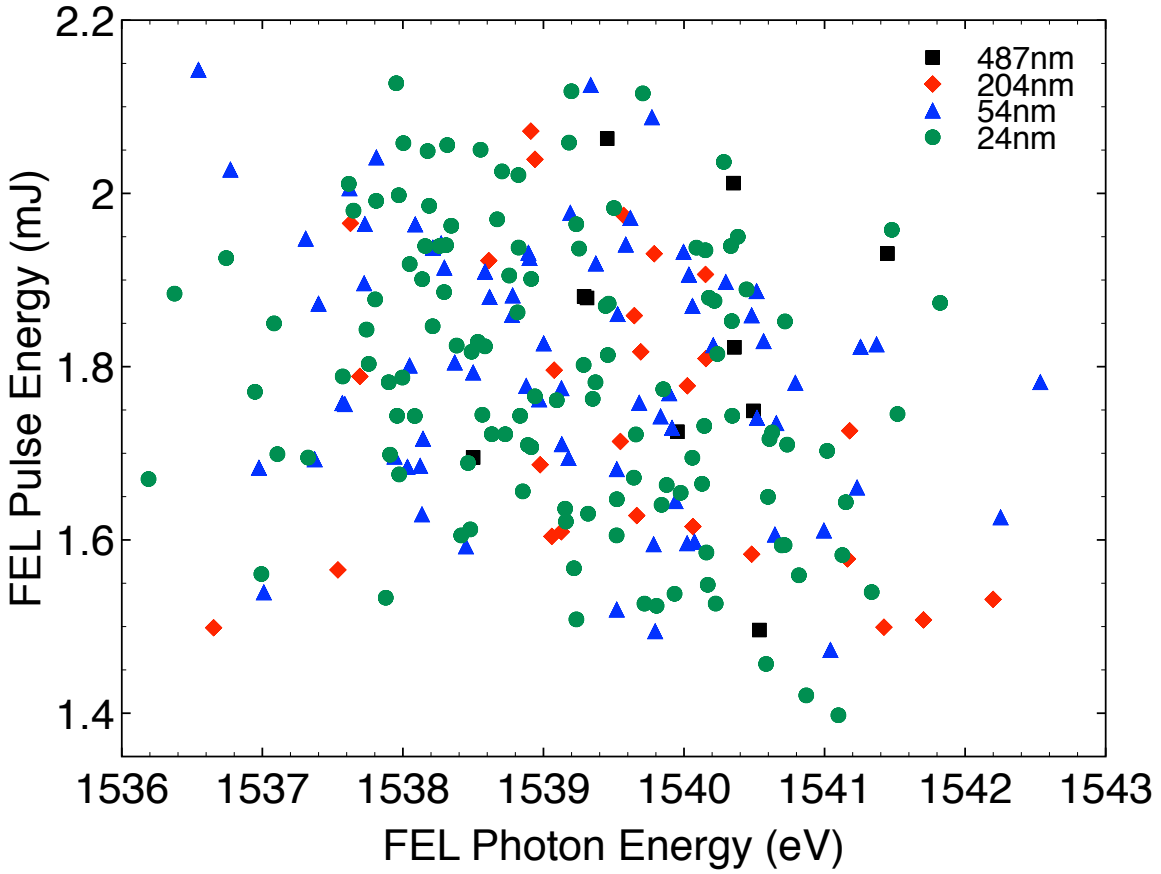

Figure 3.2: Shot-to-shot scatter of FEL photon energy versus FEL pulse energy of shots used in recorded emission spectra showing a narrow spread. The mean FEL photon energy was 1539 ± 1 eV, and the mean FEL pulse energy was 1.8 ± 0.2 mJ.

intersecting the planar CCD. This is achieved by fitting a circle through the curved emission lines and optimising its radius and centre to maximise the intensity of the cold K-α line which is the brightest spectral feature. The images were summed along the non-dispersive axis (the vertical axis on the CCD image shown in Fig. 3.1) yielding an emission spectrum for each shot which is remarkably flat outside the region of K-α line emission (zero level for each single shot). Individual spectra were then adjusted to the same zero-signal level, and summed correcting for spatial beam jitter (which shifts the spectra over a few pixels) by forcing the narrow, bright cold K-α line to overlap between shots. These multi-shot spectra were normalised according to the number of shots, thus giving the mean emission intensity of the target per shot, while

the shot-to-shot deviation from the mean gives the standard deviation.

The distribution of FEL photon energy and FEL pulse energy for each target was also recorded. Shown in Fig. 3.2 is this shot-to-shot scatter in FEL photon and pulse energy: each thickness has near identical (much less than one standard deviation) mean FEL photon energy and mean FEL pulse energy. For all shots taken on all targets the mean FEL photon energy was 1539 ± 1 eV, and the mean FEL pulse energy was 1.8 ± 0.2 mJ.

The spectra were calibrated in emitted photon energy using a fit of the Bragg angle to the positions of four widely spaced lines (lines III, VII, X, and XI) covering the range of interest. The spectra are then rebinned into 0.5 eV steps of emitted photon energy, similar to the recorded resolution of ~ 0.3 eV per pixel. The resolving power ($\lambda/\Delta\lambda$) of the spectrometer, dominated by the rocking curve of the crystal, was of order 4000. This value is consistent with the experimentally observed width of the K-α emission from the cold solid, when taking into account the natural linewidth [89]. The cold K-α for the thinnest target has a linewidth of 1.42 eV, and the total experimental broadening (Gaussian) is therefore 1.3 eV.

3.3 Experimental Results

The experimental emission spectra from the four targets are shown in Fig 3.3. The coloured bar around the lines indicates the shot-to-shot standard deviation of recorded intensity on the CCD. The number of combined shots was 10 on the 487 nm target, 27 on the 204 nm target, 75 on the 54 nm target, and 123 on the 24 nm target. The lines are numbered from III for the cold K-α line to X for the He-α line, where the roman numeral designating an emission line refers to the ionization stage of the emitting ion [28]. The ground state of magnesium is a 2^+ ion having two delocalized electrons in the conduction band, and so the cold K-α line originates from a 3^+ ion generated

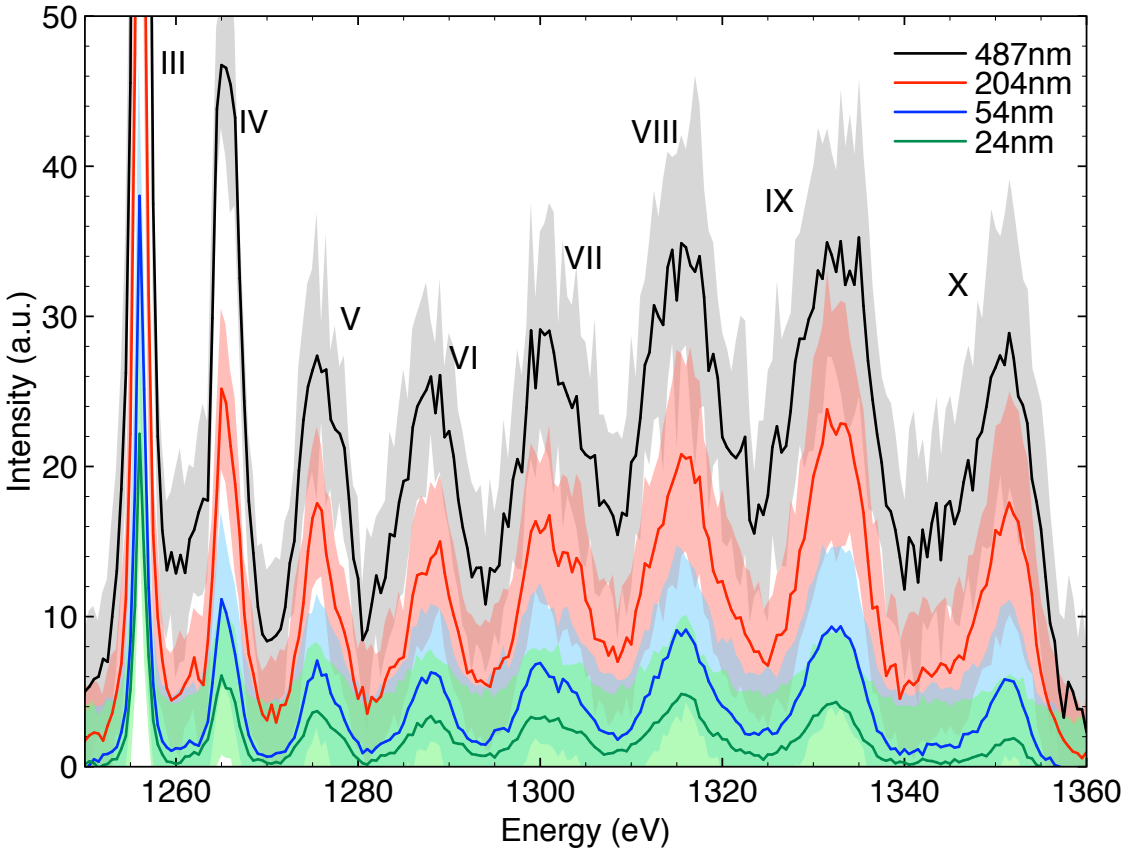

Figure 3.3: Experimental X-ray emission spectra for Mg targets of four different thicknesses, heated by the LCLS X-ray pulse with an FEL photon energy of 1540 eV and FEL pulse energy of 1.8 mJ. Each spectrum is the sum of spectra from multiple shots, and is normalised by the number of shots. The lines are labelled according to the charge state of the emitting ion. Coloured bars indicate the standard deviation from combining multi-shot spectra.

by photoionization of a K-shell electron by the FEL. The diagnostic here is the K-L radiative recombination of an L-shell electron filling the K-shell hole created by the FEL, and all lines from the cold K-α to the He-α are observed. As an example, shown in Fig. 3.4 is the photoionization process (PI) and then radiative recombination (KL) that produces line VII. Here the super-configurations change as:

$$K^2L^4 + h\nu_{FEL} \xrightarrow{PI} K^1L^4 + e^- \xrightarrow{KL} K^2L^3 + e^- + h\nu, \tag{3.1}$$

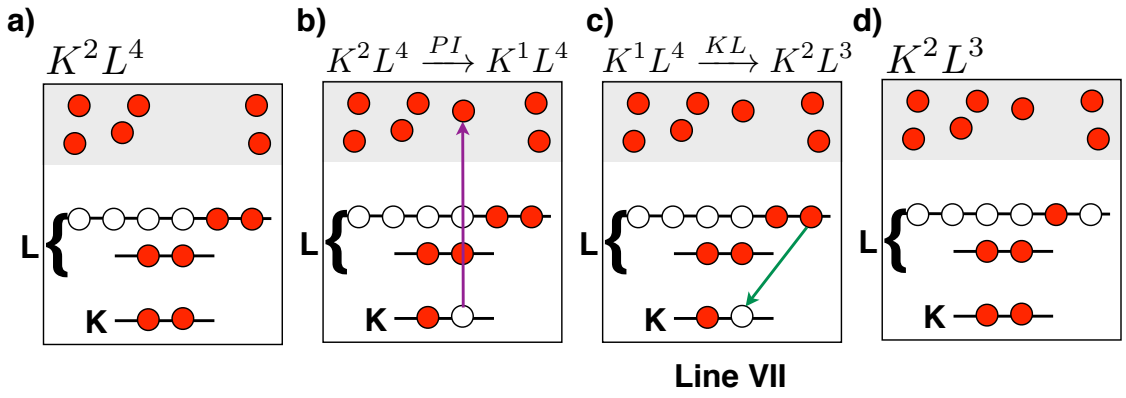

Figure 3.4: The photoionization and radiative recombination chain of Eqn. 3.1 including initial and final ground-state super-configurations. a) Ground state of carbon-like Mg. b) Photoionization process for carbon-like Mg absorbing an FEL photon and exciting a K-shell electron to the continuum. b) The following K-L radiative recombination filling this K-shell vacancy in boron-like Mg giving line VII. d) Ground state of boron-like Mg.

where the superscript integer represents the number of electrons in the K-shell or L-shell, and the final state has one fewer electron and emits a K-α photon. The fluorescence yield for Mg is low (3%) [90], so the dominant decay mechanism for states with more than two electrons in the L-shell is Auger recombination (A) which is radiationless and follows the process:

$$K^2L^4 + h\nu_{FEL} \xrightarrow{PI} K^1L^4 + e^- \xrightarrow{A} K^2L^2 + 2e^-, \tag{3.2}$$

liberating two electrons for every photoionization of the K-shell which rapidly thermalise [53].

The use of an X-ray FEL affords a unique opportunity to pump and probe the system. The electronic dynamics of the L-shell is dominated by collisions, owing to the high density of the plasma, and thus is in Local Thermodynamic Equilibrium (LTE).

In LTE the McWhirter criterion relating the collisional de-excitation rate to the radiative recombination rates is satisfied [91]. This condition is reached when the

collision-induced transitions upwards, with rate C_{lm}, far outweigh the radiative transitions down to the lower state, with rate A_{ml}:

$$\begin{aligned} N_l \sum_{m>l} C_{lm} &\gg \sum_{m>l} N_m \, A_{ml}, \\ N_m \sum_{m>l} C_{ml} &\gg \sum_{m>l} N_m \, A_{ml}, \end{aligned} \tag{3.3}$$

for all states $m > l$. Here, N_m are the populations in the upper states and N_l the population in the lower state, and in the second line the principle of detailed balance has been to used to relate the collisional rate up to the rate down: $N_l \, C_{lm} = N_m \, C_{ml}$.

To leading order, the most important term in the summation is the next higher level $u = l + 1$, i.e.

$$N_u C_{ul} \gg N_u A_{ul}. \tag{3.4}$$

In the situation relevant to this work, the lower state is the case with a full K-shell and some number of X electrons in the L-shell: K^2L^X. However, since the M-shell is unbound (forms part of the continuum) [47], and therefore there are no higher levels available for bound-bound transitions, the upper state with population N_u is the super-configuration with another vacancy in the L-shell, K^2L^{X-1}, and an L-electron collisionally ionized to the continuum. This greatly simplifies the mathematics. The rates required are the following: C_{ul} the collisional recombination rate (or its inverse C_{lu} the collisional ionization rate) and A_{ul} the spontaneous radiative recombination rate.

The McWhirter condition is commonly considered to be satisfied [91] when the collisional recombination rate (downward transitions per unit time due to collisions) is greater than 10 times the radiative rate:

$$C_{ul} > 10 A_{ul}. \tag{3.5}$$

For the ionization of an L-shell electron from carbon-like Mg (the same as that shown in Fig. 3.4a), the collisional recombination (CR) and radiative recombination (AR) processes are:

$$\begin{aligned} K^2L^3 + e^- &\xrightarrow{CR} K^2L^4, \\ K^2L^3 + e^- &\xrightarrow{AR} K^2L^4 + h\nu. \end{aligned} \tag{3.6}$$

SCFLY calculates the rates of these processes as $C_{ul} = 1.63 \times 10^{14}$ s^{-1} and $A_{ul} = 2.06 \times 10^{11}$ s^{-1} when the population of K^2L^3 is a maximum. Here, the plasma is at a temperature $T = 65\,\text{eV}$ and density $n_e = 290 \times 10^{21}\,\text{cm}^{-3}$. Indeed for all charge states, $C_{ul} \sim 0.9$–1.8×10^{14} s^{-1} and $A_{ul} \sim 0.1$–3.2×10^{11} s^{-1}. Clearly, the McWhirter condition is satisfied for this plasma.

There are, however, some caveats to this that are worth mentioning. Firstly, there is some appreciable ionization of the L-shell by the FEL photons, albeit with a much smaller cross-section than for the K-shell. For the ion stages considered above, this is larger than the ionization rate due to collisions with both thermal electrons and Auger electrons only at low temperatures, and at early times [92]. However, the ionization rate of L-shell electrons due to collisions with thermal electrons exceeds the photoionization rate at later times (higher temperatures) when the ground state populations peak (as discussed later). Therefore, the analysis above is robust to this. A further issue arises for the lower charge states which peak at early times. For all temperatures, SCFLY uses the Maxwell-Boltzmann distribution for the thermal electrons but at low temperatures ($T < 20\,\text{eV}$) the distribution should instead be Fermi-Dirac. Because the free-electron density is high, this has repercussions for the calculated rates for all processes involving thermal electrons due to the degeneracy of the free-electron quantum states [93]. For example, sizeable K-β emission has been identified experimentally [30] indicating that the recombination rate for the K^2L^7 super-configuration is larger than the A_{ul} quoted above. Essentially, the McWhirter

condition is satisfied provided one's plasma is not too cold as found early in the FEL pulse, and it should not be expected to be well satisfied for the cold K-α line. Moreover, in general the cold K-α line is not well estimated by SCFLY and depends strongly on the number of photons in the wings of the focal spot.

However, at any instant during the pulse a few percent of ions have a core hole induced by photoionization and in this sense are out of LTE. Since our temperatures are too low to thermally excite these K-shell holes, and their lifetime is short (filled by Auger recombination in Eqn. 3.2), the use of an FEL gives an instant snapshot of an LTE distribution. Furthermore, the collisional excitation rate for a K-electron to the L-shell is also low ($\sim 10^3$ s^{-1}), meaning that the K-shell is isolated from the Thermodynamic Equilibrium set up between the L-shell and the continuum.

As the absorption length of the system to the heating X-ray beam is long (of order microns [55]) the system is free of longitudinal gradients and the ionic populations are independent of target thickness d along the X-ray beam direction. Therefore, if the transverse scale-lengths are smaller than the target thickness, the instantaneous frequency-dependent intensity $I(\nu, t, d, \theta)$ emitted at an angle θ to the normal of a target of nominal thickness d at time t, owing to the filling of these core holes, obeys the simple 1D uniform slab solution to the equation of radiative transfer,

$$I(\nu, t, d, \theta) = S(\nu, t)[1 - \exp(-\kappa(\nu, t)\, d/\cos(\theta))], \tag{3.7}$$

where the instantaneous source function, $S(\nu, t)$, is given by the ratio of the instantaneous emissivity and opacity, which are both uniform in depth: $S(\nu, t) = \eta(\nu, t)/\kappa(\nu, t)$.

Despite the simplicity of this equation, to the author's knowledge no experimental demonstration of its application to a dense plasma has previously been reported. There are a number of reasons for this. Firstly, it is non-trivial to produce 'slabs'

of plasma with differing thicknesses, but otherwise identical, where the effects of longitudinal density and temperature gradients are unimportant. Secondly, in many cases, laser-driven plasmas suffer from the effects of self-absorption which affects their atomic-kinetics and the populations of the ground states, as well as the excited states (an effect that is often taken into account in simple treatments via an escape factor formalism [52, 84]). In the case described here, this is negligible: the high-intensity FEL dominates the population kinetics and allows the ground state populations to be set by LTE [55] – in other words, the emissivity $\eta(\nu, t)$ and opacity $\kappa(\nu, t)$, are not a function of thickness d. Finally, verifying the applicability of Eqn. 3.7 requires observing emission in both the optically thick ($\kappa(\nu, t)\, d \gg 1$) and thin ($\kappa(\nu, t)\, d \ll 1$) regimes, the latter requiring extremely thin targets at solid density – in this case just a few tens of nm – again necessitating rapid heating with no pre-pulse, and diagnosis on the sub-picosecond timescale of inertial confinement. As described above, this is made possible by using an FEL such as LCLS.

As expected from the behaviour of Eqn. 3.7, the observed lines in the thickness dependent emission in Fig. 3.3 increase in intensity as the target is made thicker. It is assumed that Eqn. 3.7 also holds in the time-integrated case,

$$\begin{aligned} \overline{I}(\nu, d, \theta) &= \int_t S(\nu, t)[1 - \exp(-\kappa(\nu, t)\, d/\cos(\theta))]\ dt, \\ &\approx \overline{S}(\nu)[1 - \exp(-\overline{\kappa}(\nu)\, d/\cos(\theta))], \end{aligned} \tag{3.8}$$

where the parameters κ and S in Eqn. 3.7 are replaced with their time-averaged values[2]. The time-integrated form in Eqn. 3.8 will be assumed to be identical to that in Eqn. 3.7 and the validity of this approximation is discussed further in Ch. 4.2.1. Furthermore, the thickness refers to the line-of-sight thickness $d_S = d/\cos(\theta_S)$ accounting for the viewing angle of $\theta_S = 20°$ to the nominal thickness. The ramifications of this

[2]From here onwards, unless otherwise explicitly stated, the parameters $\eta(\nu)$, $\kappa(\nu)$, $S(\nu)$, and $I(\nu, d, \theta)$ will refer to the time-integrated parameters of Eqn. 3.8.

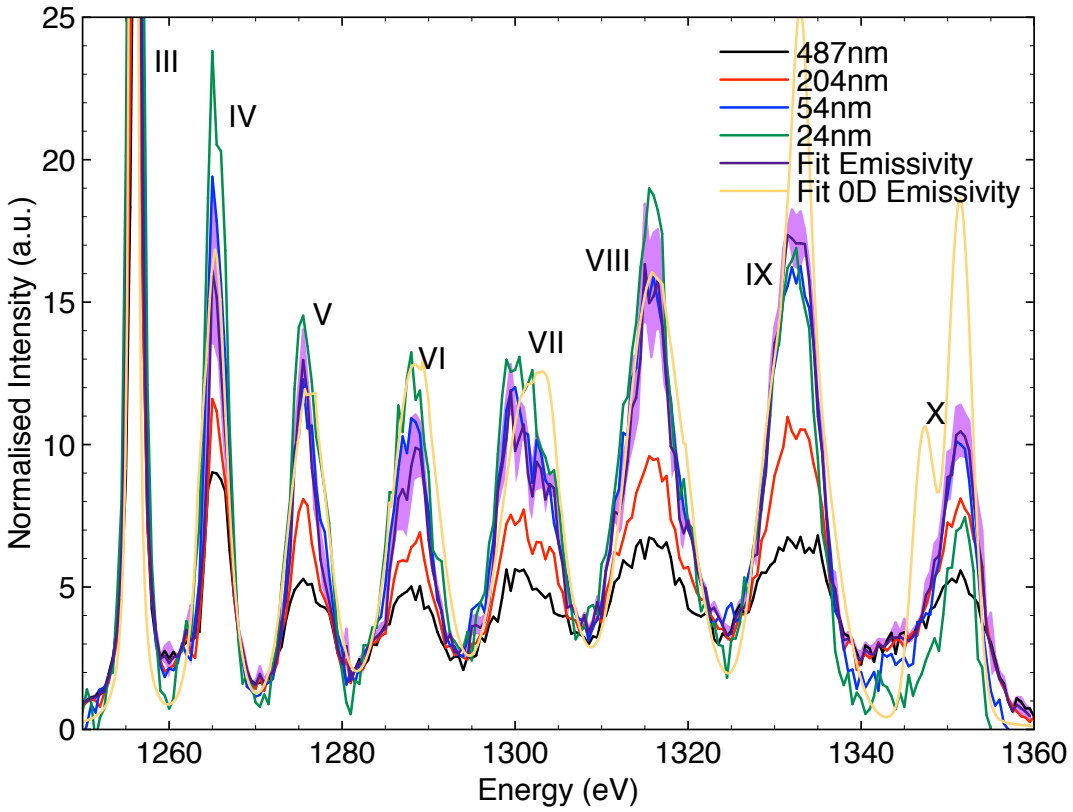

Figure 3.5: Experimental emission spectra for magnesium irradiated with an FEL photon energy of 1540 eV and FEL pulse energy of 1.8 mJ normalised to thickness and number of shots. The lines are labelled according to the charge state of the emitting ion. The plot also compares the normalised spectra with the emissivity extracted by fitting Eqn. 3.8 to the four curves, showing that the two thinnest targets tend to the optically thin limit. The 24 and 54 nm curves are consistent within the error due to the uncertainty on the target thickness. The coloured region around the fitted emissivity represents its error bar. Also shown is the fitted emissivity derived from fitting Eqn. 3.8 to simulated SCFLY spectra.

assumption will be discussed in Ch. 5, but essentially the line-of-sight just described is such that the maximum displacement between incoming and outgoing photons on the plane of the laser is well within the Half-Width-Half-Maximum (HWHM) of the beam profile, even for the thickest target, thus ensuring approximately uniform conditions in the region where radiation transfer occurs. Under these assumptions, for each frequency, the four data points corresponding to different thicknesses d are fitted to Eqn. 3.8 using $\eta(\nu)$ and $\kappa(\nu)$ as fit parameters.

The four data points and their standard deviation are fitted to the functional form

of Eqn. 3.8 using the function *curve_fit* in the *Python scipy.optimize* module [94]. This, in essence, employs a least-squares fitting algorithm to find the best-fit values for the parameters $[\eta(\nu), \kappa(\nu)] > 0$ using the Levenberg-Marquadt algorithm – an algorithm which is optimised for non-linear least-squares problems [95]. The solution is found iteratively for some sensible initial guess for the parameters. In the case with only one minimum (as with Eqn. 3.8) the algorithm easily converges to the global minimum. For a detailed description of how the algorithm works, see Ref. [95, Ch. 15.5]. The uncertainties on the original data points are used as weightings in the least-squares problem and the algorithm produces a covariance matrix of the optimal values of the parameters:

$$\mathrm{cov}(\eta, \kappa) = \begin{pmatrix} \sigma^2_{\eta\eta} & \sigma^2_{\eta\kappa} \\ \sigma^2_{\kappa\eta} & \sigma^2_{\kappa\kappa} \end{pmatrix} \tag{3.9}$$

The one standard deviation errors on the parameters are therefore given by $d\eta = \sigma_{\eta\eta}$ for the emissivity and $d\kappa = \sigma_{\kappa\kappa}$ for the opacity. The extracted opacity $\kappa(\nu)$ from this fit transpires to be a good measure of the peak opacity present within the system, and will be discussed below.

The time-integrated emission normalised both to the number of shots and to d for the four different target thicknesses is plotted in Fig. 3.5, together with the emissivity $\eta(\nu)$ obtained by the fit procedure and its error $d\eta(\nu)$. The signature of emission in the optically-thin limit is that the intensity normalised to thickness is independent of d, because if $\kappa(\nu)d_S \ll 1$ throughout the pulse, then $I(\nu, d, \theta)/d_S \to \eta(\nu)$ — the same for each target. The error bars on the 24 and 54 nm curves are such that those curves are consistent with each other and with the emissivity curve on the plot. Thus the emission from the two thinnest targets is optically thin over the whole spectral range, whilst for the two thicker targets opacity effects are evident at the peaks of the K-α emission from each ion, but the emission is still optically thin in the far wings of the transitions, i.e. the region between the K-α lines.

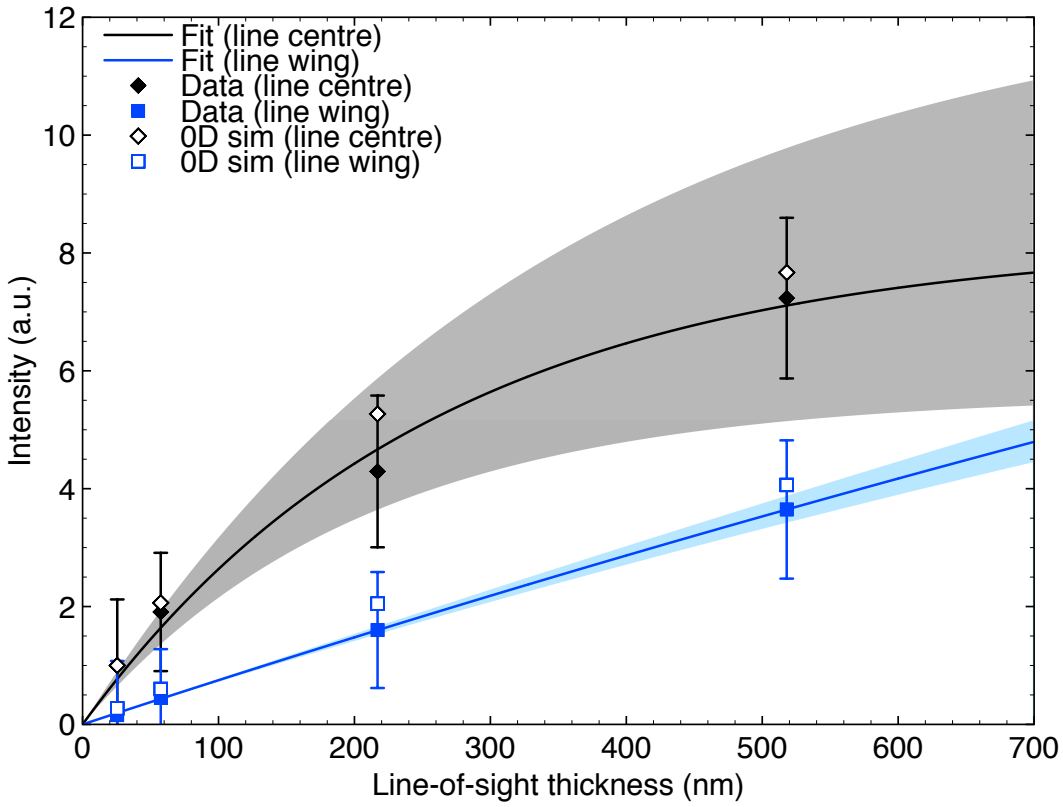

Figure 3.6: The intensity emitted by the four targets, either at a photon energy of 1315 eV (line centre), corresponding to the line centre of line VIII, or at 1325 eV (line wing), corresponding to the region between lines VIII and IX plotted against the line-of-sight thickness d_S. The latter curve approaches a linear trend in target thickness, consistent with it being representative of a low opacity region. The prediction of space- and time-integrated 0D SCFLY simulations (normalised to overlap the line-centre data for the 24 nm case) are also plotted for comparison. The error bars represent the standard deviation of the distribution of the observed intensities across the multiple shots acquired. Coloured bars indicate the error of the fit $I(\eta \pm d\eta, \kappa \mp d\kappa)$.

The curves described by Eqn. 3.8 for a given frequency resulting from the fit procedure are illustrated in Fig. 3.6 for the case of emission from line centre (specifically that of the Be-like ion, line VIII), and from line wings (between lines VIII and IX). The opacity for the line wing is low, so the fit looks linear in this case (given by the optically thin limit), whereas the line centre has a larger opacity, and here the intensity begins to saturate at larger thicknesses. As previously mentioned, the error bars on the four points in Fig. 3.6 arise from the standard deviation in combining the emission spectra from many shots. Also shown are coloured bars indicating the

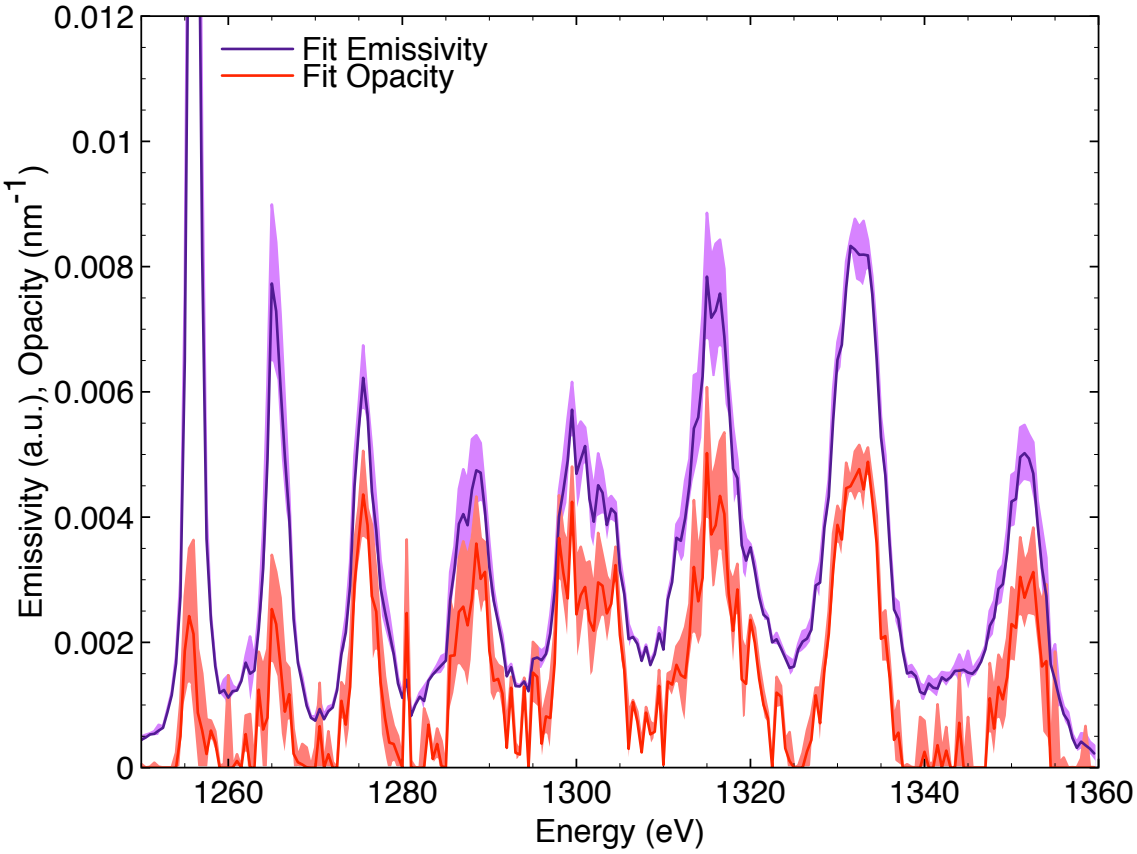

Figure 3.7: The opacity and emissivity, as a function of photon energy, obtained by fitting Eqn. 3.8 to the four intensities given by the experimental spectra for each photon energy in the spectral range of the spectrometer. The coloured region around the fitted emissivity and opacity represents their error bars.

maximum error on the fit, $I(\eta + d\eta, \kappa - d\kappa)$ and $I(\eta - d\eta, \kappa + d\kappa)$, using the standard deviation errors from the fit procedure.

The deduced, frequency-resolved values of the emissivity and opacity are shown in Fig. 3.7 and here the error bars come from the fitting procedure. It can be seen that the values of $\kappa(\nu)$ at the peaks of the K-α transitions, are of order 0.003 - $0.004\,\mathrm{nm}^{-1}$ and such values are consistent with 'integrated opacities' corresponding to $\sim 40\%$ of the peak opacities predicted by detailed atomic-kinetics calculations. The reason for this is discussed in Ch. 3.4.1.

To understand better the significance of the extracted $\kappa(\nu)$, how it relates to steady-state values of the opacity, and any effects due to transverse gradients, the

experimental data were simulated using the collisional-radiative code SCFLY [50] which has been shown to produce excellent agreement with previous experiments for LCLS interacting with solid targets [27, 30, 47, 53, 55]. These calculations are described in the following section.

3.4 Zero-dimensional SCFLY simulations

A series of time-dependent SCFLY simulations were performed to extract information about the density, temperature, and population evolution of the plasma at different input laser intensities. As discussed in Ch. 1, the only user input is the temporal profile of the X-ray drive which was assumed to be Gaussian with FWHM of 100 fs (assumed to be the same as the electron bunch duration) and a pulse energy of 1.7 mJ (reduced to 0.51 mJ to account for beamline transmission - measured as 30% [88]), centred at 1540 eV with a 0.5% bandwidth [4]. Previous work has shown that the detailed SASE temporal structure of the FEL pulse may be neglected [47]. At each time-step, SCFLY uses the calculated populations to calculate an instantaneous emissivity and opacity, and a thickness dependent intensity that obeys Eqn. 3.7. For each intensity, the emission spectrum is integrated in time, and then simulations at the different laser intensities are used to perform spatial integration across the measured focal spot [77]. As in previous work [27, 30, 47, 53, 55], an accurate match to the experimental spectra was found using this model and specific examples are shown later. More details are in Ch. 4.

3.4.1 Opacity

The space and time integrated emission from SCFLY, at two given emitted photon energies, is compared in Fig. 3.6 with the experimental data for the four thicknesses, and found to be a good match within the error bars. Whilst, of course by construction,

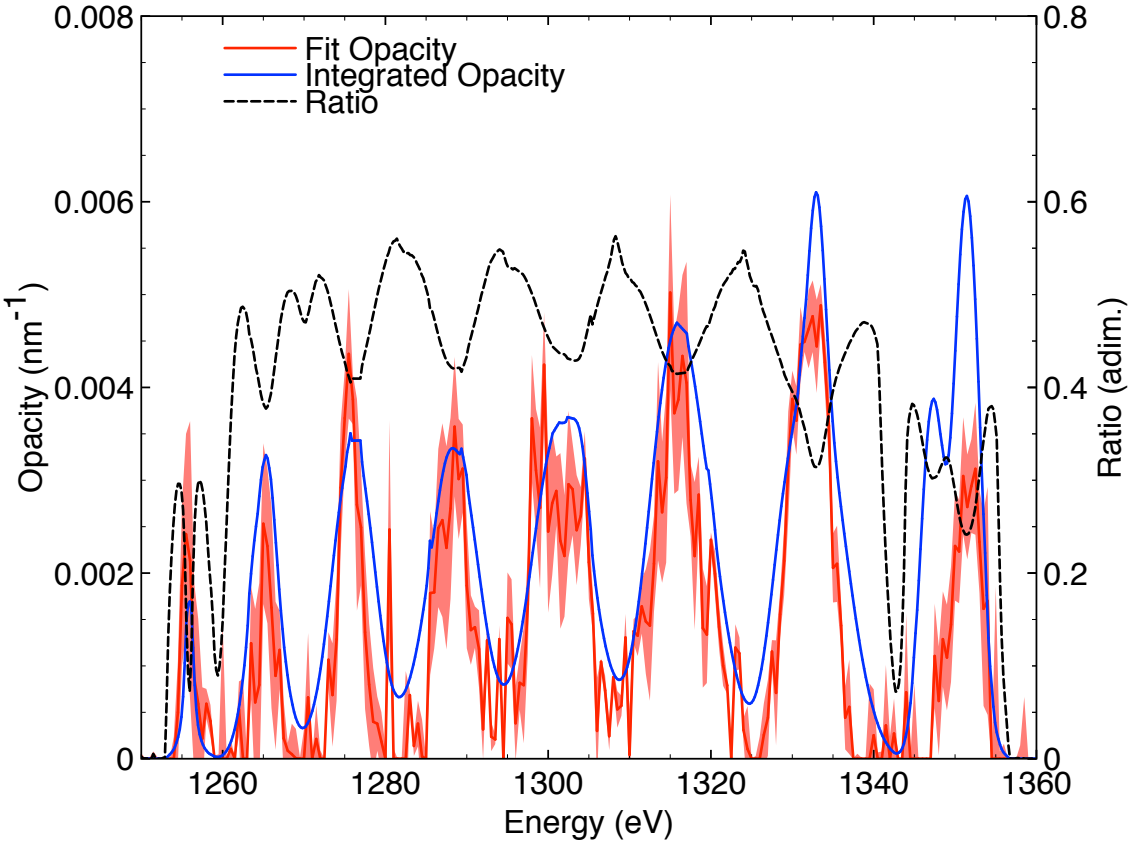

Figure 3.8: A comparison of the fitted experimental opacity $\kappa(\nu)$ with the integrated opacity derived from fitting Eqn. 3.8 to simulated SCFLY spectra. Also plotted is the ratio of this opacity to the instantaneous maximum opacity (black, dashed).

an instantaneous set of intensities for the four different targets matches perfectly Eqn. 3.7, the fact that the simulations correctly reproduce the trend shown in Fig. 3.6 also yields the non-trivial result that the same functional form is a good match to the time-integrated simulated data, even though $I(\nu, t, d, \theta)$ is not a linear function of time.

The reasonable match between the data and Eqn. 3.8, however, does not necessarily imply that the physical meaning of the fit parameter $\kappa(\nu)$, as plotted in Fig. 3.6 is that of a space- and time-integrated opacity: in order to understand its true meaning, shown in Fig. 3.8 is a comparison between the same experimental $\kappa(\nu)$, and an 'integrated opacity' generated by fitting Eqn. 3.8 to the space and time integrated spectra for four different thickness in exactly the same manner as described above for

the experimental data. Good agreement is found over the majority of the spectral range (agreement for the 'cold' K-α line of the first state is not expected, as this is sensitive to how much FEL energy is in the far wings of the FEL focal spot). Furthermore, these are also compared with the maximum instantaneous opacity at each photon energy that was observed during the simulation as the charge states evolved. Plotted in Fig. 3.8 is the ratio of the 'integrated opacity' extracted from the SCFLY simulations with the maximum instantaneous opacity calculated by SCFLY at that frequency. It is observed that at the peak of the K-α lines this ratio is reasonably consistent across the majority of charge states, varying from about 37% for line IV, up to 42% for line VI, and dropping to 32% for line IX. Such consistency provides confidence that these time and space averaged opacity measurements are accurate representations of the maximum opacity to within of order $\pm 4\%$.

The fitted experimental opacity also corresponds well to an a simple estimate of the peak bound-bound opacity [33, 64] which is given by:

$$\kappa(\nu) = N_l\Big(1 - \frac{N_u}{N_l}\frac{g_l}{g_u}\Big)\Big(\frac{\pi e^2}{mc}\Big) f_{lu}\phi(\nu), \tag{3.10}$$

where N_l is the ground state and N_u is the upper state population with degeneracies g, f_{lu} is the transition's oscillator strength, and $\phi(\nu)$ is the transition's lineshape.

SCFLY is a super-configuration atomic-kinetics code and subsequently it solves the non-LTE rate equations for generic configurations which contain the same electronic occupancy in each shell; for example it solves the rate equations for the super-configuration $K^2L^3 \equiv (1s)^2(2s2p)^3$ without reference to the individual configurations that contains, namely: $1s^2\,2s^2\,2p^1$, $1s^2\,2s^1\,2p^2$, and $1s^2\,2s^0\,2p^3$, which themselves contain terms including fine structure. Crucially, this simplification is valid for the high density plasmas of interest here as the individual configurations with the same principal quantum number are often found to be statistically populated. The line profiles

shown in Fig. 3.8 are envelopes that contain these individual configurations, populated statistically and in LTE, and the overall linewidth is determined by the combined broadening of individual configurations [50]. Ordinarily the lineshapes of individual terms (which contain fine structure) $\phi(\nu)$ are Voigt as they are a combination of the natural broadening (Lorentzian) and Doppler broadening (Gaussian). In this case the lineshape of an individual term is closely Lorentzian as the Gaussian contributions are small since the ion temperature is low. Often individual terms are then combined into an STA (super-transition-array) Gaussian width for ease of calculation at the atomic-kinetics stage [96].

As discussed in Ch. 1.3, the choice of IPD model ensures that the only bound shells are the K and L-shells. One consequence of this is the absence of satellite emission from lines involving spectator electrons in higher shells. It is therefore assumed that each emission line in Fig. 3.3 arises from one ionization stage with no contribution from satellites of its neighbours. The predictiveness of the simulated spectra, alongside measurements of the IPD [30] and simulations with the SP model which includes a bound M-shell [47, p. 10] (which were found not to match the onset of line emission as a K-edge is traversed), lend credence to this interpretation. However, a caveat is that this should not be expected to hold for the He-α line where, in the model for IPD used here, the M-shell is only just in the continuum and the binary nature of the choice of model forces it to be wholly unbound [32]. Satellite emission on the red-side of the resonance line is observed for this line in Fig. 3.3, indicating that it is partly beginning to rebind [43], and may be important for the He-α line-width measurement discussed further in Ch. 6.

In order to extract a line-centre opacity estimate, it is assumed that $N_l \gg N_u$ and this ground state population at its peak (e.g. for the 6+ ion stage) comprises around 40% of the total number of ions at solid density $n_i = 4.31 \times 10^{22}$ cm^{-3} (as evinced later in Fig. 3.10a). The oscillator strengths are tabulated and for line VI is

$f_{lu} = 5.8161$ [97]; in general for resonant K-L transitions these are of order $10^0 - 10^1$. Furthermore, the value at the peak of the Lorentzian lineshape $\phi(\nu_0) = 2/(\pi\Gamma_L)$ must be estimated from the natural broadening Γ_L. Since the radiative lifetime is long, the width is dominated by the Auger lifetime of the upper state which is of order 2 fs. This gives a width of $\Gamma_L \sim 2\,\mathrm{eV}$ and a maximum value of $\phi(\nu_0) \sim 0.3\,\mathrm{eV}^{-1}$ at its peak. An estimate for the line centre opacity assuming most the population corresponds to the ground state term in the resonance line is therefore:

$$\kappa(\nu_0) \sim N_l\Big(\frac{\pi e^2}{mc}\Big) f_{lu}\phi(\nu_0) = 0.0087\,\mathrm{nm}^{-1}, \tag{3.11}$$

using $N_l \sim 1.7\times10^{22}\,\mathrm{cm}^{-3}$ and $f_{lu} \sim 5.8$. Note that this is just for one individual term which contributes to a super-configuration. In reality there will be a number of closely spaced overlapping Lorentzian lines with differing oscillator strengths that contribute to the overall envelope of the lineshape which is then configurationally broadened – lumping them together into the STA width. Here, the simplifying assumption is made that only one of these term's Lorentzians contributes to the emission at the centre of the envelope which provides a lower limit on the estimate of $\phi(\nu_0)$. This maximum opacity at the line centre is in good agreement with the parameters shown in Fig. 3.8. Finally, the measured opacity is lower than this due to the rise and fall of the charge state as a function of time and gives a time-averaged opacity that is $\sim 40 - 55\%$ of that at the instantaneous maximum, yielding a value of $0.0035 - 0.0048\,\mathrm{nm}^{-1}$ which compares well with the fit to the data. This result is justified later in Ch. 4.2.1 assuming that the rise and fall is approximately Gaussian as evinced later in Fig. 3.13.

This Gaussian approximation breaks down for the higher energy lines and the extracted opacity as a fraction of peak opacity drops. The reason for this is because these charge states are around for a longer time and so the rise and fall as a function of time is no longer Gaussian over a narrow temporal window, and furthermore the

population in the upper state is comparable to the population in the lower state and one can no longer neglect this population. Furthermore, the ground state population of the He-like ion continues to increase as a function of time after the laser switches off because nearly all decay channels, at the high final temperature, lead to this state.

3.4.2 Source Function

Of further interest is the shape of the source function given by the ratio of the emissivity and opacity. The bound-bound emissivity [33, 64] is:

$$\eta(\nu) = N_u A_{ul} \Big(\frac{h\nu_{ul}}{4\pi}\Big) \phi(\nu), \tag{3.12}$$

where, as in Eqn. 3.10, N_u is the upper state population, A_{ul} is the transition's spontaneous emission rate, ν_{ul} is the transition frequency, and $\phi(\nu)$ is the transition's lineshape. Complete redistribution is assumed so that the emissivity has the same lineshape as the opacity in Eqn. 3.10. The oscillator strength is related to the A-rate by [64]:

$$A_{ul}\Big(\frac{h\nu_{ul}}{4\pi}\Big) = \Big(\frac{2h\nu_{ul}^3}{c^2}\Big)\Big(\frac{\pi e^2}{mc}\Big) f_{lu}. \tag{3.13}$$

Taking the ratio of the emissivity with the opacity in Eqn. 3.10 gives the frequency-independent source function:

$$S(\nu) = \Big(\frac{2h\nu_{ul}^3}{c^2}\Big) \frac{N_u}{N_l} \frac{g_l}{g_u} \Big(1 - \frac{N_u}{N_l} \frac{g_l}{g_u}\Big)^{-1}. \tag{3.14}$$

This is a standard result and only depends on the ratio of the upper and lower state populations. It varies weakly with frequency as the emission and absorption lineshape profiles are identical. Its equivalence with Planck's law (a black-body spectrum, defined in Eqn. 2.2) is evident for the case where the upper and lower states are

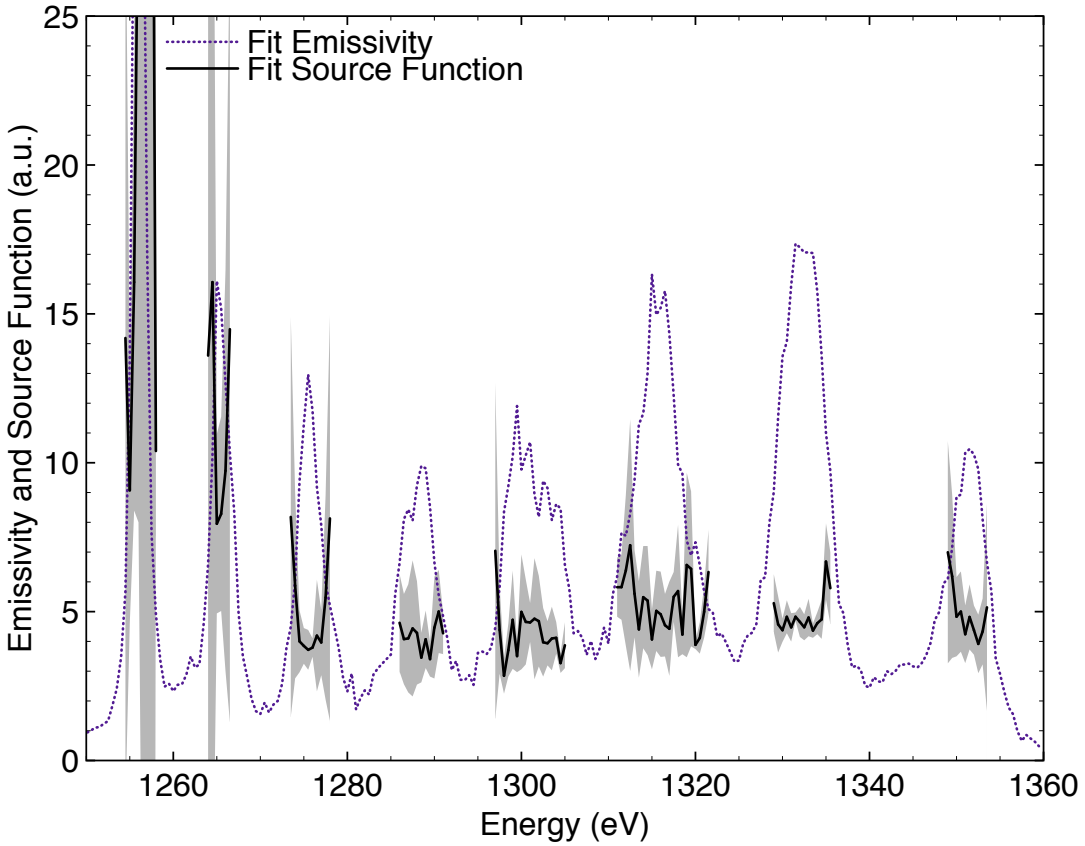

Figure 3.9: The source function, as a function of photon energy, obtained by fitting Eqn. 3.8 to the four intensities given by the experimental spectra for each photon energy in the spectral range of the spectrometer. Sections of the curve from the line-wings have been omitted as the ratio of the emissivity to the opacity varies unreliably here. Also shown is the emissivity as in Fig. 3.7. The coloured region around the fitted source function represents its error bar found by combining the errors in the emissivity and opacity: $dS = S\sqrt{(d\eta/\eta)^2 + (d\kappa/\kappa)^2}$.

populated thermally by Boltzmann's distribution at a temperature T:

$$\frac{N_u}{N_l} = \frac{g_u}{g_l} \exp\Big(- \frac{h\nu_{ul}}{k_B T}\Big). \tag{3.15}$$

However, for the K-L transition the temperature is too low to populate the upper level thermally and its population closely follows the laser intensity, whilst (as described in the next section) the lower state's population is set by LTE conditions. Hence, one would expect a constant ratio of upper to lower state populations and the source function to not vary with the lineshape. This is exactly what is observed ex-

perimentally in Fig. 3.9: across the middle of each line the source function is flat and similar for each emission line, reflecting the fact the ratio of the (super-configuration) states is dictated by the driving FEL, and individual terms are in LTE. Taking the instantaneous source function from SCFLY gives the same shape as that observed experimentally (flat across a line shape) with the steps rising and falling in time with the populations. However in SCFLY this would be expected by definition, as it is assumed *a priori* that the individual terms within a superconfiguration are in LTE and statistically populated [50]. This is never assumed in the fit to the data from one frequency to the next. Indeed, the experimental observation of a flat source function is a direct consequence of the individual terms in the emission lines existing in LTE and further evidence that the extracted emissivity and opacity as a function of frequency are meaningful descriptors of the conditions in the plasma. It is reassuring that the fitted source function is flat as a function of frequency for each emission line, especially given that no assumption on neighbouring frequencies is made by the fitting procedure.

Furthermore, inverting Eqn. 3.14 to solve for $\frac{N_u}{N_l}\frac{g_l}{g_u}$ from the SCFLY source function gives the expected ratio of populations and this ratio is roughly constant for each ionization stage, confirming that, internally, SCFLY is behaving consistently.

3.4.3 Population evolution

Further insight is gleaned from the SCFLY simulations by considering the computed charge state distribution and level populations as a function of time. In Ch. 3.4.1 it was shown that the deduced experimental opacity is consistent with the opacity deduced from SCFLY simulations. The physical explanation for this is that under LTE conditions, the ratios of the ionization states are dictated by Saha equilibrium, and the absorbing ground states which determine the opacity appear under the same temperature and electron density conditions as they are swept through in time regardless

of the target thickness.

To confirm this is the case, the charge state distribution and temperature as a function of time is compared with the Saha equilibrium case. In Saha equilibrium [33, 64]:

$$\frac{\Xi_e \, \Xi_{Z+1}}{\Xi_Z} = \frac{n_e \, n_{Z+1}}{n_Z}, \tag{3.16}$$

where Ξ_e is the electronic partition function, and Ξ_Z the partition function of the ion with charge Z; n_e is the electron density, and n_Z the density of ions with charge Z. This is greatly simplified in the case of this experiment: because the heating is isochoric [27], the sum of the populations of the ion stages is constant and given by the ion density $n_i = 4.31 \times 10^{22}\,\mathrm{cm}^{-3}$. For a given temperature, one then just needs to solve iteratively for the mean charge state $\overline{z} = n_e/n_i$. Substituting for the partition functions [64], Eqn. 3.16 simplifies to:

$$\frac{n_{Z+1}}{n_Z} = f(Z, T, \overline{z}) = 2\Big(\frac{2\pi e m_e}{h^2}\Big)^{3/2} T^{3/2} \, \frac{g_{Z+1}}{g_Z} \frac{\exp(-I_Z/T)}{\overline{z} n_i}. \tag{3.17}$$

where the degeneracies, g_Z and ionization energies, I_Z (including IPD according to the neutral atom model [48]) match those used in SCFLY. Here, e is the electronic charge, m_e the electronic mass, and h is Planck's constant. Note that crucially the temperature T is too low to excite K to L transitions, and since only those two shells are bound, Boltzmann distributions of states (as described in Eqn. 3.15) other than the ground state need not be considered [47].

From a first guess of $\overline{z}$ the ratio of subsequent charge states is found using Eqn. 3.17. Imposing conservation of nucleii,

$$\frac{n_i}{n_2} = \sum_{z'=2}^{Z} \frac{n_{z'}}{n_2} = 1 + \frac{n_3}{n_2}\Big(1 + \frac{n_4}{n_3}\Big(1 + \frac{n_5}{n_4}\Big(1 + ...\Big)\Big)\Big), \tag{3.18}$$

allows one to solve for n_2/n_i and then calculate all subsequent populations. Note

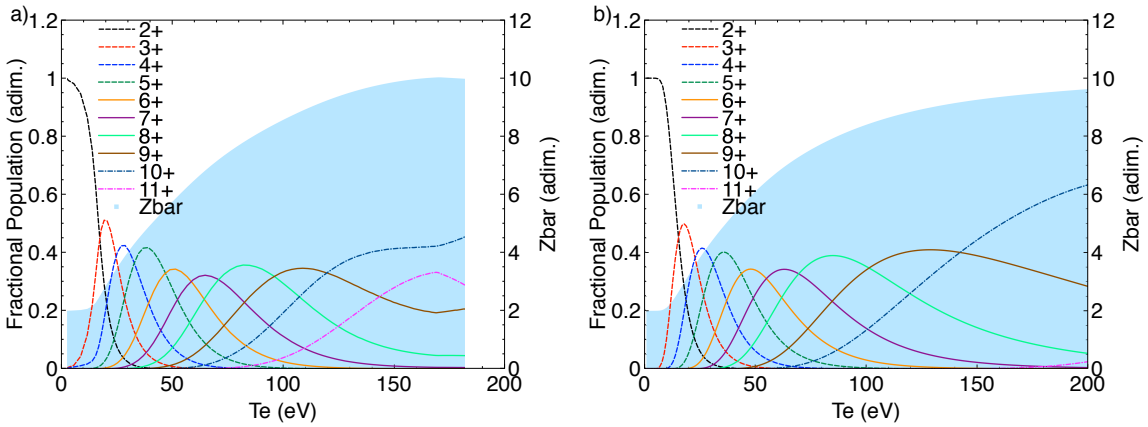

Figure 3.10: a) Charge state distribution, and mean charge state $\overline{z}$ (Zbar) evolution as function of electron temperature for all ionization stages at peak laser intensity for the case where the sample is driven by the FEL. b) Charge state distribution as function of temperature given by Saha equilibrium. The case driven by the FEL is very similar to the Saha equilibrium case.

that the cold ground state is forced to be Mg^{2+}, in this nomenclature n_2, and so the solution to this is robust for any starting value of $\overline{z} \geq 2$. From these populations one then solves for

$$\overline{z} = \sum_{z'=2}^{Z} z' \frac{n_{z'}}{n_i}, \tag{3.19}$$

the mean charge state, and this can then be used as the next guess until convergence is found.

The equilibrium charge state distribution as a function of temperature is a good match for that from the non-LTE SCFLY simulations, which gives confidence that the measurements are made under conditions very close to LTE (for the ground state populations). Whilst the case shown in Fig. 3.10a is at peak laser intensity, the differences away from the focal spot are minimal. For lower laser intensities the final temperature and density obtained is lower and so the evolution with temperature shown in Fig. 3.10a is identical, except truncated at this lower temperature.

Furthermore, the assumption that the partition functions of the ions are dictated solely by their ground states transpires to be excellent. The textbook Saha formula of Eqn. 3.17 was compared with the LTE solver in SCFLY, which includes all excited

states that may be populated (in this case, only a small subset since all shells above the M-shell are unbound due to IPD). The evolution of the charge states as a function of temperature is exactly identical to that shown in Eqn. 3.10b. The only small deviation from Eqn. 3.17 is at high temperature ($\sim 200\,\mathrm{eV}$) where the upper state of the helium-like ion (K^1L^1) has around 2% of the population of the helium-like ground state (K^2L^0). All charge states lower than Li-like have upper state populations that are $< 1\%$ of the ground state at $T = 200\,\mathrm{eV}$. Consequently, the underlying assumptions of Eqn. 3.17 are very good.

However, there are effects of the FEL that are worth noting. Primarily, the driving effect of the laser is to shift the production of charge states to higher temperatures. As an example, the 3^+, 4^+, and 5^+ peak at slightly higher temperatures, and further, at the end of the pulse, the 11^+ is populated but not in the Saha equilibrium case. This is because, when the laser is on, the 11^+ ionization stage comes from the K^0L^1 super-configuration (with negligible contribution from its ground state - K^1L^0), which isn't thermally populated in the Saha case for two reasons: the temperature isn't high enough to appreciably ionize up to hydrogenic ions, and even if it were, the temperature is again too low to excite this electron into the L-shell.

Further differences arise between the driven and LTE simulations because the charge states in the laser-driven case include the photoionized states of the form K^1L^N. For example, the charge state 8^+ in Fig. 3.10 includes all super-configurations that have 4 electrons and so is comprised of the super-configurations $K^1L^3 + K^2L^2$. In order to definitively tease out the effect of the FEL, a better comparison would be the states that have the same number of L-shell electrons and so to compare the states $L^N = K^1L^N + K^2L^N$ as this captures the ground state of an ionization stage (K^2L^N) and the (for the most part) small number of these which have then been photoionized (K^1L^N) by the FEL.

Shown in Fig. 3.11 is the deviation of the populations L^N for the SCFLY simulation

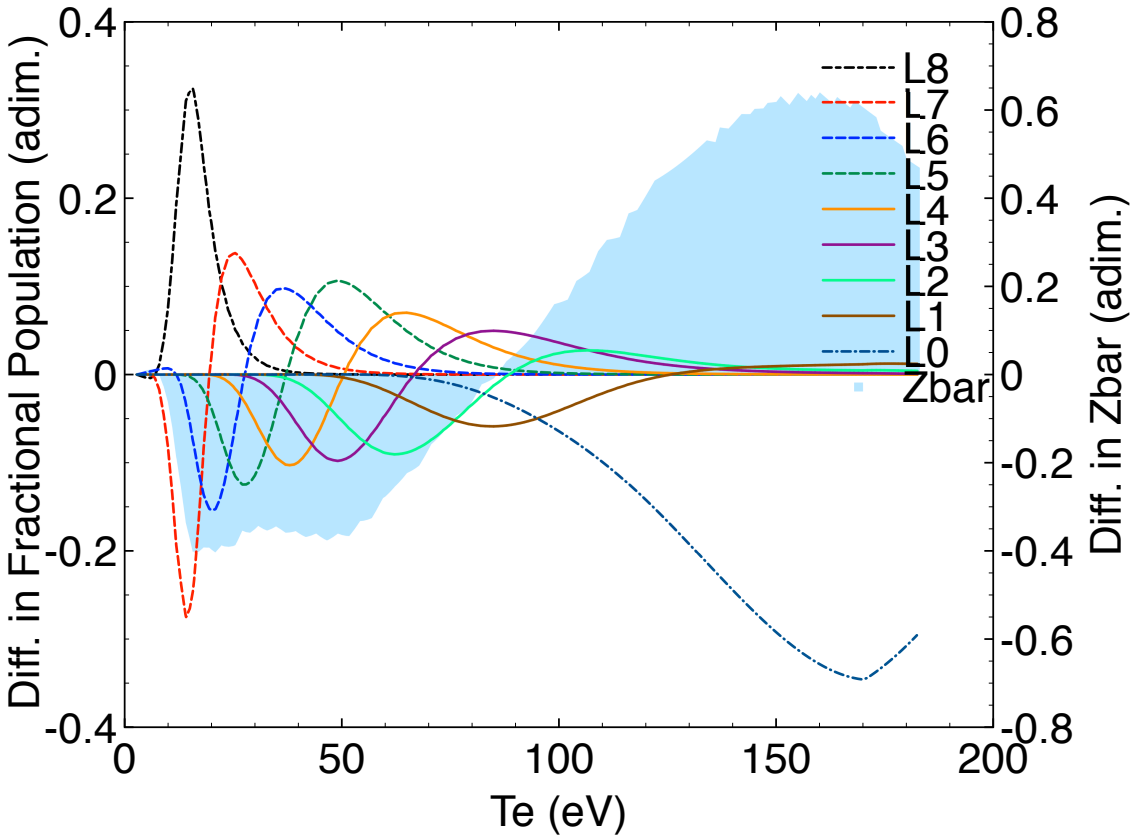

Figure 3.11: Deviation of level populations at peak laser intensity as a function of temperature from the Saha equilibrium (LTE) case, including the ground states of the form K^2L^N, and the upper states that have been photoionized by the FEL of the form K^1L^N. Also shown is the deviation of the mean charge state $\overline{z}$ (Zbar). Values greater than zero indicate that the population is greater in the driven case than in Saha equilibrium.

driven by the FEL, from the Saha LTE case, for all states up to $L^0 = K^1L^0 + K^2L^0$, (i.e. $[K^1L^N + K^2L^N]_{FEL} - [K^2L^N]_{LTE}$), and the deviation of the mean charge state $(\overline{z}_{FEL} - \overline{z}_{LTE})$, both as function of temperature. This provides an estimate for how far the system is driven from LTE by the FEL. In general, the ground states peak at slightly higher temperatures and this effect is most pronounced earlier in the pulse (at lower temperatures). The higher charge states are much closer to LTE: they show less pronounced deviations from the Saha equilibrium case.

Perhaps most interesting are the L^1 and L^0 curves. The first shows a much smaller deviation at high temperatures when this state is populated. Here the upper state

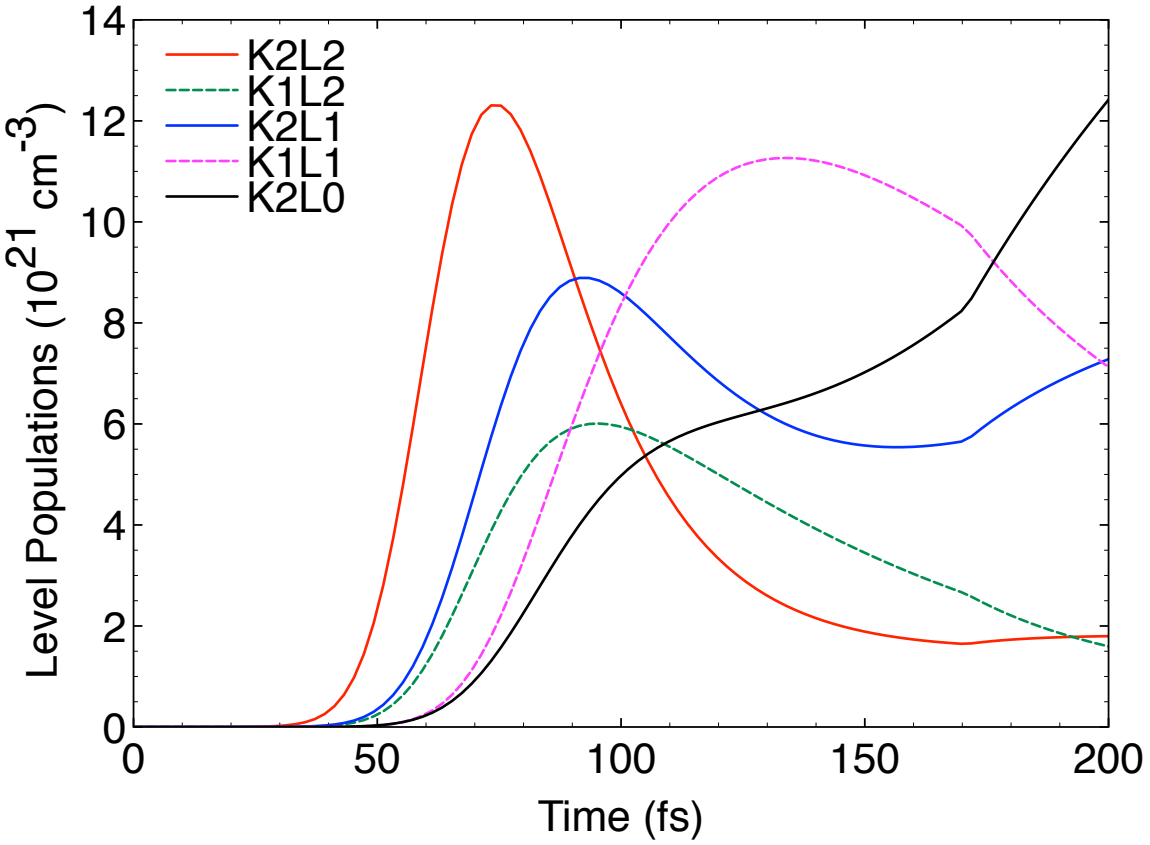

Figure 3.12: Time evolution of the population of the ground states (K^2) and photoionized (K^1) charge states of the Be-like, Li-like, and He-like ions. Ground states are solid lines and photoionized states in dashed lines. Here the photoionized populations exceed the ground states late in the pulse and populations tend towards the He-like ground state K^2L^0.

K^1L^1 cannot be rapidly depleted by Auger recombination and so is much longer lived. The K^1L^1 state has a spontaneous emission rate (defined in Eqn. 3.13) that gives it a lifetime of 271 fs – much longer than the driving laser pulse. It is therefore much more likely to be found under the same temperature conditions as the Saha case as shown in Fig. 3.12. Further, once this is the dominant charge state, the amount of heating provided by the PI and A processes of Eqn. 3.2 is smaller and therefore these states exist over a much wider temperature range. The L^0 curve differs as the laser prematurely drives the Li-like ground state (K^2L^1) up to the He-like ground state (K^2L^0) through a photoionization process followed by radiative recombination. If,

however, the aforementioned long-lived K^1L^1 state undergoes further photoionization before it can relax back to the He-like ground state, K^2L^0, it will create a hydrogenic ion with a double core hole K^0L^1 which is very unlikely to recombine back to the hydrogenic ground state before the end of the laser pulse – for the Ly-α transition the A-rate gives a decay time of 103 fs. The specific mechanism for this series of transitions is written:

$$\begin{aligned} K^2L^1 + h\nu_{FEL} &\xrightarrow{PI} K^1L^1 + e^-, \\ K^1L^1 + h\nu_{FEL} &\xrightarrow{PI} K^0L^1 + e^- \xrightarrow{KL} K^1L^0 + e^- + h\nu, \end{aligned} \tag{3.20}$$

and the emerging photon is that of the Ly-α transition. Recall, as mentioned earlier, that the population of the hydrogenic ions is almost entirely in the upper state as not only are they not created thermally, but neither is the FEL photon energy high enough to photoionize K^2L^0 up to the hydrogenic ground state K^1L^0. These are not included in the curves shown above which only go up to K^2L^0, and so it would appear that this population is larger for the Saha equilibrium case.

Of further interest are the populations of the photoionized single and double core hole states which in fact exceed the ground state populations at later times for the Be-like, Li-like, He-like ions in Fig. 3.12. This is to be compared with the lower charge states where the percentage of ions with a core hole is small (see Fig. 3.13) and the approximation that the driving effect of the FEL on the populations is small still holds. In other words, it could be assumed that most of the population is in the state K^2L^N with a small number ionized to K^1L^N. Clearly, at late times and for the higher charge states this assumption breaks down.

The temporal window over which a charge state emits is, in general, limited by the photoionization rate, which is much higher than the A-rate. The radiative lifetimes of each charge state are long (~ 100 fs) mirroring the low X-ray fluorescence yield (3%), but due to photoionization by LCLS photons and rapid radiationless recombination

these states are quickly burnt through to higher charge states. However, once the driving laser is switched off, the upper state of the He-like ion is no longer being populated by photoionization, as can be seen in Fig. 3.12. Given that it then falls off exponentially as a function of time, it would take approximately 800 fs to drop to a level below 2% that would be expected thermally. This time-scale is shorter than the electron-phonon coupling time [54] and much shorter than the target disassembly time.

Finally, over the entire temperature range the deviation of the mean charge state in the driven case from the LTE case is less than one charge state, which is equivalent to a difference in the electron density of $< 10\%$.

3.4.4 Temperature and density evolution

Now that the charge state distribution has been shown to be near LTE, and as a function of temperature does not depend on laser intensity, it remains to discuss what effect the spatial and temporal evolution of our plasma across the whole focal spot has on the extracted opacity.

To ascertain what effect this would have on the extracted opacity it is informative to go deeper than the charge state distribution and consider the super-configuration level populations. As an example, consider a particular mid-range charge state that has 4 electrons in the L-shell; its simulated charge state population history is shown in Fig. 3.13. These are the same charge states shown earlier in Fig. 3.4. Early in the FEL pulse the target is at low temperatures and this ion-stage does not exist, and no emission is produced from it. Later in the FEL pulse, owing to the combination of photo- and collisional ionization, the charge state K^2L^4 starts to be populated, and K-shell holes within it (K^1L^4) can be created via photoionization. Emission is recorded from the filling of these core holes ($K^1L^4 - K^2L^3$). At the same time the next charge state up K^2L^3 is also being produced, and it is this state that is

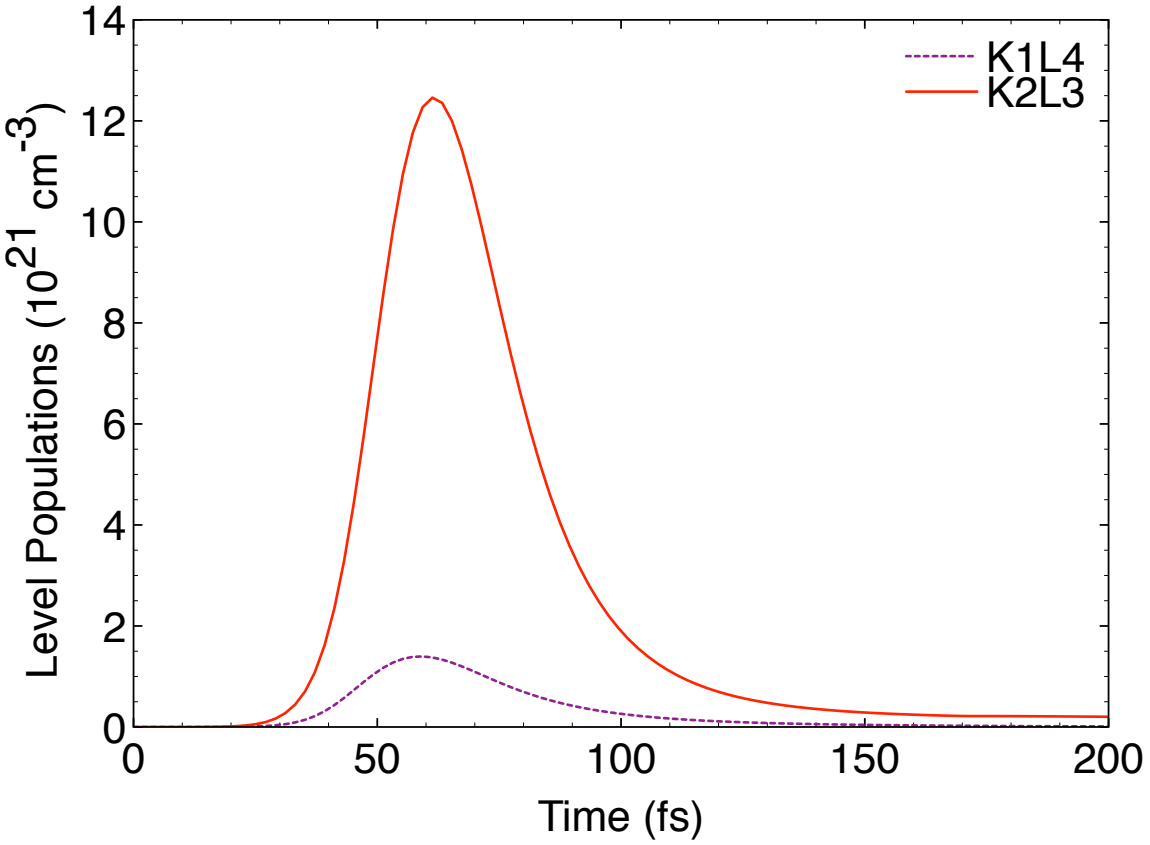

Figure 3.13: Time evolution of the population of the absorbing (K^2L^3) and emitting (K^1L^4) charge states for line VII, showing that the information provided by the spectra on the opacity arise from a relatively narrow temporal window. The low level of the population with a core hole shows that the deviations from LTE populations in the system are small.

responsible for the majority of the opacity. Later in time, this ion-stage has been depleted and no longer contributes K-α photons. Hence, the measured time-averaged opacity is weighted towards regions of both high emission and high opacity at the relevant frequency, and because emission is only observed when the populations of the ion-stages are high, the measurement is effectively gated in time.

However this is far from being a disadvantage: as shown in Fig. 3.13 for emission line VII, the population of both emitting and re-absorbing states for a given K-α line rise and fall within a relatively narrow temporal window, which implies that the opacity inferred from fitting the emission spectra is both weighted towards the time

at which the opacity of a given line is close to its maximum, and also arising from a time window which limits the variations of the plasma conditions.

In a similar way to Vinko et al. [53] the mean temperatures and densities at peak emission can be extracted, along with their corresponding standard deviations: $\{\overline{T} \pm \sigma_T,\ \overline{n}_e \pm \sigma_{n_e}\}$. The mean $\overline{X} = E(X)$, where X is the temperature or density, is given by:

$$E(X) = \frac{\int_A \int_t X(A,t)\,\eta(A,t)\,dA\,dt}{\int_A \int_t \eta(A,t)\,dA\,dt}, \tag{3.21}$$

using the instantaneous emissivity $\eta(A,t)$ as a function of enclosed area A and time t as a weighting function. The standard deviation σ_X of the temperature or density is the second moment of the distribution and is given by:

$$\sigma_X = \sqrt{E(X^2) - (E(X))^2}, \tag{3.22}$$

The fitted opacity and emissivity plotted in Fig. 3.7 for line VI is thus constrained to conditions of temperature $T = 45 \pm 15\,\mathrm{eV}$ and density $n_e = 230 \pm 48 \times 10^{21}\,\mathrm{cm}^{-3}$, whilst the spanned range of conditions goes from $\{T = 12 \pm 6\,\mathrm{eV},\ n_e = 100 \pm 20 \times 10^{21}\,\mathrm{cm}^{-3}\}$ for the cold K-α, to $\{T = 117 \pm 30\,\mathrm{eV},\ n_e = 380 \pm 30 \times 10^{21}\,\mathrm{cm}^{-3}\}$ for the He-α line. This range of conditions is shown in Fig. 3.14 for each line, with each sequential line emerging from a target which is hotter and denser.

Finally, it is worth commenting here about one of the merits of the approach using an FEL. As was seen in Fig. 3.14, each charge state appears under different temperature and density conditions. In essence this experiment corresponds to several traditional opacity experiments under different conditions, where the emission (and opacity) of each charge state (or line in the spectrum) is gated in a short ($\sim 10-30\,\mathrm{fs}$) window. This can all be achieved using just one LCLS pulse acting as a simultaneous pump and probe. The X-rays are used to heat the target through the photoionization and Auger recombination chain of Eqn. 3.2, and simultaneously the emissivity and

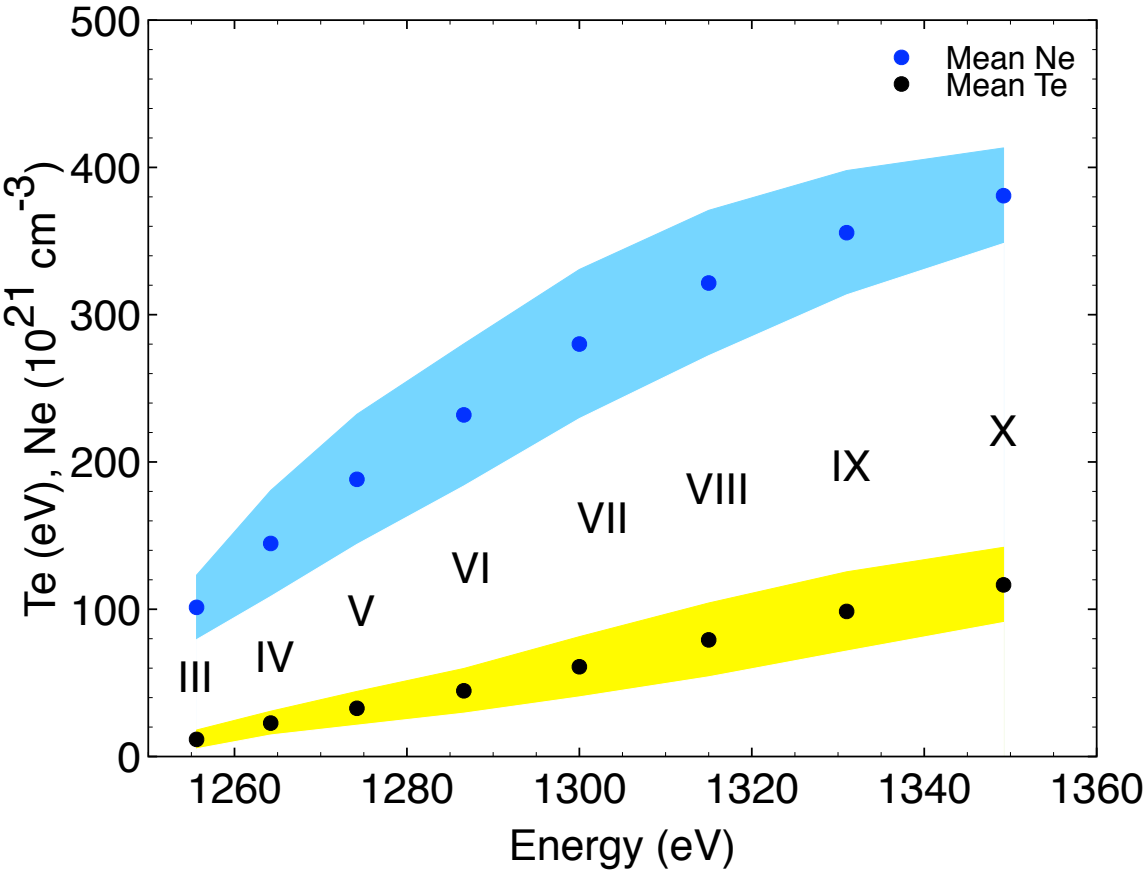

Figure 3.14: Mean temperature and density weighted by the emissivity as a function of frequency labelled according to the charge state of the emitting ion. Error bars are the standard deviation of the distribution.

opacity of each line are revealed through the radiative recombination of Eqn. 3.1 gated in conditions that are close to LTE for the absorbing state.

3.5 Conclusions

In conclusion, LCLS has been used to create hot Mg plasmas of varying thickness at exactly solid density, allowing the extraction of a measure of the opacity in a solid-density plasma in near-LTE conditions. The values of the opacity extracted from fitting the data using the uniform slab solution to the radiative transfer equation, were compared with the opacity obtained in detailed predictive atomic-kinetics simulations; such comparison shows that the opacity extracted from the fit has the

physical meaning of a line opacity integrated over a short time window, where both emitting and absorbing charge states for a given K-α line are populated. As such, it also corresponds to a certain fraction of the peak opacity, which in the case discussed here is around 40% of its value, and also compares well to an 'integrated opacity' deduced from fitting to SCFLY simulations. The reason for the 40% value is explained later in Ch. 4.2.1. As the absorbing ions are ground state ions, which largely obey an LTE population distribution, the fit provides a measure of solid-density LTE opacity. Furthermore, the source function behaves as expected from atomic-kinetics calculations. The short emission window also allows the extraction of mean temperatures and electron densities over the emission window for each K-α line. This method of extracting opacity from the variation of intensity with target thickness may complement methods based on absorption [59, 79].

Chapter 4

Robustness of deduced Opacity to variations in conditions

Now that the experimental data has been introduced, in this Chapter further modelling of it is discussed. First, the effect of altering the temporal parameters of the laser pulse on the emission spectra and deduced (fitted) opacity are explored, including its shape, length, and energy content. Crucially, the derived opacity is found to be relatively insensitive to changes in the pulse parameters. Furthermore, the assumptions used in the simple 1D slab solution to the equation of radiative transfer (Eqn. 3.7) are investigated in detail. This includes the approximation that arises from assuming that the time-integrated equation in Eqn. 3.8 has the same form as Eqn. 3.7, as well as the fundamental assumption that the emissivity and opacity do not depend on the thickness d. Both these assumptions are found to be very good for the purposes of the work presented in this Thesis.

4.1 Modifications to the X-ray drive

In Ch. 3.4 it was shown that the data may be adequately modelled using an X-ray drive which was assumed to be Gaussian with FWHM of 100 fs and a pulse energy of

1.7 mJ (reduced to 0.51 mJ to account for beamline transmission), centred at 1540 eV with a 0.5% bandwidth. SCFLY is designed to reproduce the data with minimal input from the user; given that the only user input is the temporal X-ray drive it is prudent to investigate this further.

In this section, three of these assumptions about the FEL pulse are tested: the shape of the pulse, its length (FWHM), and its energy content. Not considered is the X-ray photon energy and bandwidth for two reasons. Firstly, the bandwidth has been measured to be narrow [4] and is much smaller than the energy gap between K-edges. This was exploited previously in measurements of the Ionization Potential Depression which relied on a narrow bandwidth FEL and accurately known photon energy in order to determine the crossing of an emission threshold [30]. Secondly, the photoionization cross-section $\alpha(\nu)$ (in cm^2) as a function of frequency ν (in Hz) which enters the photoionization rate in SCFLY [51, 98] is given by:

$$\alpha(\nu) = 4.12 \times 10^{26} \frac{I_n^{5/2}}{Q_n} \nu^{-3} \tag{4.1}$$

where I_n is the ionization potential of an electron in the n'th shell, and Q_n is the screened charge as described in Chung et al. [51]. This varies weakly as ν^{-3} over the range of interest. For instance, getting the FEL photon energy wrong by ± 5 eV would lead to an error in $\alpha(\nu)$ of $< 1\%$. Provided that one probes above the K-edge for the He-like ion, then the photoionization rate, and consequent atomic-kinetics calculation, is insensitive to the choice of photon energy within a few eV.

4.1.1 Pulse shape

Firstly, the driving laser profile is in general assumed to be Gaussian centred at 100 fs, with a FWHM of 100 fs and a hard cut-off at 170 fs. The simulation is allowed to evolve in time from $0 - 200$ fs and the output is chosen for 100 time steps spaced by

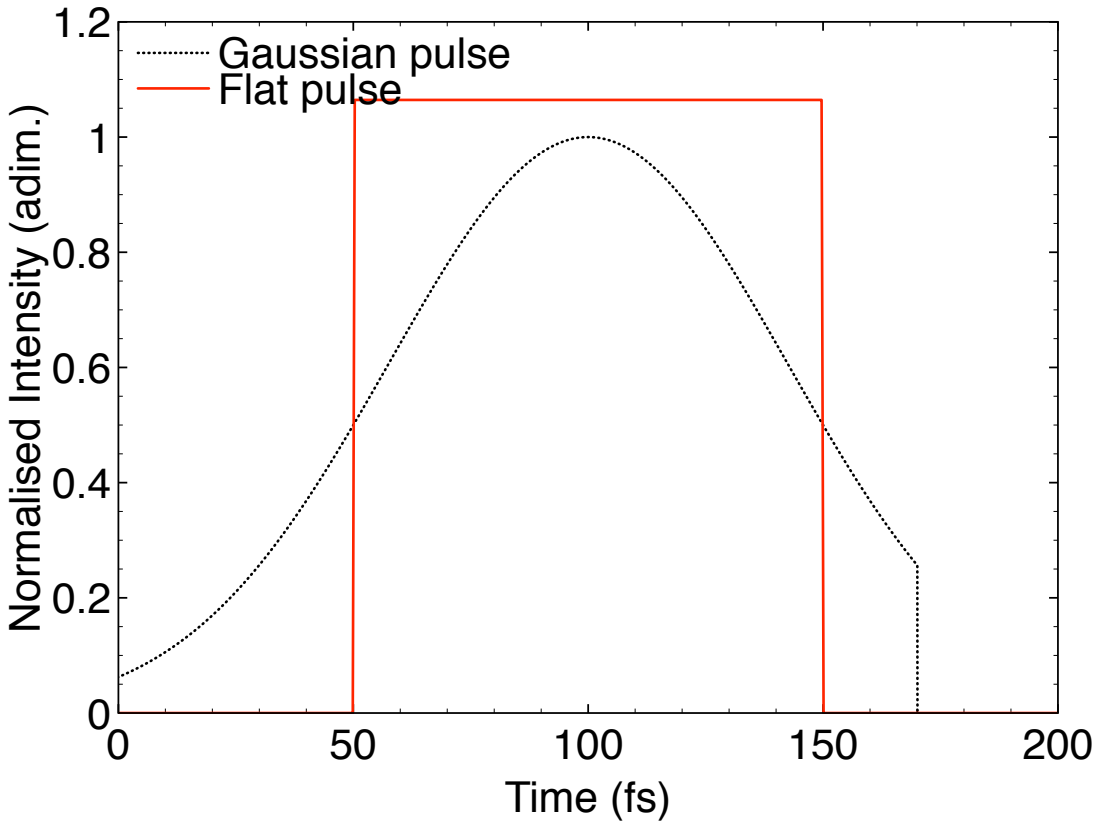

Figure 4.1: A comparison of the nominal Gaussian pulse (black, dotted) with FWHM of 100 fs, and peak at 100 fs, with a flat pulse (red, solid) with the same FWHM and same fluence.

~ 2 fs. Internally, the time-steps used are much smaller and so consequently increasing the number of time steps has a negligible effect on the time-integrated spectra.

In previous work, it was found that simulations are predictive regardless of the details of the temporal pulse, provided that the pulse's fluence and spatial distribution are correct [47]. Furthermore, the SASE (Self-Amplified Spontaneous Emission) nature of the LCLS source, which is characterised by chaotic spikes [99], is found to not effect the details of the time-dependent evolution of the plasma [47].

This work is extended here by considering not only a Gaussian pulse in time but also a flat (top hat) pulse. The Gaussian pulse is defined as:

$$g(t, p, w) = \exp\left(\frac{-(t-p)^2}{2w^2}\right), \tag{4.2}$$

where t is the time, p is the peak time, and $w = W_{FWHM}/2\sqrt{2\ln 2}$, the Gaussian width in terms of the FWHM width W_{FWHM}. The flat pulse for comparison is defined as:

$$f(t, p, W_{FWHM}) = \begin{cases} \dfrac{\sqrt{2\pi}w}{W_{FWHM}} & \text{if } |t-p| < W_{FWHM}/2, \\ 0 & \text{otherwise,} \end{cases} \tag{4.3}$$

where it has been normalised to the same fluence as the Gaussian pulse above. These two pulses are shown in Fig. 4.1. Note also that there is a hard cut-off at 170 fs for the Gaussian pulse[1].

The effect of the now more intense laser drive is to shift the evolution of the charge states further from LTE and they start to exist at higher temperatures than in the non-LTE Gaussian pulse case that was shown in Ch. 3.4. In Fig. 4.2 a few selected charge states from Fig. 3.10a are reproduced (in dotted lines) and compared with the simulation driven with a flat laser pulse (solid lines). Of course, nothing happens for the first 50 fs, but then once the laser switches on the effect is marked for the lower charge states. These are burnt through rapidly by the photoionization/Auger chain shown earlier in Eqn. 3.2; since the photoionization rate is higher each charge state starts to appear at higher temperatures than the Gaussian profile which was close to LTE. As an example, consider the curve for carbon-like Mg (labelled as 6^+ in Fig. 4.2). SCFLY calculates the peak photoionization rate when this charge state is most abundant as $4.8 \times 10^{13}\,\mathrm{s}^{-1}$. For the flat pulse this occurs around 60 fs – so around 10 fs after the laser switches on. Comparing this with the equivalent Gaussian drive, the rate is only $2.5 \times 10^{13}\,\mathrm{s}^{-1}$ and peaks around 50 fs. As expected, this rate is half the rate for the flat pulse, reflecting the fact that it occurs when the Gaussian drive is at half its maximum value. But importantly, this means that the burn for the Gaussian drive is slower and takes 5 times longer to reach the carbon-like ionization

[1]The astute reader will notice that the fluence is the same assuming there is no cut-off in the Gaussian pulse. The cut-off gives a reduction in fluence of $< 4\%$. Introducing this cut-off has a negligible effect on the final time and space integrated spectrum.

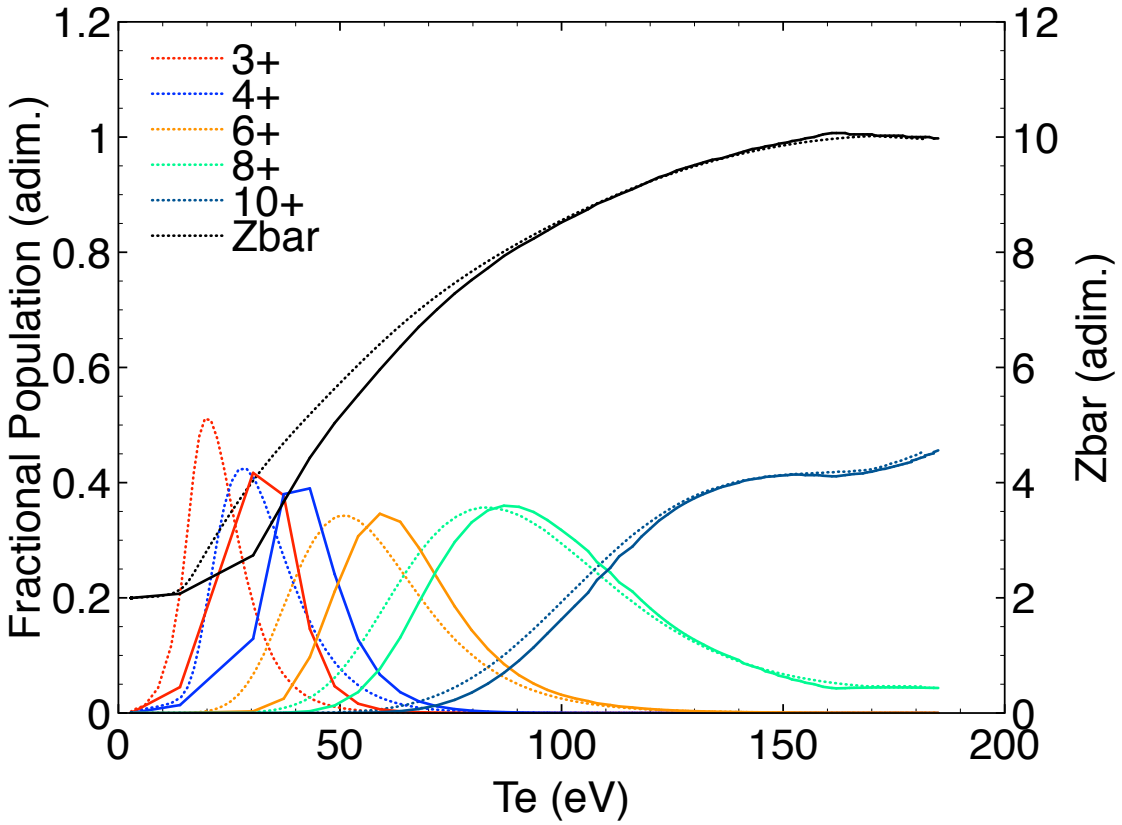

Figure 4.2: Charge state distribution, and mean charge state $\overline{z}$ (Zbar) evolution as a function of electron temperature for selected ionization stages at peak laser intensity for the case where the sample is driven by a Gaussian profile (dotted lines), and a flat profile (solid lines).

stage, and correspondingly, this stage peaks at a temperature that is 10 eV lower.

For readability only a few charge states are shown, but the trend is that as the pulse progresses in time and the system is driven to higher temperatures, the deviation from the Gaussian case becomes smaller. Above 100 eV the mean charge state evolution track is essentially the same between the two different laser drives. Here the mean charge state is higher and the heating is limited by the longer KL radiative recombination rates of the higher charge states as the rapid Auger decay channel is no longer open. The tracks end at the same final (long time) $\overline{z}$ and T_e as expected because the two pulses have the same fluence: after enough time the system approaches the same steady-state solution. Furthermore, and most relevant to the final emission

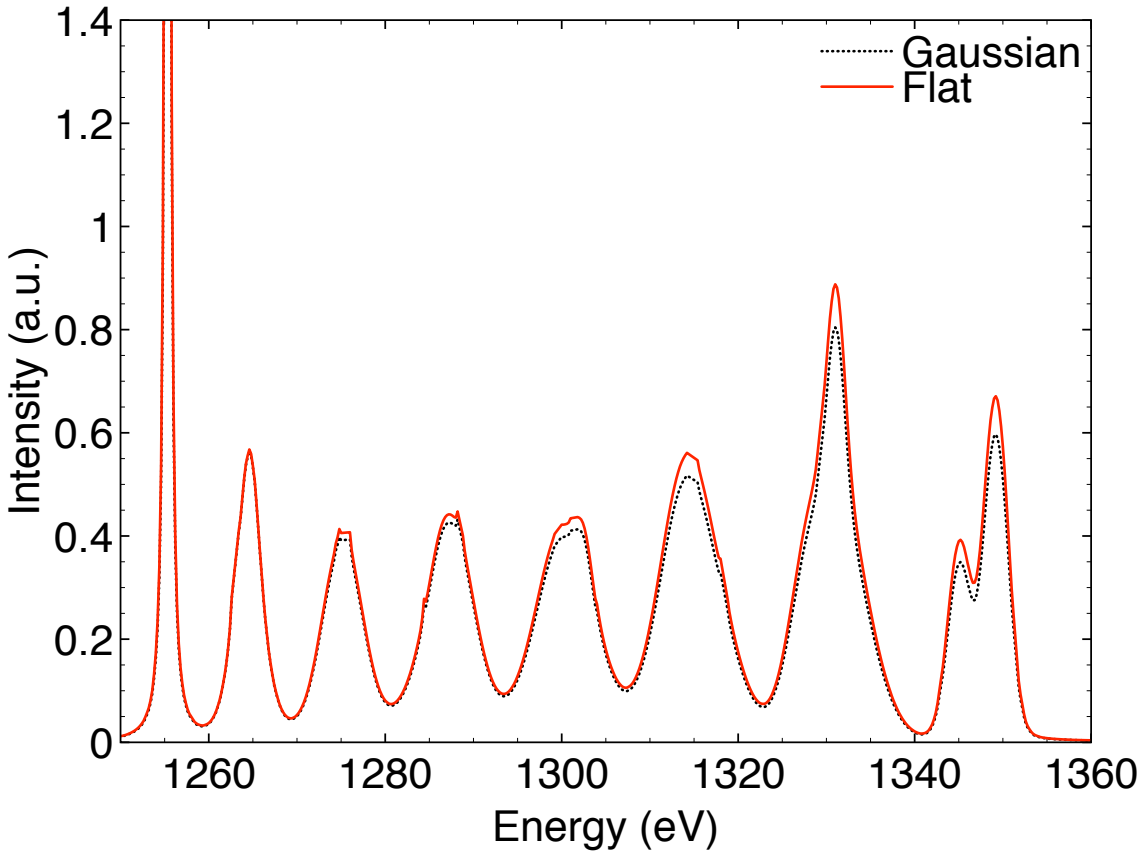

Figure 4.3: The prediction of space- and time-integrated 0D SCFLY simulations with thickness 54nm for the case where the sample is driven by a Gaussian profile with FWHM of 100 fs (black dotted), and a flat profile with the same parameters (red solid).

spectrum, the ground state populations peak at a lower value than in the Gaussian case. This is because the photoionization rate is larger for the entire pulse – the upper states responsible for the emission have larger populations.

The effect this has on the calculated emission spectrum ends up being subtle as evinced in Fig. 4.3. The overarching shape of the spectrum is the same, but the emission for higher charge states is larger by about 10% since the photoionization rate is higher. This emission excess increases moderately as the charge state increases from around 6% to approximately 12% for the He-α line. Whether this would be detectable in an experiment is unlikely as the expected increase on every line is within the experimental error of the emission spectra shown in Ch. 3. Consequently, the final

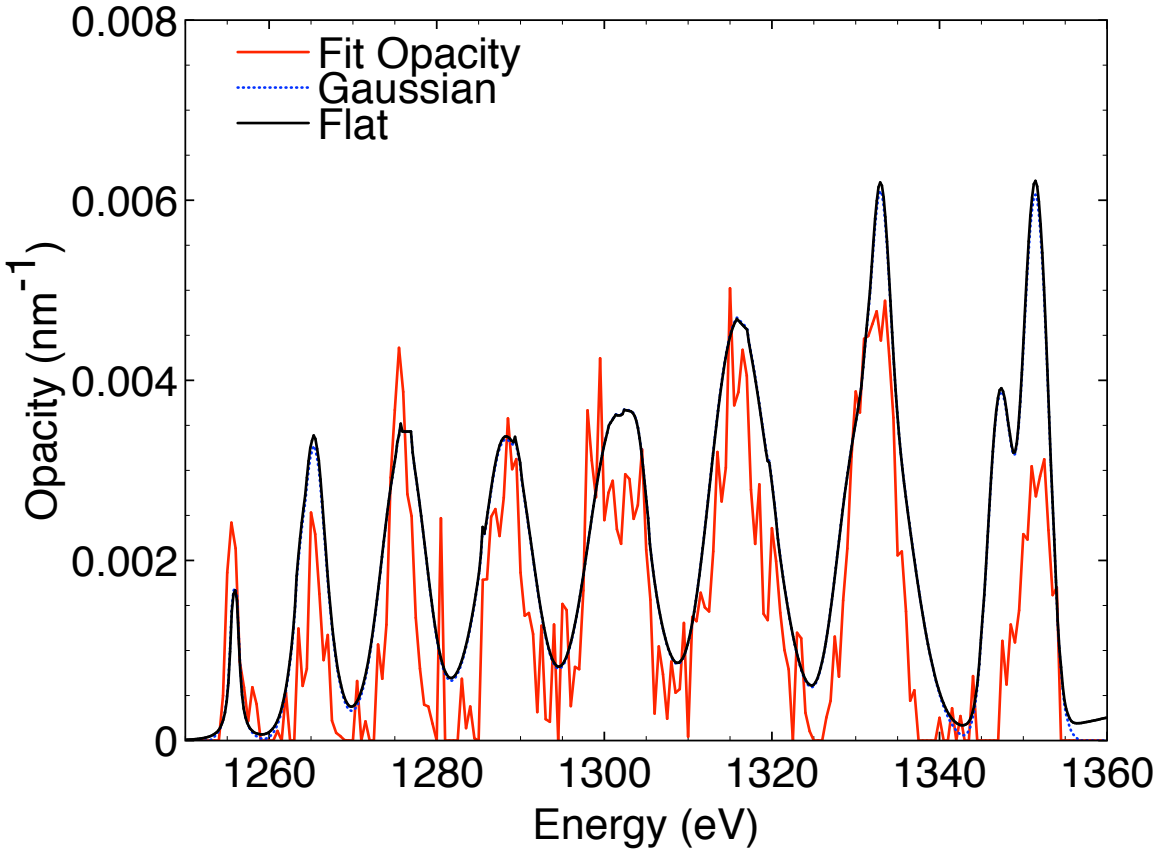

Figure 4.4: A comparison of the fitted experimental opacity $\kappa(\nu)$ with the integrated opacity derived from fitting Eqn. 3.8 to simulated SCFLY spectra for a Gaussian profile with FWHM of 100 fs (blue dotted), and a flat profile with the same parameters (black solid).

emission spectrum is robust against a change in pulse-shape.

Coincidentally, the effect on the deduced opacity from fitting using the procedure of Ch. 3.4.1 is negligible as shown in Fig. 4.4 where the curves for the nominal 100 fs Gaussian pulse and the flat pulse nearly completely overlap. Despite the flat pulse increasing the emission of the Li-like and He-like lines, this does not result in an appreciably larger value for the integrated opacity.

4.1.2 Pulse length

Similarly, relaxing the assumption that the pulse has a FWHM of 100 fs is investigated. Here, five different pulses are considered: three are realistic – the nominal

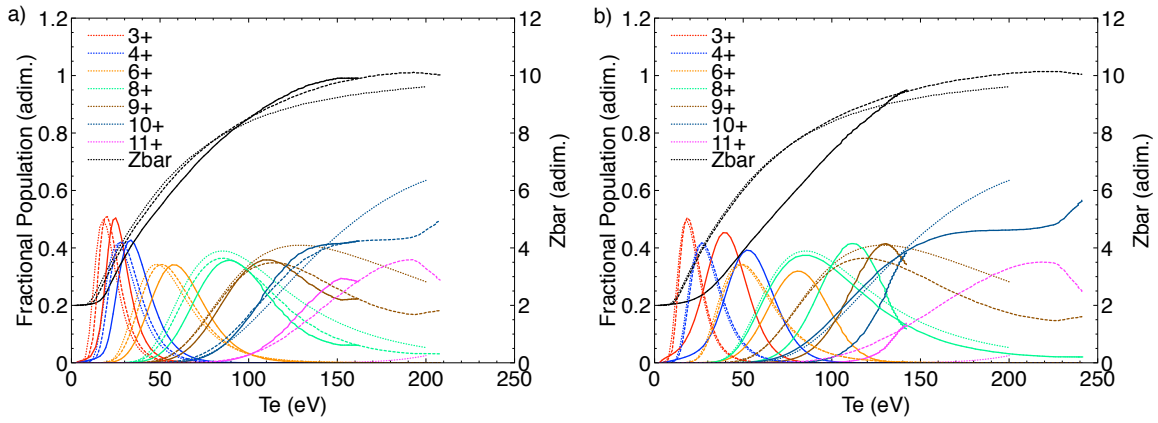

Figure 4.5: Charge state distribution, and mean charge state $\overline{z}$ (Zbar) evolution as function of electron temperature for selected ionization stages at peak laser intensity for the case where the system exists in LTE (dotted curve both figures); the sample is driven by a shorter Gaussian profile (solid lines) with FWHM of a) 50 fs, b) 10 fs; and, a longer Gaussian profile (dashed lines) with FWHM of a) 200 fs, b) 500 fs. The longer profiles are closer to LTE for most of the charge state evolution, whereas the shorter profiles are driven more strongly and show larger departures from the LTE solution.

pulse, and a halving or doubling of the pulse length to 50 or 200 fs; the other two less so but are illustrative – an ultrashort pulse of 10 fs, and a very long one at 500 fs. As in the previous section the X-ray fluence is conserved.

Again, using a higher intensity drive (as is required for the shorter pulse length) leads to a larger departure from LTE. Shown in Fig. 4.5a is the population evolution for the 50 fs and 200 fs drives, and in Fig. 4.5b the more extreme cases of 10 fs and 500 fs pulses both compared with the LTE case that was shown previously in Fig. 3.10b. The longer the laser pulse the more similar to LTE the evolution is for most of the laser drive. The difference for the ultrashort pulse in Fig. 3.10b is stark. Because of this five-fold increase in laser intensity, the 3^+ peaks at a much higher temperature of 40 eV and the system's overall evolution is truncated to below 150 eV. The reason for this is the competition between the very short laser drive and comparably short Auger rate: the Auger rate is not fast enough to move up through the charge state distribution before the end of the laser pulse.

Whilst the longer profiles are even closer to LTE, at higher temperatures above 100 eV (and correspondingly later in the drive), the mean charge state exceeds that for the LTE case because of the far higher population of hydrogenic ions (shown in magenta in Fig. 4.5). Recall, as discussed previously, that the radiative lifetime of the Li-like ion is long and if this ion stage exists for an appreciably long time during the laser drive it can be doubly-ionized to the upper state (K^0L^1) of the hydrogenic ion. On the other hand, the He-like and Li-like ions contemporaneously exist in lower abundances, especially for the longer 500 fs pulse – these two effects combined give a higher mean charge state over the LTE calculation. Furthermore, if one wanted to ensure closer LTE conditions for most charge states, then a longer, lower intensity pulse should be chosen.

Unlike in the flat-top case discussed before, the final temperature and density (mean charge state) conditions obtained after the laser pulse ceases are not the same as the 100 fs Gaussian pulse, despite the same fluence being used in both cases. The reason for this is exactly the same as above. Using the ultrashort and very long pulse as extreme illustrative examples, the end mean charge state for the 10 fs pulse is 9.5 in the focal spot compared to 10 for the longer 500 fs pulse. The ultrashort pulse finishes before the highest charge states, burnt through via photoionization/Auger decays, can be arrived at, despite the increased rate of photoionization leading to an overall faster burn-through. Here, the limiting step is the approximately 5-10 fs Auger decay before an ion can absorb another LCLS photon[2]. Conversely for the long pulse, the early evolution is not similarly limited since the mean time between photoionizations is much longer than the Auger decay time and the progression up through charge states closely follows LTE. But as discussed above, the He-like ions with their comparably long radiative lifetimes now have sufficient time to be created in abundance and concurrently so does the excited hydrogenic ion stage. The result is

[2]The photoionization rate for the Be-like ion in the middle of the pulse is such that a photon is absorbed about once every 2 fs, and the excited state undergoes an Auger decay once every 10 fs.

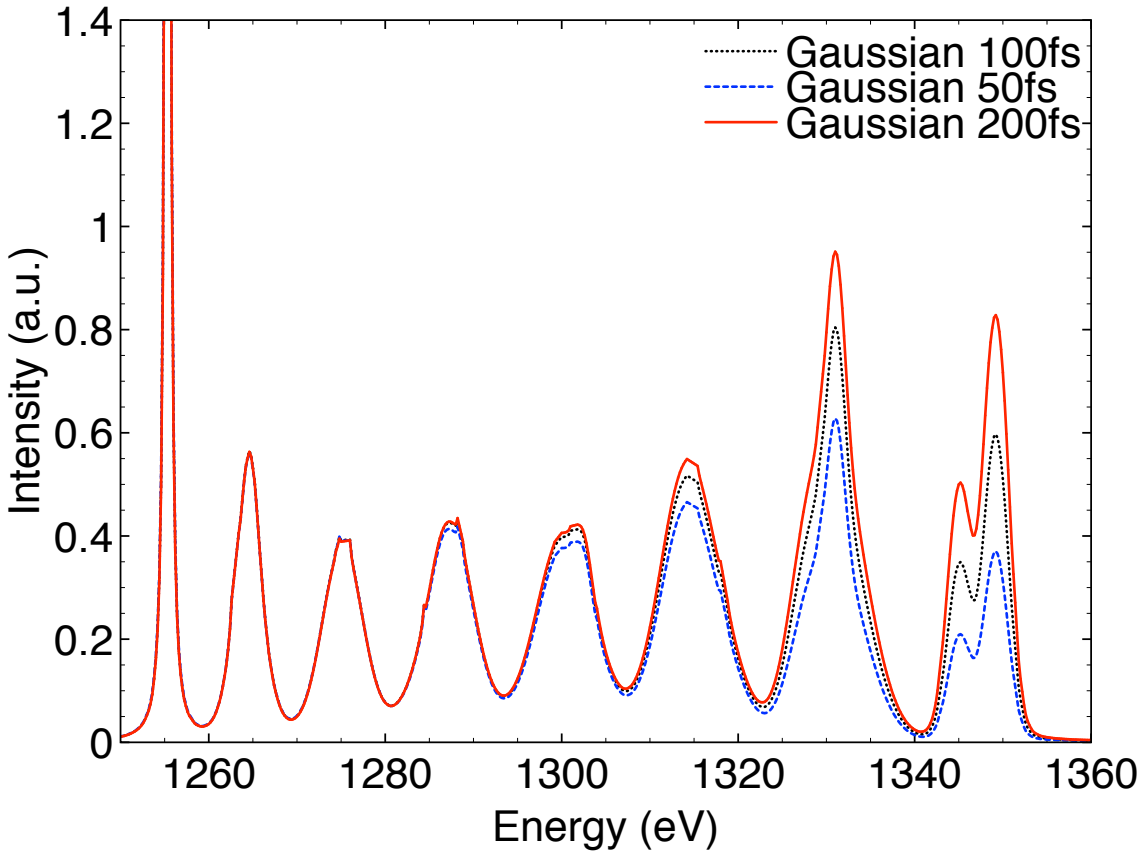

Figure 4.6: The prediction of space- and time-integrated 0D SCFLY simulations with thickness 54nm for the case where the sample is driven by a Gaussian profile with FWHM of 100 fs (black dotted), 50 fs (blue dashed), and 200 fs (red solid).

a higher temperature and density than the 100 fs Gaussian drive: by taking a longer time, the laser's deposition of energy is much more efficient.

Remarkably, the effect of changing pulse length by a factor of two is modest on the final emission spectrum and deduced opacity. To reiterate the above discussion, decreasing the pulse duration doesn't allow enough time (limited by the Auger rate) to burn through to the higher charge states – they appear under lower temperature conditions – and so the higher energy lines don't appear as strongly. However increasing the pulse length pushes the evolution more towards LTE and the lines emit for longer limited by their A-rate lifetime because the time between photoionizations for a lower intensity pulse is longer. As an extreme example of the ramifications of this, an equilibrium can be set up whereby a Li-like ground state can absorb an LCLS

photon to become the excited state K^1L^1, emit a He-α photon, and then collisionally recombine back to the Li-like ion numerous times whilst the laser is on. For the 500 fs pulse length, at maximum laser intensity, this can occur for more than 200 fs in the latter half of the drive. However, these differences are ironed out once the emission is time and space integrated over the focal spot.

Furthermore, this can actually be used as a limit on the pulse length. Given that the energy content of the LCLS pulse before the final focussing optics[3] (measured using a GMD) and its measured spatial gradients on target are more accurately known than its temporal characteristics (based on the electron bunch length), modifying the pulse length and comparing the shape of the resulting emission spectrum allows the pulse length to be constrained within $20-40$ fs since the effect on the intensity of the higher lying lines is stronger (indeed, more than in the flat profile discussed earlier). Overall it would appear that any pulse length within this limit may be chosen giving qualitatively the same results for most charge states; and furthermore, a better fit across the whole spectrum (including the highest lines) could be obtained with a shorter pulse.

The effect of this on the deduced opacity is again small as can be seen in Fig. 4.7 – compressing or stretching the pulse length by factor of two has no appreciable effect on the integrated opacity deduced by this method for all charge states up to Be-like. There is an increase in the probed opacity of the Li-like and He-like lines when using a longer pulse due to the increased time window over which these states may emit. However, using a longer pulse with the same fluence gives qualitatively the same behaviour but with a smaller population of upper states and would be beneficial as the laser is then a more perfect probe: the conditions of the ground states are closer to LTE, and the percentage pushed out of LTE through photoionization by the laser, at any given time is smaller. However, given that the measured opacity for the higher

[3]This will turn out to be important in Ch. 5.

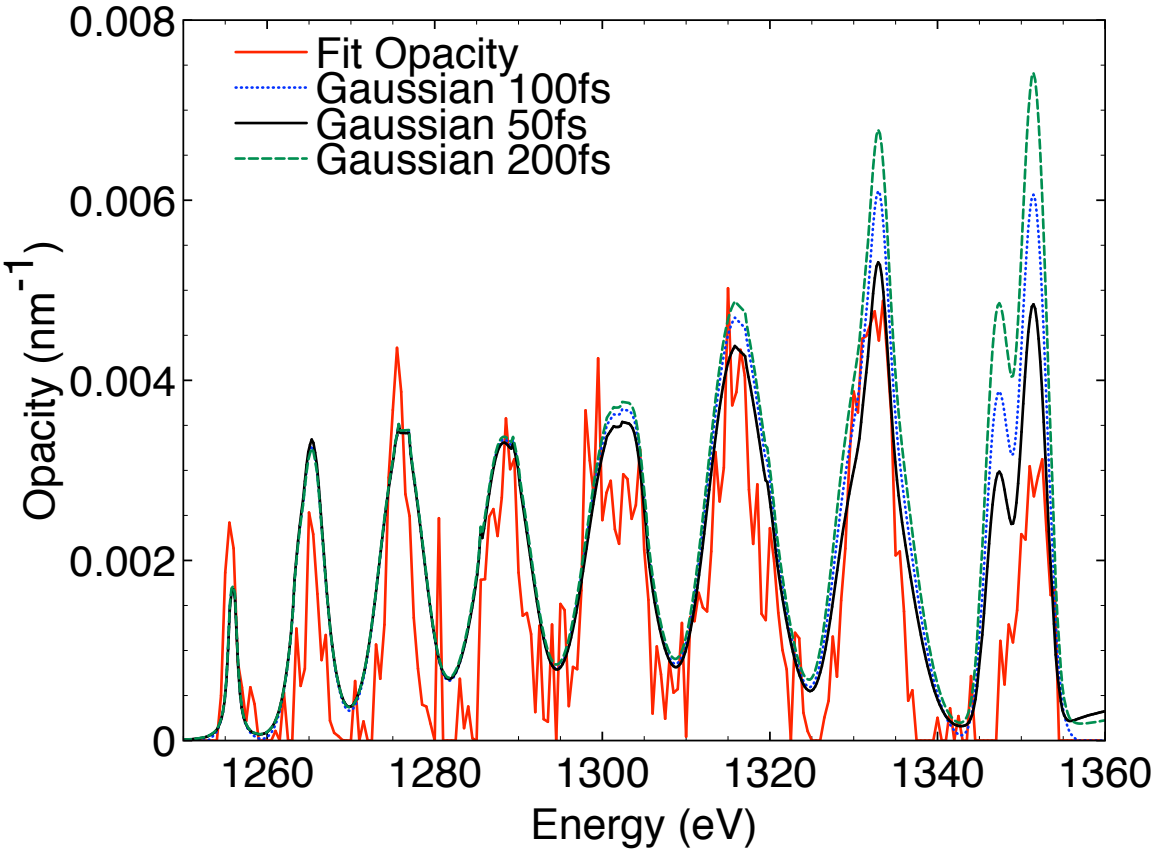

Figure 4.7: A comparison of the fitted experimental opacity $\kappa(\nu)$ with the integrated opacity derived from fitting Eqn. 3.8 to simulated SCFLY spectra for a Gaussian profile with FWHM of 100 fs (blue dotted), 50 fs (black solid), and 200 fs (green dashed).

lines is lower, what may be occurring is the pulse-length is in reality shorter than the modelled 100 fs.

4.1.3 X-ray fluence

Finally, modifying the X-ray energy in the pulse is investigated. The driving pulse's energy content is halved to 0.85 mJ, and doubled to 3.4 mJ, whilst keeping the pulse's temporal parameters fixed at their nominal value of 100 fs for the FWHM.

Expectedly, reducing the energy content of the pulse decreases the intensity of the emission lines, however the effect is more profound for the higher lines which come later in the pulse. Whereas just lengthening the pulse slows the evolution because of the reduced ionization rate with the spectra still exhibiting the same intensity for

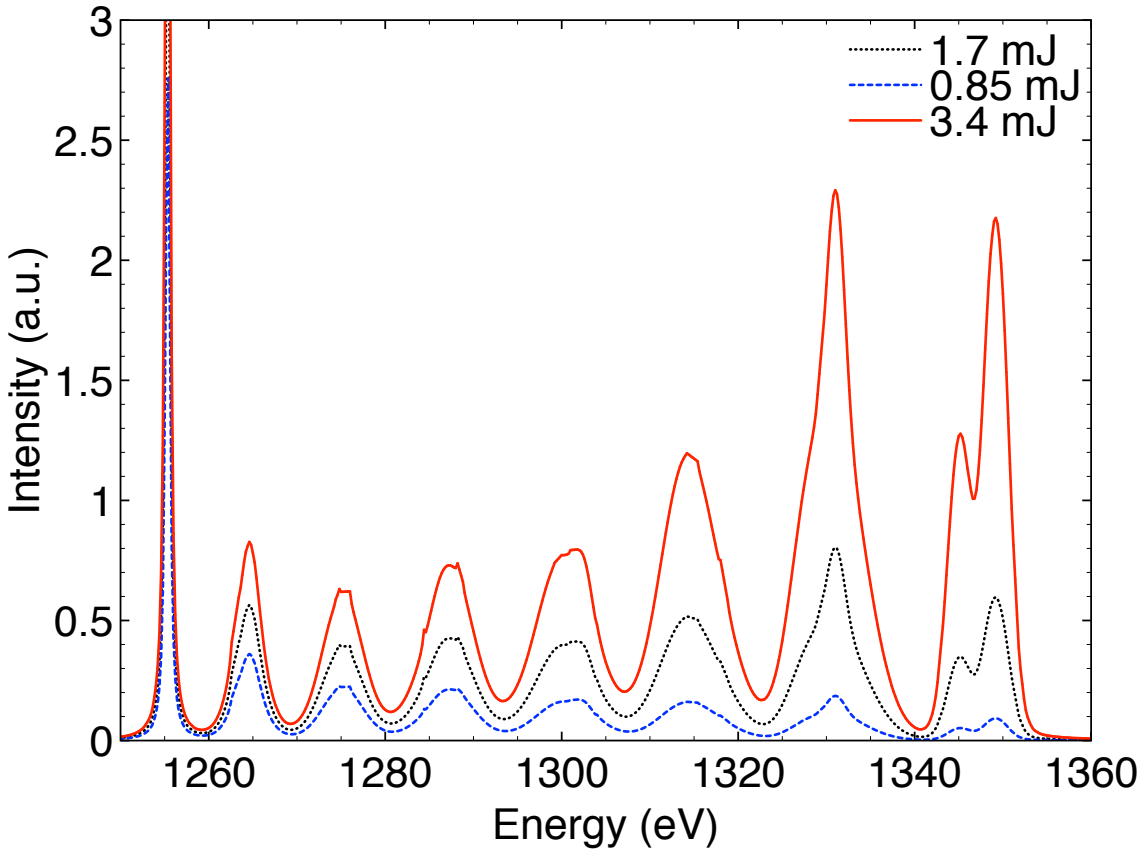

Figure 4.8: The prediction of space- and time-integrated 0D SCFLY simulations with thickness 54nm for the case where the sample is driven by a Gaussian profile with FWHM of 100 fs (black dotted) and nominal fluence of 1.7 mJ, the same temporal profile but with the fluence halved to 0.85 mJ (blue dashed), and doubled to 3.4 mJ (red solid).

most lines as the available number of photons for photoionization remains the same – now they are reduced. Instead, reducing the overall fluence not only decreases the availability of these upper states dramatically (and therefore their emissivity) but also truncates the evolution to end at a lower temperature. There is consequently a marked drop off in line emission as a function of frequency as seen in Fig. 4.8 mirroring the reduced populations of upper states. For example, in Fig. 3.12 using a 1.7 mJ fluence the population of K^1L^1 peaked around $11 \times 10^{21}\,\mathrm{cm}^{-3}$, higher in fact than the ground state; but in the lower fluence scenario, this population peaks at half this value, with a population of $6 \times 10^{21}\,\mathrm{cm}^{-3}$, and later in the laser pulse. The emissivity of all charge states is thus reduced, and more dramatically for the later charge states.

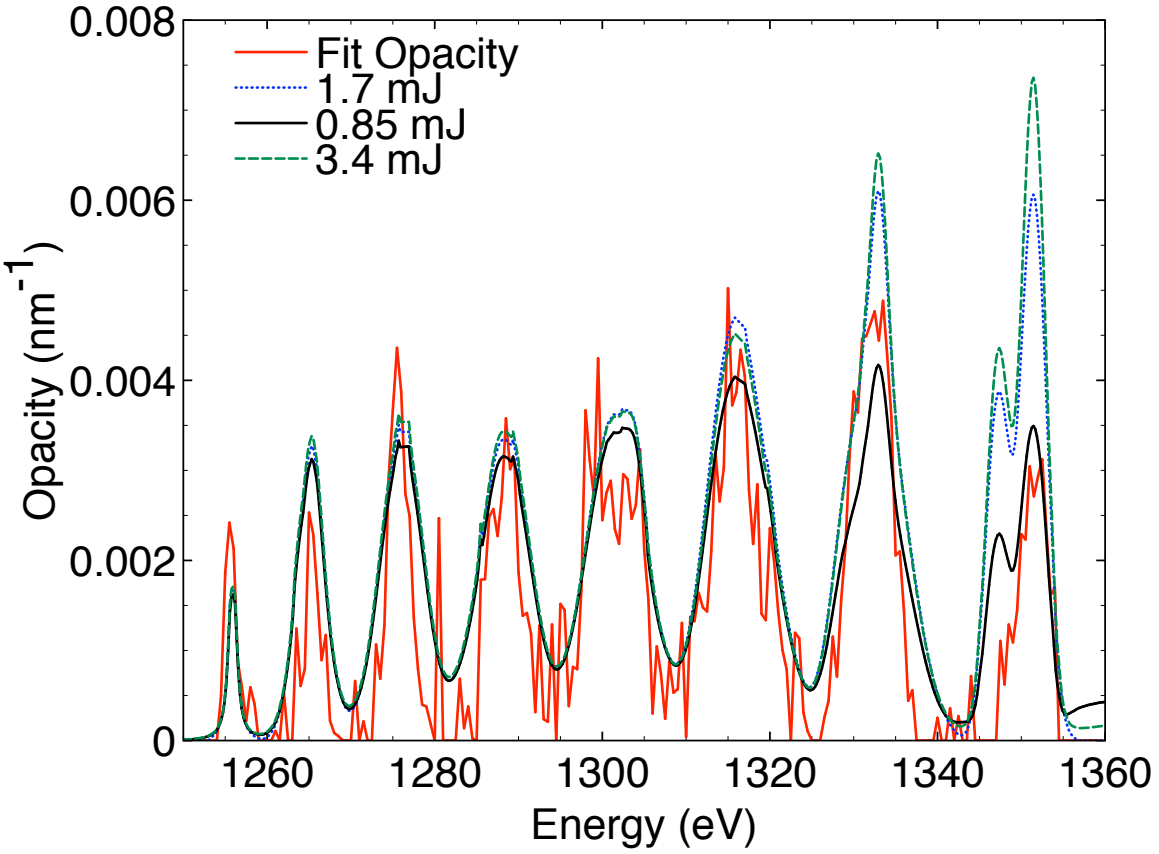

Figure 4.9: A comparison of the fitted experimental opacity $\kappa(\nu)$ with the integrated opacity derived from fitting Eqn. 3.8 to simulated SCFLY spectra for a 1.7 mJ nominal drive (blue dotted), the fluence reduced to 0.85 mJ (black solid), and increased to 3.4 mJ (green dashed).

On the other hand, doubling the fluence increases the line emission as a function of frequency and similarly has the largest effect on the He-α line. Doubling or halving the fluence roughly has the same effect of doubling or halving the line intensity of most lines.

This can go some way to explaining an anomaly in Fig. 3.5 where a lower than expected intensity is observed for the He-α line of the thinnest target. This line originates almost exclusively from the hot core of the focal spot in a region of diameter ~ 100 nm, where the temperature peaks at 180 eV. If, for example, the final temperature attained were to be lower for the thinner target then this would explain the deficit in the He-α line. A reason for this could be losses of Auger electrons from the

target. These have already been shown in previous work to thermalise rapidly (within a few fs) preventing the creation of a two-temperature distribution [47]. However, a 1300 eV electron travels at a velocity of $21\,\mathrm{nm\,fs^{-1}}$ and could conceivably escape the target altogether before it has an opportunity to thermalise with the free electron distribution through collisions with ions, on average in less than 2 fs [53]. This is discussed further in Ch. 6.

Somewhat surprisingly, despite this drop (or increase) in line emission overall, the effect on the opacity is not appreciable. This makes sense if, as a rough guide, one assumes that a doubling in fluence (number of photons available for photoionization) leads to a doubling in line emission (number of photons re-emitted from K-L recombination) for every target. Without absolute values for the number of photons emitted it is difficult to disentangle the effect on the extracted opacity of, say, an decrease in pulse length versus an decrease in fluence. It was found in Ch. 3.4.1 that the deduced opacities match SCFLY simulations well for all lines except the lithium-like and helium-like lines where the deduced opacity is lower than expected. This may therefore be attributed to a lower final temperature than expected from SCFLY simulations affecting only these higher charge states. The reason for this is because these states are only populated at the end of the pulse, and now in lower quantities than for the nominal drive. The rest of the evolution however remains the same, indicative of the fact that provided one burns through the charge states in a roughly linear fashion and with enough time that they exist in near-LTE conditions, the deduced opacity for most charge states is consistent regardless of fluence, pulse length, or pulse shape. The important point here is that the lower opacity for the final two lines could be either due to a shorter pulse length, or lower pulse energy. More information is required to discern between the two and this will be elaborated on in Ch. 5.

4.2 Assumptions of the fit to Radiation Transfer

In this section the intrinsic assumptions of the fit to the 1D solution to the equation of radiative transfer are investigated. Formally, the 1D solution is:

$$\overline{I}(\nu, d, \theta) = \int_{t=0}^{t_f} \int_{z=0}^{d} \eta(\nu, z, t) \exp(-\kappa(\nu, z, t)\, z/\cos(\theta))\; dt\; dz, \tag{4.4}$$

where the emissivity and opacity may be functions of both position along the line-of-sight and functions of time t. The z-coordinate is integrated from the back to the front of the target and the t-coordinate runs until some final t_f later than the emission peak. Firstly, the assumption that the time-integrated form of this equation has the same functional shape as Eqn. 3.7 is formally investigated. Then, in the succeeding section, the effect of linear modifications to the emissivity and opacity is considered in detail in the time-independent (instantaneous) case.

4.2.1 Time-integration of the intensity

The effect of the rise and fall of the emissivity and opacity on the functional form of the radiation transfer solution is investigated. The value of $\sim 40\%$ found earlier for the ratio of the measured opacity to the maximum instantaneous opacity is justified and the assumption of Eqn. 3.8 is found to be excellent. Eqn. 4.4 is integrated along the line-of-sight assuming that $\eta(\nu, t)$ and $\kappa(\nu, t)$ are not functions of distance $d_S = d/\cos(\theta_S)$, where $\theta_S = 20°$. It is assumed that the line-centre is observed and so the explicit dependence on frequency is dropped. The solution to the 1D problem is then:

$$\overline{I} = \int_{0}^{t_f} \frac{\eta(t)}{\kappa(t)} [1 - \exp(-\kappa(t)\, d_S)]\; dt, \tag{4.5}$$

for one specific line only. For non-linear functions of $\eta(t)$ and $\kappa(t)$ this is difficult to solve analytically. As a simple example, Eqn. 4.5 is solved for $\kappa(t) = \kappa_0\, g(t, p, w)$,

where $g(t, p, w)$ is the Gaussian defined in Eqn. 4.2. The parameters are taken to roughly match those shown in Fig. 3.13 for the boron-like ion stage: that is a peak at $p \approx 60\,\text{fs}$, and $W_{FWHM} = 30\,\text{fs}$. In reality the profile is asymmetrically skewed with a steeper rise than fall due to the exponential processes that populate and de-populate levels, found from solving the rate-equations. The maximum opacity is chosen to be $\kappa_0 = 0.008\,\text{nm}^{-1}$ matching that in Fig. 3.8 for line VII. To simplify the analysis, the FWHM of the emissivity curve is assumed to be the same, and its peak is taken to be δp later at $p_\eta = p + \delta p$ with the same height κ_0, such that the source function $|S| = 1$. Therefore, $\eta(t) = |\kappa_0|\, g(t, p + \delta p, w)$.

Eqn. 4.5 is therefore solved numerically:

$$\overline{I} = \int_0^{t_f} \frac{g(t, p + \delta p, w)}{g(t, p, w)} [1 - \exp(-\kappa_0\, g(t, p, w)\, d_S)]\; dt, \tag{4.6}$$

as a function of thickness d_S for different offsets of $\delta p = 0,\ 2,\ 10,\ 20\,\text{fs}$. The results are shown in Fig. 4.10a; due to the symmetry of the Gaussian function, there is no appreciable difference between using positive or negative differences in the peak position.

To analyse the departure from the simple time-averaged solution of Eqn. 3.8, the curves in Fig. 4.10a are fitted using the procedure described in Ch. 3.3. The fractional deviation ΔI of the time-integrated curve from the simple 1D solution of Eqn. 3.8 is defined as,

$$\Delta I = \overline{I} - \frac{\eta_f}{\kappa_f} [1 - \exp(-\kappa_f\, d_S)], \tag{4.7}$$

where $\overline{I}$ is defined in Eqn. 4.6 and, η_f and κ_f are found from fitting to the form of Eqn. 3.8 at the same thicknesses as the experimental data, as described in Ch. 3.3. The fitted values of the opacity are $0.0045\,\text{nm}^{-1}$ for both $\delta p = 0$ and 2 fs: ergo, there is no appreciable difference in the fitted opacity for a small temporal shift. The opacity decreases to $0.0035\,\text{nm}^{-1}$ for $\delta p = 10\,\text{fs}$, and to $0.0019\,\text{nm}^{-1}$ for $\delta p = 20\,\text{fs}$. The effect

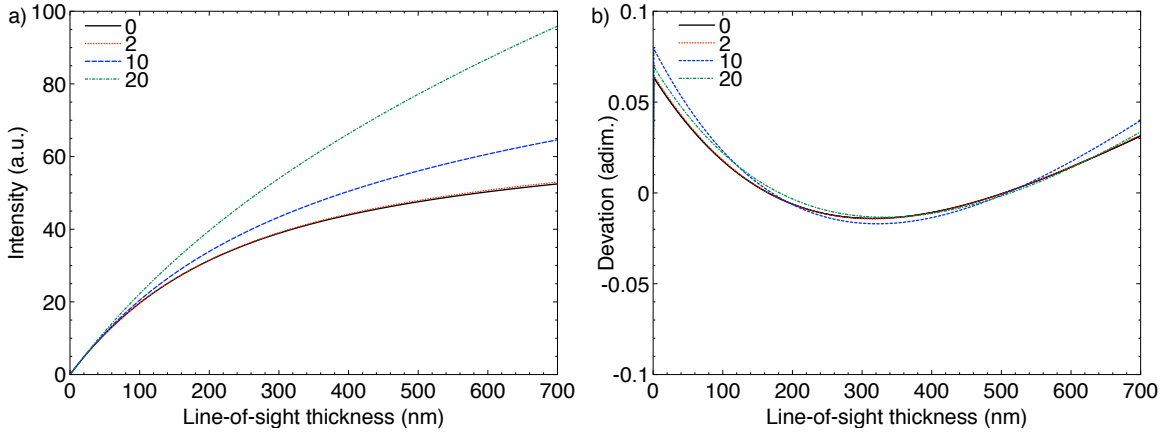

Figure 4.10: Examples of the effect of different offsets in the peak time between η and κ on the functional form of the radiative transfer solution, using $\kappa_0 = 0.008\,\mathrm{nm}^{-1}$. The offsets are $\delta p = 0,\ 2,\ 10,\ 20\,\mathrm{fs}$. Shown in a) is the time integrated radiative transfer solution, and in b) the deviation (Eqn. 4.7) from the functional form of the simple 1D slab solution to radiative transfer of Eqn. 3.8 used to fit the data in Ch. 3.3.

of increasing the time delay between the peaks is to decrease the overlap between the curves, allowing the emission to depart through a region with a contemporaneously lower opacity – this results in a smaller extracted opacity. Using a difference of $\delta p = 2\,\mathrm{fs}$, which matches the emissivity and opacity of Fig. 3.13, has a less than 1% effect on the derived opacity, so provided the emissivity peaks with the opacity then the temporal profile of the opacity is accurately probed. Furthermore, the deviation from the simple time-averaged form of Eqn. 3.8 is found to be $< 5\%$ as evinced by Fig. 4.10b and mimics the shape of the data (albeit to a lesser degree): the intensity points are larger than the fit for the two thinnest and thickest targets, but less than the fit for the third target around one optical depth as evinced in Fig. 3.6.

In Fig. 4.10 the approximation of Eqn. 3.8 is confirmed to be excellent and essentially one may therefore assume the functional form of the 1D solution to radiative transfer may be applied to time-integrated spectra with time-averaged parameters. Furthermore, the extracted opacity here is between 24% for a large temporal shift and 56% for a small temporal shift, in rough agreement with the ratios shown in Fig. 3.8. Larger shifts give a lower extracted opacity as the probed emissivity passes

through a region of relatively lower opacity, and this corresponds well with the He-α line where the rise and fall of the emissivity is neither exactly contemporaneous with the opacity, nor is the opacity well approximated by the Gaussians discussed here. Another point to note is that the extracted opacity as a percentage of the maximum instantaneous opacity (set above to be $\kappa_0 = 0.008\,\mathrm{nm}^{-1}$) is slightly higher than the measured value $\sim 40\%$, most probably because the actual evolution of the charge states is exponential and determined by the solution to the rate equations. However, this simple model captures much of the physics of what's going on.

Whilst the absolute value of the temporal shift δp is important, it of course also depends on the length of the driving laser pulse as described in Ch. 4.1.2. As expected, for longer pulses the difference between the time of peak emissivity and peak opacity also increases commensurately, however, the ratio of δp to W_{FWHM} is roughly constant at 6% regardless of the pulse length. This again most likely reflects the fundamental processes that populate the upper state and lower state, and indeed one would expect these processes to modify the time delay between the emissivity and opacity peaking in a similar way to their lifetimes (FWHM) such that their ratio is constant.

Further, the effect of squeezing or stretching the Gaussian was also investigated. The values of $W_{FWHM} = 10$, 30, and 50 fs are chosen setting both widths of the emissivity and opacity Gaussians to be the same, and $\delta p = 0\,\mathrm{fs}$. This has the effect of increasing the integrated intensity, as correspondingly the integral in Eqn. 4.5 is larger, but this has no effect on the derived opacity – renormalising the curves to incorporate this into the source function removes this effect.

The reason that adjusting the width has no effect when $\delta p = 0\,\mathrm{fs}$, can be seen by solving Eqn. 4.5 analytically using the series expansion of the exponential:

$$\overline{I} = -\int_0^{t_f} \sum_{n=1}^{\infty} \frac{(-\kappa_0\, g(t,p,w)\, d_S)^n}{n!}\, dt = -\sum_{n=1}^{\infty} \frac{(-\kappa_0\, d_S)^n}{n!} \int_0^{t_f} g^n(t,p,w)\, dt. \quad (4.8)$$

The solution to this is much simpler as the source function is no longer a function of time. Integrating over the Gaussian assuming $t_f \to \infty$ gives,

$$\overline{I} = -\sqrt{2\pi} w \sum_{n=1}^{\infty} \frac{(-\kappa_0 \, d_S)^n}{n! \sqrt{n}}. \tag{4.9}$$

The Gaussian width w is just a constant scaling factor here and may be absorbed into the source function. Note that this looks very similar to the case with no Gaussian integration apart from the annoying factor of $\sqrt{n}$. Incorporating this into the bracket containing the optical depth modifies the optical depth by a factor of $n^{-1/2n}$ which remarkably, for small $1 < n < 10$, is around 0.85 but moreover increases tending monotonically towards 1 as $n \to \infty$. Therefore, Eqn. 4.9 sort of looks like the expected $[1 - \exp(-\kappa_0 d_S)]$ form except with the lower order terms slightly modified. Finally, this result may be arrived at more quickly by considering that the plasmas modelled in this thesis are optically thin and generally have $\kappa_0 d_S \ll 1$. Thus Eqn. 4.9 reduces to $\sqrt{2\pi} w \kappa_0 d_S$ exactly in the optically thin limit – yielding the same optically-thin limit as with no temporal considerations encountered in Ch. 3 but with the source function increased by a factor of $\sqrt{2\pi} w$.

4.2.2 Linear variations in the emissivity and opacity

The effect of linear variations in the emissivity and opacity are investigated here. These would arise if there were some mechanism whereby the emissivity or opacity were to increase or decrease as photons transit out of the target. For example, if the number of emitting or absorbing atoms were to change along the line-of-sight, possibly as a result of the radiation field in the plasma. This is considered in the time-independent case and the starting point is the integral form of the solution to

the equation of radiative transfer:

$$I(\nu, d) = \int_0^d \eta(\nu, z) \exp(-\kappa(\nu, z)\, z)\; dz, \tag{4.10}$$

where the integral runs over the z-coordinate from the back to the front of the target, and the explicit time and angle dependence[4] has been dropped. Of course in the simple case that $\eta(\nu, z)$ and $\kappa(\nu, z)$ are not functions of distance the result shown in Eqn. 3.7 is recovered. It is assumed in the following that $\eta(z) = \eta_0 + \eta_1\, z$, and $\kappa(z) = \kappa_0 + \kappa_1\, z$ where the dependence on frequency has also been dropped.

Firstly, Eqn. 4.10 is integrated assuming that the emissivity is a function of distance. The integral to be calculated is:

$$I_\eta(d) = \int_0^d (\eta_0 + \eta_1\, z)\; \exp(-\kappa_0\, z)\; dz. \tag{4.11}$$

The first term with η_0 gives the expected behaviour of Eqn. 3.7, which is rewritten in this notation as:

$$I_0(d) = \frac{\eta_0}{\kappa_0}[1 - \exp(-\kappa_0\, d)]. \tag{4.12}$$

The second term may be integrated by parts:

$$I_\eta(d) - I_0(d) = \eta_1 \int_0^d z\; \exp(-\kappa_0\, z)\; dz, \tag{4.13}$$

to give the final expression:

$$I_\eta(d) - I_0(d) = \frac{\eta_1}{\kappa_0^2}[1 - \exp(-\kappa_0\, d)] - \frac{\eta_1\, d}{\kappa_0}\, \exp(-\kappa_0\, d). \tag{4.14}$$

In the limit of $\eta_1 \to 0$ then the right-hand side becomes zero and the equation reduces to the simple solution.

[4]Note that if θ were included then the analysis would be same except there would be a constant $\cos(\theta)$ term.

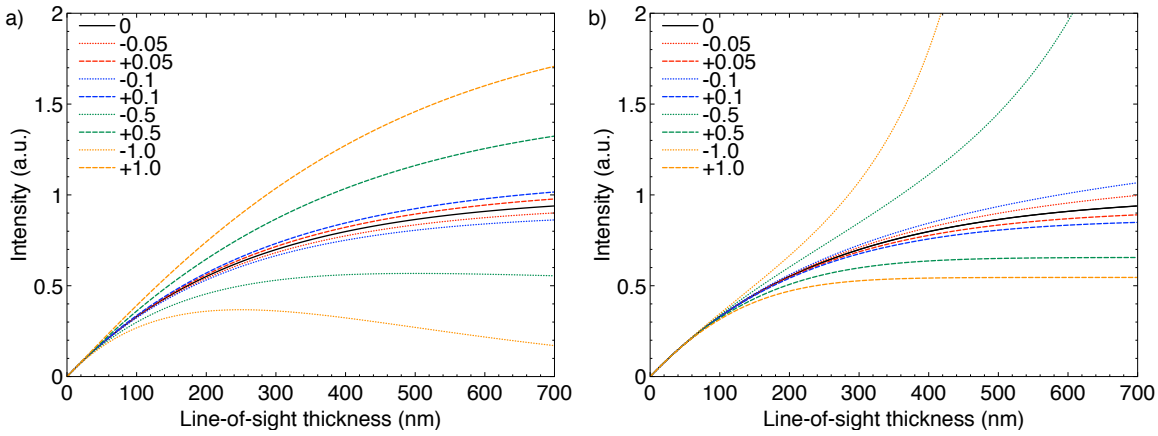

Figure 4.11: Examples of the effect of linear variations in η and κ on the functional form of the radiative transfer solution, using $\kappa_0 = 0.004\,\text{nm}$ and η_0 set such that the optically-thick limit (source function) $\eta_0/\kappa_0 = 1$: a) the effect of perturbations in $\eta_1 d_\tau/\eta_0 = \pm 0.05, \pm 0.1, \pm 0.5, \pm 1.0$; and b) the effect of perturbations in $\kappa_1 d_\tau/\kappa_0 = \pm 0.05, \pm 0.1, \pm 0.5, \pm 1.0$.

The functional form of the modulation created by these extra terms is shown in Fig. 4.11a for the case that $\eta_1\, d_\tau/\eta_0 = \pm 0.05, \pm 0.1, \pm 0.5, \pm 1.0$, where $d_\tau = 250\,\text{nm}$ – the thickness at one optical depth. The effect of a positive linear change in the emissivity is to increase the number of emitters with distance travelled along the line-of-sight distance. This would be the case in a lasing gain medium, or relevant to this work, if the number of ions with a core hole (upper states) was larger on the front surface of the target than the back surface. Whilst this would be much more pronounced for thicker targets, the effect would be very slight for the targets considered here. For example, the laser has an absorption depth of order microns [79] and for the thickest target ($d_4/\cos(\theta_F) = 689\,\text{nm}$) the transmission of the laser through the (cold) target is of order 65%. Assuming the number of emitters is proportional to the laser intensity, which isn't unreasonable as it is the laser which creates the core holes, would give a change of emissivity of $\eta_1 d_4/\eta_0 \cos(\theta_F) = 0.35$, similar to $\eta_1 d_\tau/\eta_0 = 0.13$ shown in Fig. 4.11a, and yielding a small increase for the thickest target. This effect is investigated in more detail in Ch. 5 and will differ from the simple model here because in reality the variation would be exponential not linear as the size increases,

and the transmission of the target will increase throughout the driving pulse as it becomes further ionized. However, for small differences this may be approximated as linear.

A negative linear change decreases the emissivity as a function of distance, and in the case of $\eta_1 d_\tau \to \eta_0$ allows the total emissivity to become negative for distances above this threshold. One should take care to discount values where this occurs – e.g. above 250 nm in Fig. 4.11a for the curve $\eta_1 d_\tau / \eta_0 = -1.0$ where the emission intensity begins to decrease unphysically for distances above this point. However, in general a negative linear change would be expected if one considers the effect of radiation trapping or self-absorption on the system assuming the number of absorbers is fixed.

The way that self-absorption is modelled in practice is by incorporating escape factors. The A-rate used to calculate the upper-state population n_u in Eqn. 2.7 is reduced, thus reducing the emissivity. If this were to vary from one point in the plasma to another along the line of sight, then one would have an emissivity varying as $\eta(z) = \eta_0 \pm \eta_1 z$. However, the escape factors calculated by SCFLY using Phillips et al. [52] are close to one, and so are neglected in this thesis.

Using this fit to the data with the extra parameter of η_1 gives the same fit as before with $\eta_1 \approx 0$. At frequencies where the fitting procedure does not find this, the values for η_1 chosen by the program are large indicating a failing of the fitting procedure due to noise rather than some real physical meaning. The extracted emissivity from the data therefore does not appreciably change with thickness.

Next, the alternative case that the opacity is a function of distance is integrated. It is useful to first define the error function:

$$\mathrm{erf}(x) = \frac{2}{\sqrt{\pi}} \int_0^x \exp\bigl(-t^2\bigr) dt. \tag{4.15}$$

The integral to be found is

$$I_\kappa(d) = \eta_0 \int_0^d \exp(-\kappa_0\, z)\ \exp\bigl(-\kappa_1\, z^2\bigr)\ dz. \tag{4.16}$$

Re-expressing the exponent as $\kappa_1 z^2 + \kappa_0 z = \kappa_1[z^2 + \kappa_0 z/\kappa_1]$, and then recasting by completing the square:

$$\kappa_1\Bigl[z^2 + \frac{\kappa_0}{\kappa_1} z\Bigr] = \kappa_1\Bigl[\Bigl(z + \frac{\kappa_0}{2\kappa_1}\Bigr)^2 - \Bigl(\frac{\kappa_0}{2\kappa_1}\Bigr)^2\Bigr], \tag{4.17}$$

the integral becomes:

$$I_\kappa(d) = \eta_0 \exp\bigl(\kappa_0^2/4\kappa_1\bigr) \int_0^d \exp\bigl(-\kappa_1\,(z + \kappa_0/2\kappa_1)^2\bigr)\ dz, \tag{4.18}$$

which can be solved by making the substitution $u = \sqrt{\kappa_1}(z + \kappa_0/2\kappa_1)$. The limits are $u_d = \sqrt{\kappa_1}(d + \kappa_0/2\kappa_1)$, and $u_0 = \kappa_0/2\sqrt{\kappa_1}$ and the final integral is found:

$$I_\kappa(d) = \frac{\eta_0}{2} \exp\bigl(\kappa_0^2/4\kappa_1\bigr) \sqrt{\frac{\pi}{\kappa_1}}\Bigl[\operatorname{erf}(u_d) - \operatorname{erf}(u_0)\Bigr], \tag{4.19}$$

where use has been made of Eqn. 4.15.

Note that in the above it is assumed that $\kappa_1 > 0$ and the solution for Eqn. 4.19 is only valid in this domain. If instead $\kappa_1 < 0$, then Eqn. 4.18 becomes:

$$I_\kappa(d) = \eta_0 \exp\bigl(-\kappa_0^2/4|\kappa_1|\bigr) \int_0^d \exp\bigl(|\kappa_1|\,(z - \kappa_0/2|\kappa_1|)^2\bigr)\ dz. \tag{4.20}$$

This is not analytically integrable but can be expressed using the imaginary error function defined as:

$$\operatorname{erfi}(x) = \frac{2}{\sqrt{\pi}} \int_0^x \exp\bigl(t^2\bigr) dt = -i \operatorname{erf}(ix), \tag{4.21}$$

so that Eqn. 4.20 integrates to:

$$I_\kappa(d) = \frac{\eta_0}{2}\exp\left(-\kappa_0^2/4|\kappa_1|\right)\sqrt{\frac{\pi}{|\kappa_1|}}\Big[\mathrm{erfi}(v_d) - \mathrm{erfi}(v_0)\Big], \tag{4.22}$$

with $v_d = \sqrt{|\kappa_1|}(z - \kappa_0/2|\kappa_1|)$ and $v_0 = -\kappa_0/2\sqrt{|\kappa_1|}$. The limit of Eqn. 4.12 for $\kappa_1 \to 0$ may also be recovered for variations in opacity and is detailed in App. A.

The error functions defined in Eqns. 4.15 and 4.21 are integrable numerically and tabulated in the *Python scipy.special* module [100]. Examples of the form of these solutions are given in Fig. 4.11b using $\kappa_1\, d_\tau/\kappa_0 = \pm 0.05, \pm 0.1, \pm 0.5, \pm 1.0$. The effect of a positive linear change in the opacity is to increase the absorption of photons with distance travelled along the line-of-sight distance, and the curve saturates with increasing distance at a new optically thick limit with a larger opacity. However, a negative linear change decreases the opacity as a function of distance, and in the case of $\kappa_1 d_\tau \to \kappa_0$ allows the total opacity to become negative for distances above the threshold d_τ. This is clearly unphysical behaviour leading to a sign change in the exponent of Eqn. 4.10 and beyond this value the intensity increases exponentially with distance.

As in the emissivity case, incorporating this change to the fitting procedure gives the same fit as before, finding $\kappa_1 \approx 0$, apart from at a few points where the fitting procedure fails due to noise in the data – here the found value of κ_1 is unfeasibly large and ordinarily this happens for the line wings where noise is prevalent.

4.3 Conclusions

In this Chapter it has been shown that the emission spectrum for most lines is insensitive to pulse shape and length provided that the overall fluence remains the same. Increasing or decreasing the fluence yields a commensurate change in the intensity of the emission spectrum. For example, the effect of reducing the fluence is to decrease

the intensity of the lines, because of the corresponding decrease in photoionization rate and peak temperature attained, with a larger effect for the higher energy lines; the overall shape of the spectrum is broadly the same but reduced by around a factor of two. This could go some way to explaining the reduction in the He-α line in Fig. 3.5 for the thinnest target: if Auger electrons are lost from the target then the conversion of laser energy to Auger electrons which then thermalise with the bulk electrons is reduced compared with the thicker targets. The reduction of this line could be used as a signature for Auger electron losses and is discussed in Ch. 6.

The robustness of the method of extracting opacities described in Ch. 3 can be exemplified by considering what happens when one adjusts other pulse parameters. It is found that stretching or compressing the pulse-length (FWHM of the Gaussian) has no appreciable effect on the extracted opacity until the Li-like charge state, and moreover even replacing the pulse with a flat-top pulse of the same length (all conserving the pulse-energy at 1.7 mJ) has a negligible effect. Further, even reducing or increasing the pulse energy by a factor of two only gives a small change to most of the deduced K-shell opacities, and only has a large effect on the higher energy lines. Using a longer pulse length allows the system to evolve in conditions closer to LTE, but the practicality of using this as a method is limited by the radiative recombination lifetime, and disassembly time. Furthermore, the experimentally deduced opacity for the Li-like and He-like lines is lower than that simulated with the nominal parameters and may be due to one of two reasons. Either, the pulse length is shorter than the nominal 100 fs given by the electron bunch, or the pulse energy on target is lower than the 30% of the nominal value given by the measured beamline transmission [88]. This disparity is resolved by moving to three-dimensional simulations in Ch. 5.

The robustness of the shape of the solution to the radiative transfer equation was investigated relaxing certain assumptions and the temporal integration was found to offer some explanation as to the deviation of the fit from the perfect 1D slab

solution. The assumption that the functional form of the time-integrated radiation transfer solution is identical to the instantaneous solution (Eqn. 3.8) transpires to be excellent, and an explanation that the probed opacity is $\sim 40\%$ of the instantaneous maximum is offered by modelling the rise and fall of the emissivity and opacity as Gaussians. The impact of adding a linear variation with distance to the opacity or emissivity was considered and found to not affect the fits found in Ch. 3. However, in reality for the thickest target the emissivity and opacity will both vary as a function of distance as the laser attenuates through the target and should be added in order to model this conclusively. This is investigated in detail in Ch. 5 by building a full three-dimensional model of the target.

Chapter 5

Three-dimensional modelling of spectra

In this Chapter a more detailed three-dimensional model of the plasma is advanced. First, the relevant geometric effects and their relevance are introduced and discussed. Next, three-dimensional SCFLY simulations are built and the resulting derived opacity is shown and compared with the experiment and the simpler zero-dimensional case. It is found that attenuation of the laser through the target is important, and increasing the laser intensity by a factor of two reduces the time taken for the absorption to saturate and the target to become transparent. Including this gives good agreement to both experiment and the zero-dimensional case. Finally, the model is extended beyond the instantaneous case to account for photon time-of-flight effects across the target during the emission. These are not found to affect the preceding results.

5.1 Geometric effects

There has already been a raft of previous work in order to adapt SCFLY into a three-dimensional model, most notably by Rackstraw et al. [55]. In this work, the authors

considered the broadening of K-α lines from an optically thick sample as a function of the fluence and intensity of the X-ray drive when driven on or near resonance, and furthermore their width as a function of the viewing angle. In order to achieve this, an array of cubic cells, or voxels, of side length 100 nm were constructed to mimic the geometry of the target. The laser was allowed to propagate from the front to the back and the output FEL radiation from each layer, accounting for absorption, was passed as the input radiation field to the layer behind to drive the simulation in that layer. The simplicity of this approach relies on the lack self-emission within the plasma. Recall that in many cases, laser-driven plasmas suffer from the effects of self-absorption and this often is taken into account in simple treatments via an escape factor formalism [52, 84]. Earlier this was used to justify that the emissivity and opacity are not functions of thickness along the driving FEL direction, but this may be extended to any direction: the high-intensity FEL dominates the population kinetics, not the emitted radiation from the sample, and allows the ground state populations to be set by LTE and upper state populations to be set by the driving FEL [55]. What would otherwise be a non-trivial radiation transfer problem instead becomes a problem of computational accounting as the evolution within each voxel is independent of its neighbours and only depends on the incoming FEL (attenuated accordingly by the opacity of the layers above).

There are many important modifications between the work of Rackstraw et al. [55] and that described here. The first is the geometric setup of the problem which had to be completely overhauled. For their work, 100 nm cubic voxels were sufficient to encapsulate to good accuracy the emission from the entire plasma as they only considered the cold K-α which is emitted from a large region. In the case discussed here – above the K-edge for all states up to He-like – this approach is insufficient. The highest energy lines are emitted from a small region right near the focal spot of the laser, and a broad-brushed approach with large cells will miss much of the nuanced

evolution for these lines. Instead the geometry of the problem is modified to capture all of the input simulations at different laser intensities, and the voxels are allowed to change size accordingly. The shape of these voxels is determined by how the fluence-scan is modelled [77]. The fluence-scan used to describe the spatial laser drive just has the intensity as a function of enclosed area A, with no indication of the shape. In reality, the beam profile is a complicated shape and is irrelevant for zero-dimensional simulations since the emitted intensity I_n is integrated over the enclosed area (using an appropriate weighting as a function of A_n) as described in Ciricosta et al. [47]. A functionally equivalent method would be instead to calculate the enclosed areas A_n and integrate the emitted intensity across them numerically, for example using the trapezium rule, i.e.:

$$I = \int_0^{A_N} I(A)dA = \sum_{n=1}^{N} \frac{1}{2}(I_n + I_{n-1})(A_n - A_{n-1}), \tag{5.1}$$

an approach which as shown later will allow the integration to be extended into more dimensions.

However, the area subtended will depend on the viewing angle, and the inclination of the target to the incoming FEL. It is assumed that the beam impinging on the target along the FEL direction (i.e. at $\theta_F = 45^\circ$ to the target normal) is comprised of concentrically circular isocontours of intensity so that the enclosed area may be converted to an enclosed radius $r_y = \sqrt{A/\pi}$. Consequently, the shape of the equal intensity annuli as they impinge on the target are stretched along the inclined plane to form ellipses of equation:

$$r_y^2 = x^2 \cos^2(\theta_F) + y^2, \tag{5.2}$$

where the directions are chosen such that the x axis is inclined to the z direction of the FEL by θ_F, and the y axis is not, so the radius in the y direction, corresponding

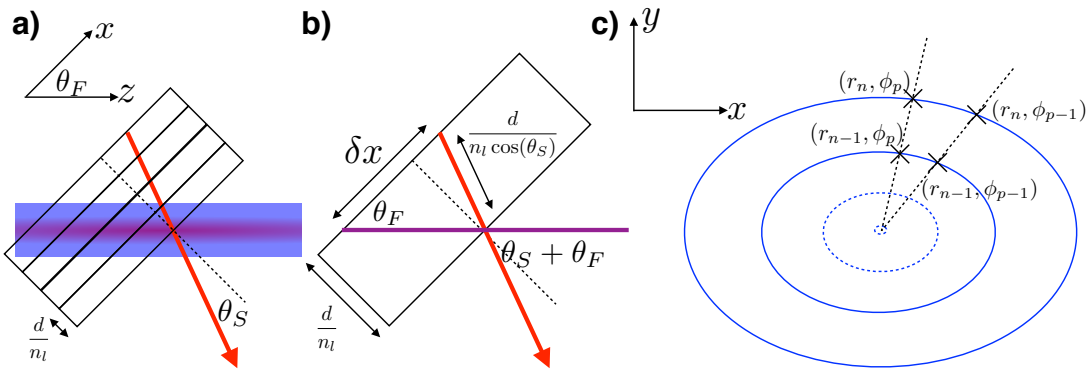

Figure 5.1: a) General schematic of geometry showing the $x-z$ plane including the FEL forming concentrically circular isocontours of intensity in purple impinging the target (divided into n_l slabs) along the z direction at an angle of θ_F to the target normal, and the line-of-sight in red at an angle of θ_S to the target normal. b) Diagram explaining the calculation of δx across the back of the first slab ($k = 1$) as defined in Eqn. 5.5. c) Concentric ellipses viewed on the front surface of target at an angle of θ_S. Relevant points in the calculation in r and ϕ used for the areal integration of Eqns. 5.8-5.11 are labelled.

to the enclosed area in the fluence-scan, is constant for each annulus regardless of inclination angle or viewing angle. The coordinates x and y run perpendicular to the target normal, however it is more useful to choose z to lie along the FEL direction, and not orthogonal to x. The general schematic of the model is shown in Fig. 5.1a.

Of course the observed ellipses are then inclined by the viewing angle $\theta_S = 20°$:

$$r_y^2 = x^2 \frac{\cos^2(\theta_F)}{\cos^2(\theta_S)} + y^2, \tag{5.3}$$

where θ_S is measured in the opposite sense to θ_F (as shown in Fig. 3.1) to simplify the calculation given that in the experiment the angle between the FEL and line-of-sight is $\theta_S + \theta_F = 65°$. Clearly, when $\theta_S = \pm\theta_F$ this recovers the trivial result that the annuli are circles with one important caveat: when $\theta_S = -\theta_F$ and the target is viewed along the FEL direction, the circles have equal emitted intensity as a function of angle ϕ around the circle – this is equivalent to the simple inclined slab investigated in Ch. 3. However, because of the different line-of-sight, when $\theta_S = \theta_F$, the difference

between the angles $\theta_S + \theta_F = 2\theta_F$ is no longer zero and the emitted intensity will vary as a function of angle ϕ.

The way that the emitted intensity is propagated through the target is fairly straight-forward. An angle-resolved (in angle around the ellipse ϕ) direction is chosen to pass through the nominal N simulations that form ellipses on the surface. For clarity the number of equal depth slabs chosen along the z direction shall be called n_l and so for each slab there will be some emitted intensity following Eqn. 3.7:

$$I(k, d/n_l, \theta_S) = \frac{\eta(k)}{\kappa(k)}\Big[1 - \exp\left(-\kappa(k)\,\frac{d}{n_l \cos(\theta_S)}\right)\Big]. \tag{5.4}$$

The emissivity $\eta(k)$, and opacity $\kappa(k)$ are found for each layer k by interpolating between neighbouring simulations on that surface. For example, say that on the front surface the ray passes through the central spot and simulation I_0, but on a layer further back in the target the point of intersection could pass at some distance between the ellipses for simulations with laser intensity I_5 and I_6. Therefore, the emissivity and opacity must be interpolated between these simulations using the fluence-scan.

The distance shift δx between ellipses compared with the front surface of the target ($k = 0$) is found as a function of FEL and viewing angle using the sine rule:

$$\delta x = \frac{k}{n_l}\frac{d}{\cos(\theta_S)}\frac{\sin(\theta_S + \theta_F)}{\sin(\theta_F)}. \tag{5.5}$$

This is shown schematically in Fig. 5.1b. The case of $\theta_S = -\theta_F$ gives the expected result of $\delta x = 0$ – that all the viewed ellipses are aligned with the incoming FEL.

The ellipses viewed on layers behind the front surface are therefore shifted from their coordinates (x, y) on the front layer to a new position $(x + \delta x, y)$ on the layers behind and so the r_y radius of this ellipse must be found:

$$r_y^2 = (x + \delta x)^2 \cos^2(\theta_F) + y^2. \tag{5.6}$$

Recall that the parameter r_y corresponds to an enclosed area (or intensity isocontour) in the fluence-scan and hence an FEL intensity. This allows one to interpolate the required emissivity and opacity.

The emitted intensity from a layer behind is propagated forward by attenuating through the next layer, then the emission from this new layer is calculated and added like so:

$$\begin{aligned} I(n_l-3) = &\Big[\Big[\Big[I(n_l)\exp\left(-\kappa(n_l-1)\,\frac{d}{n_l\cos(\theta_S)}\right) + I(n_l-1, d/n_l, \theta_S)\Big] \\ &\times \exp\left(-\kappa(n_l-2)\,\frac{d}{n_l\cos(\theta_S)}\right) + I(n_l-2, d/n_l, \theta_S)\Big] \\ &\times \exp\left(-\kappa(n_l-3)\,\frac{d}{n_l\cos(\theta_S)}\right) + I(n_l-3, d/n_l, \theta_S)\Big], \end{aligned} \tag{5.7}$$

where the intensity on each layer obeys Eqn. 5.4, and the hindmost layer is $I(n_l) = I(n_l, d/n_l, \theta_S)$. Ergo, the intensity on the surface $I(0)$ is the full product up to the front layer. Clearly, the number of slabs n_l should be chosen to ensure adequate coverage of the focal spot as the emissivity and opacity could change dramatically from one slab to the next near the laser focus, as one deviates from it in steps of δx.

Now that the emission intensity along rays through the target has been found on the front surface of the target it may be integrated in area. Since the intensity varies not only with radius r but also with angle ϕ around the ellipse the two dimensional integral must be found:

$$I = \int_{\phi=0}^{2\pi}\int_{r=0}^{r_N} I(r,\phi) r\,dr\,d\phi = \int_{\phi=0}^{2\pi}\int_{u=0}^{r_N^2} I(u,\phi)\frac{du}{2}d\phi, \tag{5.8}$$

where $r \equiv r(\phi)$ is governed by the observed ellipse of Eqn. 5.3 and in the second step the substitution $u = r^2$ is made. In order to accomplish this a two-dimensional trapezium method is employed. The integrated emission intensity of each annulus must be found. First the 'integration' in r^2 is carried out for each angle ϕ_p using the

trapezium rule:

$$I_n(\phi_p) = \frac{1}{4}[I(r_n^2, \phi_p) + I(r_{n-1}^2, \phi_p)][r_n^2(\phi_p) - r_{n-1}^2(\phi_p)], \tag{5.9}$$

where the radius depends on angle ϕ_p. This is then similarly integrated around in ϕ:

$$I_n = \sum_{p=1}^{N_p} \frac{1}{2}[I_n(\phi_p) + I_n(\phi_{p-1})]\delta\phi, \tag{5.10}$$

with $\delta\phi = 2\pi/N_p$, and N_p the number of evenly-spaced angle points chosen to obtain adequate coverage. These four points in r and ϕ are shown in Fig. 5.1c and labelled according to Eqns. 5.9-5.10. In the following $N_p = 80$ and increasing the resolution has no effect on the final calculated spectrum. These I_n are then summed to find the total intensity (similar to Eqn. 5.1):

$$I = \sum_{n=1}^{N} I_n. \tag{5.11}$$

Finally, this is performed for every time step and simply integrated in time.

5.2 Three-dimensional SCFLY simulations

All targets are split into $n_l = 10$ equal slabs along the FEL direction and a series of SCFLY simulations are set up with thickness $d/(n_l \cos(\theta_F))$. Only 50 timesteps are chosen, half the amount in Ch. 4, without loss of spectral resolution. The thickest target, where these geometric effects will be most pronounced, was also modelled using the full 100 timesteps and using $n_l = 50$ equal slabs. This way each voxel is spaced by $< 30\,\text{nm}$ in z and the distance shift of Eqn. 5.5 for each layer should be $\delta x < 28\,\text{nm}$ for every target. Comparing the spectrum from this higher resolution set of simulations for the thickest target with the coarser gridding of 50 timesteps and 10

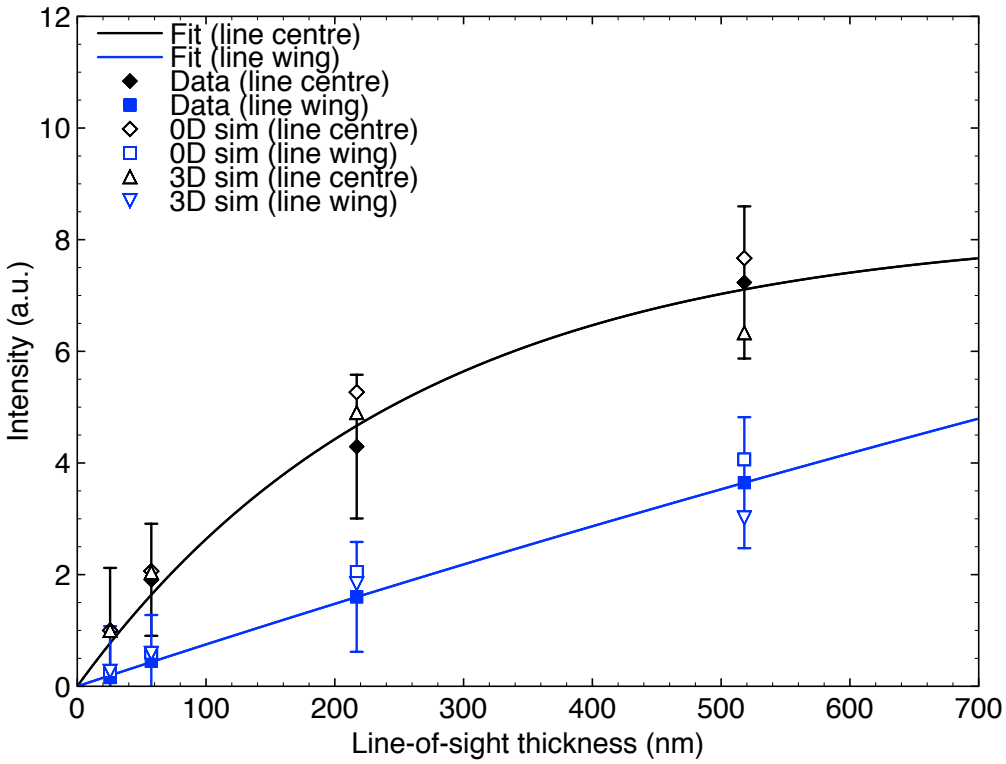

Figure 5.2: The intensity emitted by the four targets, either at a photon energy of 1315 eV (line centre), corresponding to the line centre of line VIII, or at 1325 eV (line wing), corresponding to the region between lines VIII and IX plotted against the line-of-sight thickness d_S. The prediction of space- and time-integrated 3D SCFLY simulations (normalised to overlap the line-centre data for the 24 nm case), and 0D simulations from Fig. 3.6 are also plotted for comparison. The thickest point for the 3D simulation drops as it emits less than expected. Consequently, the latter curve no longer has a linear trend over all thicknesses. In general, a good match is found for the three thinnest targets but not for the thickest target.

slabs was found to have a minimal effect, leading to no loss of spectral fidelity from using a coarser gridding. The FEL is very tightly focussed such that the HWHM measured from the fluence-scan is around 690 nm and its intensity drops below 20% outside of a radius of 1.8 μm from the focus. Consequently, lengths $\sim$ 70 nm (the depth of laminae for the thickest target) should be sufficient to adequately sample lateral gradients and in the following the coarser gridding will be used. The output radiation of each layer, after attenuation by the opacity calculated using the spectral module with a full set of all possible transitions, is fed to the layer behind as an input

radiation source, thus accurately modelling the attenuation of the FEL. For each layer and time step, spectra are calculated and used to populate arrays in emissivity and opacity for the aforementioned calculation. These are integrated in space using the procedure described above and then also in time.

The space and time integrated emission from SCFLY, at two given emitted photon energies, is compared in Fig. 5.2 with the experimental data for the four thicknesses, and found to be a good match within the error bars for the three thinnest targets. However, the thickest target, whilst within experimental error, is found to offer a poorer match to the experimental data, and as mentioned earlier this is not due to a lack of resolution – the higher resolution spectrum gives the same result. Furthermore, the line wing is no longer optically thin and the extracted opacity is now a poor match to the experiment. Consequently, the move towards three-dimensional simulations is having some detrimental effect on the thickest target.

This discrepancy is examined from two directions since two fundamental changes have been made over the 0D simulations. It should either be due to attenuation of the incoming FEL beam through the target, or because of transverse gradients through the sample and the inclined line-of-sight through the emission region. The latter is easily discounted by considering a 3D target where each lamina has the same emissivity and opacity as the front layer, thus removing the effect of attenuation through the target. Under these conditions the final point in Fig. 5.2 increases in intensity and compares well with the experimental result and the 0D simulations expatiated earlier in Ch. 3. The implication of this is that the lateral gradient has a small effect on the spectrum and the use of a one-dimensional simulation (as in Chs. 3 and 4) is reasonable.

However, it would appear from these results that the attenuation is having an effect and the conditions on the rear of the target are different, making the target appear thinner than it really is. This may be investigated in more detail by comparing

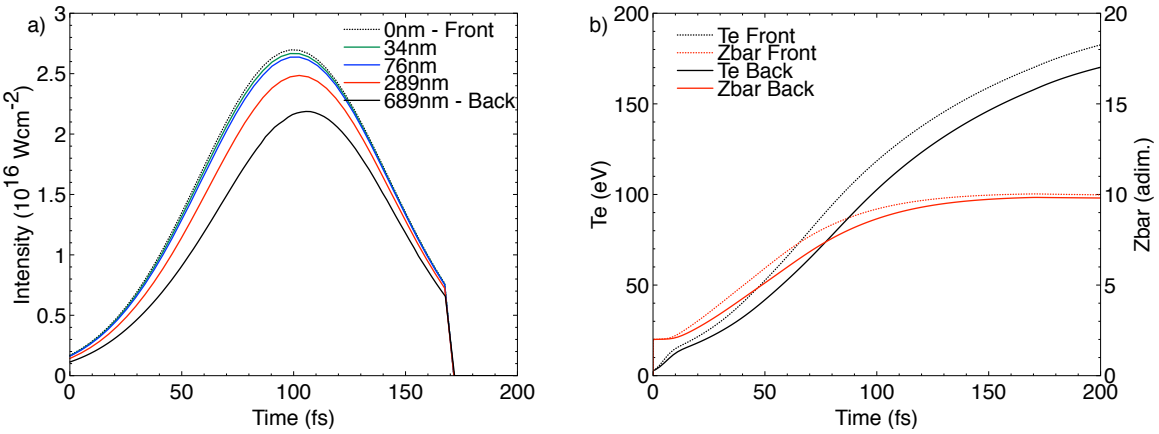

Figure 5.3: a) A comparison of the FEL intensity, integrated in frequency, as a function of time at various points through the target. The back side of the thickest target receives a lower intensity which affects its evolution. b) The temperature and charge state evolution as a function of time between the front and back of the thickest target.

the attenuation of the input FEL through the target, which is done in Fig. 5.3a and through consideration of the evolution of conditions between the front and the back of the target shown in Fig. 5.3b.

Since the FEL's photon energy is above the K-edge for all ionization stages up to He-like, the bound-free opacity is considerable, and consequently the attenuation of the FEL between the front and back is appreciable. The frequency-integrated intensity, $I_\omega(t) = \int I(\omega, t) d\omega$, as a function of time is shown in Fig. 5.3a. This decreases linearly for the three thinnest targets, as expected from Beer's law,

$$I_\omega(z,t) = I_\omega(0,t)\exp(-\kappa(t)z) \approx I_\omega(0,t)[1-\kappa(t)z], \tag{5.12}$$

and has a negligible effect on the spectrum for the 24 nm and 54 nm targets, a small effect for the 204 nm, but clearly is noticable for the thickest target where the FEL length is 689 nm. Correspondingly, there is a lower peak intensity received by the rear side of the target at 100 fs by a factor of 18% and the result is that the evolution is slower and attains a lower final temperature as can be seen in Fig. 5.3b. Subsequently, there is a shift in time at which each charge state peaks on the rear of the target, and

moreover in lower abundances, especially for the upper states with a K-shell hole, because of the smaller photoionization rate leading to less emission from the rear surface.

In their saturable absorption experiment, Rackstraw et al. [79] showed that the plasma evolution is sensitive to the FEL intensity with a higher intensity allowing the plasma to become transparent more quickly. Indeed, further to this, Ciricosta et al. [47] found that they required a larger energy on target greater than the measured value of the beamline transmission, which suffers from being measured with great uncertainty [88]. In their work they found slightly better agreement with the nominal value calculated from the reflectivity of the optical components giving a value of 50% [47]. Therefore, in the same vein as in Ch. 4, it is fruitful to now consider the effect of increasing the FEL energy.

5.2.1 Towards saturable absorption

In exactly the same fashion as above, a 3D simulation for each target was carried out but now with the laser intensity increased by a factor of two, much like the work of Ch. 4.1.3. This would correspond to an increase in the beamline transmission to 60%. Identically with Fig. 5.2, the space and time integrated emission is compared with the experimental data for each thickness in Fig. 5.4. This time, however, each target matches that found experimentally, and a linear trend is recovered for the low opacity region between lines. However, there is still some effect of the attenuation in making the thickest point drop off relative to the others. These 3D simulations are compared with the 0D simulations of Ch. 4.1.3 with the laser intensity doubled (beamline transmission of 60%).

Using the same procedure described in Ch. 3.4.1, the opacity is extracted from these four points and shown in Fig. 5.5 as a function of frequency. In general this opacity is slightly larger than that for the 0D simulations shown in Ch. 4.1.3 as there

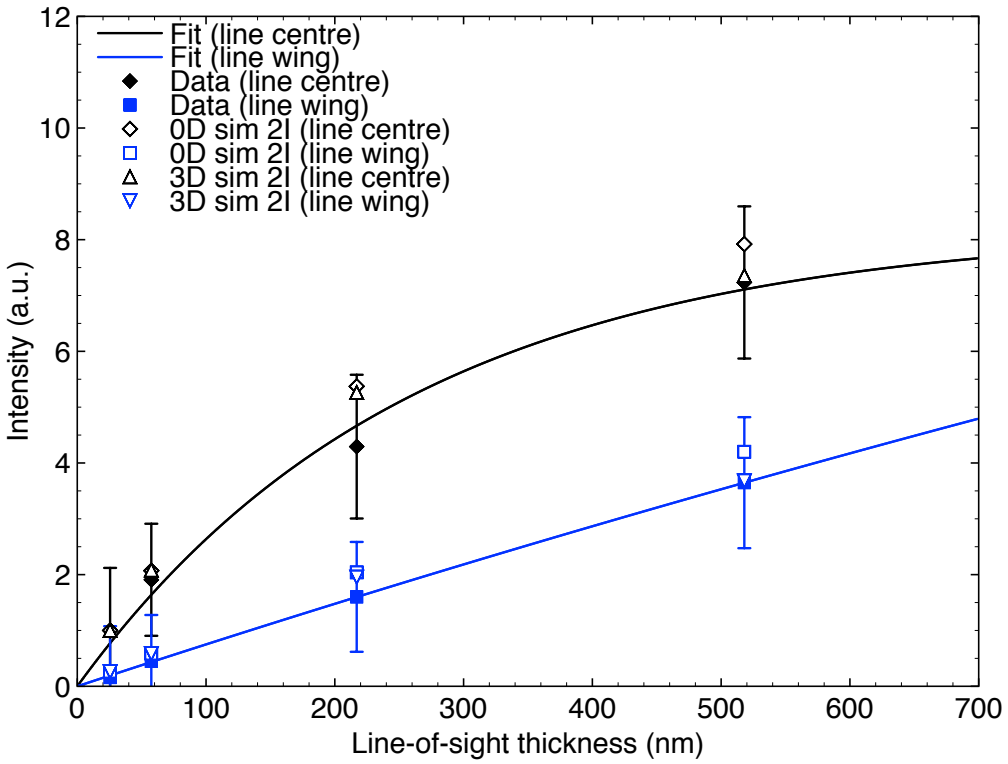

Figure 5.4: The intensity emitted by the four targets, either at a photon energy of 1315 eV (line centre), corresponding to the line centre of line VIII, or at 1325 eV (line wing), corresponding to the region between lines VIII and IX plotted against the line-of-sight thickness d_S. The prediction of space- and time-integrated 3D SCFLY simulations with the laser intensity doubled (normalised to overlap the line-centre data for the 24 nm case), and 0D simulations from Ch. 4.1.3 are also plotted for comparison. A linear trend is recovered again for the simulations of the low opacity region. A good match is found for all targets.

is still some attenuation on the thickest target, however the shape in general is a good match for the experimental data. The final two lines, the Li-α and He-α have a larger opacity which, as seen in Ch. 4.1.3, is a result of the higher intensity laser drive and final higher temperature obtained. It is encouraging to see agreement with all the other lines which are emitted during the plasma's transient evolution earlier in the laser pulse.

However, there is still an effect due to the attenuation and this is most readily viewed in the line wings. The larger opacity on the line wings is attributed to a lower emission intensity from the thickest target. The reason this occurs is twofold.

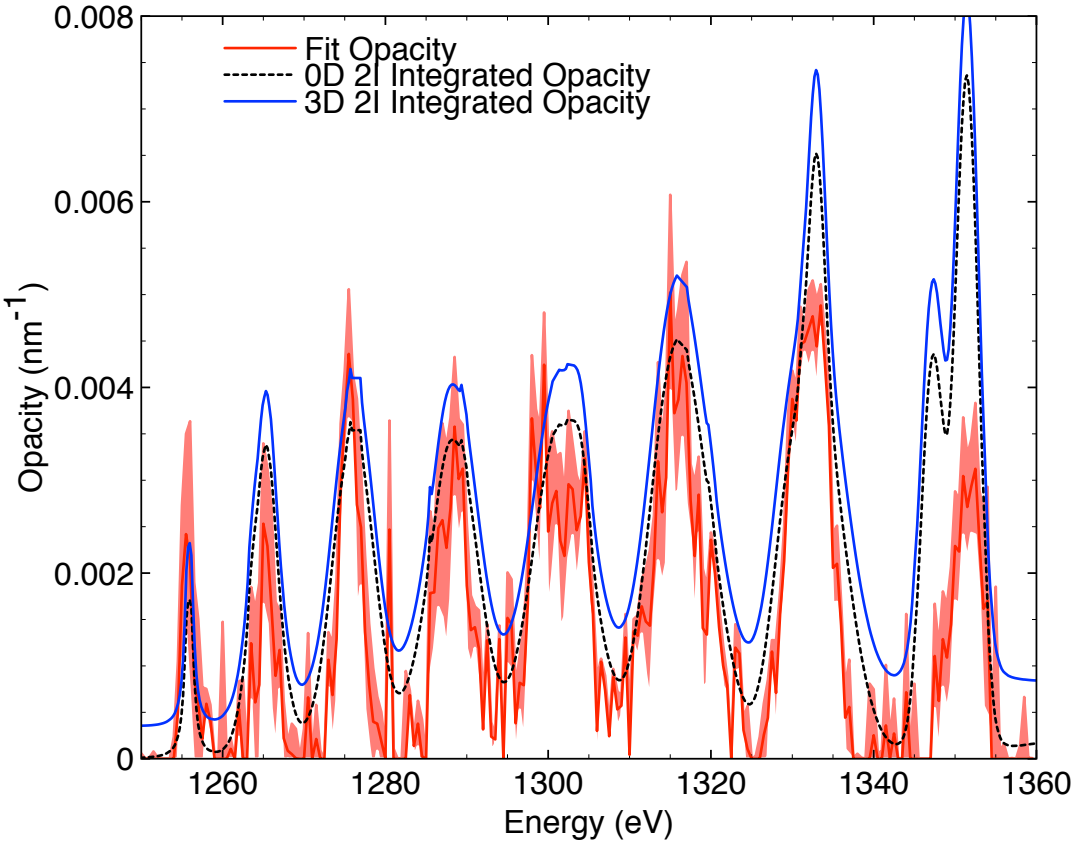

Figure 5.5: A comparison of the fitted experimental opacity $\kappa(\nu)$ with the integrated opacity derived from fitting Eqn. 3.8 to simulated SCFLY spectra. The integrated opacity is a good match to the experimental data and the integrated opacity from 0D simulations with the intensity doubled shown previously in Fig. 4.9.

Firstly, the lower laser intensity reaching the rear of the target results in a longitudinal emission gradient: the rear of the target still emits less in total. But, because of the lower photoionization rate, the emission occurs correspondingly later at the back of the target. The emission therefore passes through a colder region than in the 0D case (since the plasma evolves more slowly at lower laser intensities) as it exits the hot core along the line-of-sight with a corresponding increase in bound-free absorption.

Again, the effect of the attenuation on the laser drive for the thinner targets is small except this time the reduction at the time of peak laser intensity is only 7% on the thickest target. Consequently, as evinced by Fig. 5.6a, the evolution between the front and the back is much more similar as seen in Fig. 5.6b, and at times later than

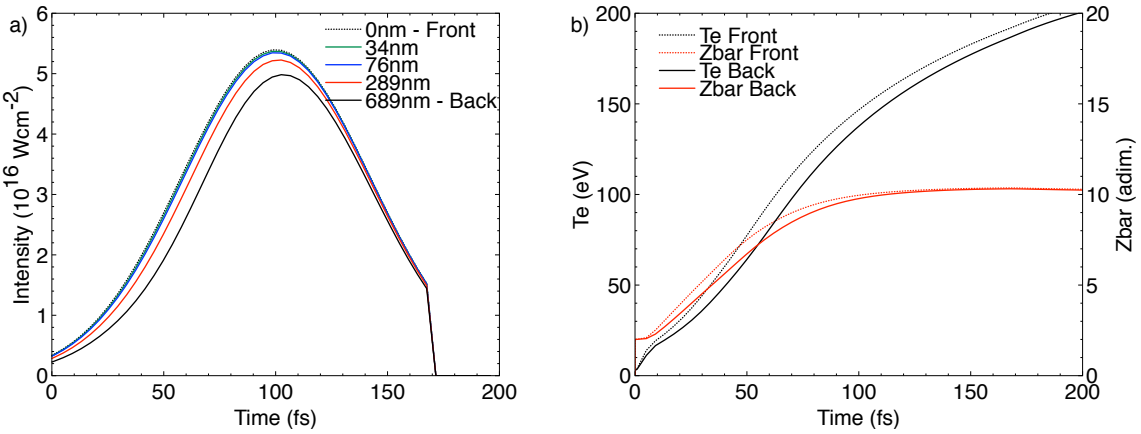

Figure 5.6: a) A comparison of the FEL intensity, integrated in frequency, as a function of time at various points through the target. The attenuation is reduced by using a larger FEL intensity as the target becomes transparent to the X-rays much sooner. b) The temperature and charge state evolution as a function of time between the front and back of the thickest target. The charge state is the same between the front and the back around the time the laser intensity peaks at 100 fs.

the maximum laser intensity the reduction due to attenuation is very small. Indeed, whilst the final temperature obtained in the focal spot is higher, recall from Ch. 4 that this has a minimal effect on the emission spectrum as at this time the ions are stripped to He-like and the ground state population of this charge state varies little over a large range of temperatures (c.f. Fig. 3.10). The greatest effect will be on the upper state K^1L^1 of the He-like ion whose population is dictated by the increased photoionization rate. Moreover, the emission for most charge states occurs at earlier times whilst the sample evolves. As mentioned above, the largest effect of this higher temperature is on the higher-energy lines.

Evidently, there is some trade-off between a high laser intensity to ensure that the target's absorption saturates, minimising the longitudinal gradient in conditions, and burning through the charge states slow enough that they appear under LTE conditions as discussed in Ch. 4. This places limits on the laser intensity: arbitrarily increasing the pulse-length will adversely affect the spectrum as the corresponding lower intensity will lead to higher absorption of X-rays by the thicker targets.

The simulations in this Chapter lend credence to the work of Ciricosta et al. [47]

where they find that a higher beamline transmission is required to better model their spectra. Further to this, if the beamline transmission increases by around a factor of two, then to decrease the integrated opacity from the final two emission lines (the Li-like and He-like) to match the experiment, a corresponding decrease in pulse length from the nominal 100 fs would be required. Again this is borne out by previous work [47, 81, 101, 102] where the required X-ray pulse length has been consistently found to be shorter than the nominal electron bunch duration. The implications of this are discussed in more detail in Ch. 6.

In general, incorporating a larger beamline transmission results in the three-dimensional simulations tending towards the simpler zero-dimensional case of Chs. 3 and 4.

5.3 Photon Time-of-flight effects

It now remains to investigate the final possible effect on the emission spectrum, the time of flight of FEL photons through the target from front to back, and the responding transit of emitted photons from the back to the front – i.e. the effect of photon time-of-flight.

As a simple first approximation, the dielectric properties of the plasma are neglected and it is assumed that photons travel at the speed of light: $c = 300\,\mathrm{nm\,fs^{-1}}$. The integration in time and space must now be completed at the same time to account for the delay in the laser in propagating from one lamina to another which takes a time $t_F = d/(n_l c\cos(\theta_F))$, and the added line-of-sight time until the emission reaches the next lamina $t_S = d/(n_l c\cos(\theta_S))$, where the nominal thickness of each lamina d/n_l is modified by the line-of-sight through the target at θ_S to the normal, and the FEL beam direction at an angle of θ_F. The way this is achieved in practice is to choose the nominal time to be given by the back surface of the target (though

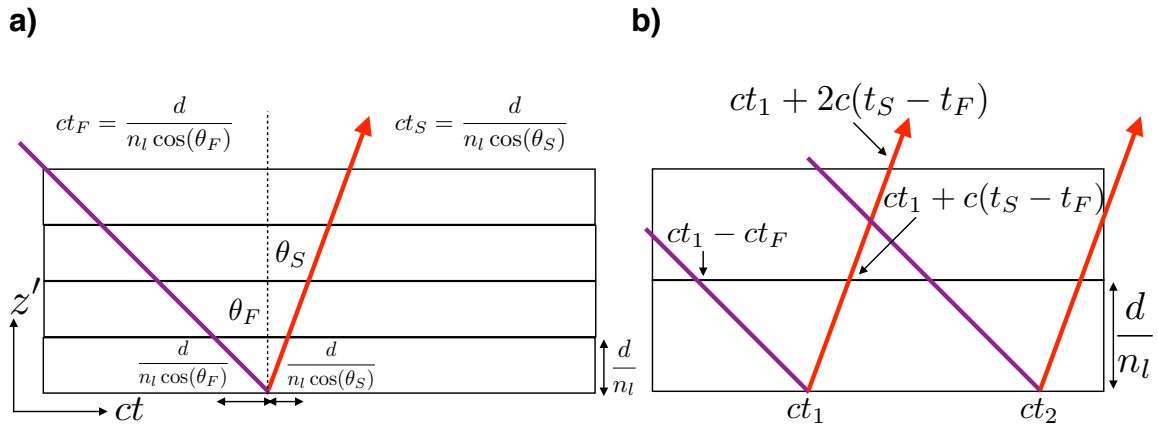

Figure 5.7: a) General schematic of photon time-of-flight geometry showing laminae in the $z' - ct$ plane where z' is the target normal direction and should not be confused with z in Fig. 5.1. The FEL (purple) impinges such that it arrives at each successive slab delayed by $ct_F = d/(n_l \cos(\theta_F))$. The emission then emerges along a line-of-sight such that it reaches successive laminae with a time delay of $ct_S = d/(n_l \cos(\theta_S))$. b) Blow up of part a) in z'. Fixing the nominal time of two events ct_1 and ct_2 to be that at the rear surface of the target, the time that each ray meets the next plane will be offset by $c(t_S - t_F)$. This must be accounted for during the ray propagation of Eqn. 5.13.

of course one could arbitrarily choose any layer as a reference). Each lamina above that, is then shifted back in time by t_F, reflecting the fact that these layers received the FEL at a time $t - t_F$. The emitted photons then reach each subsequent forward layer a time t_S later, so that the total time shift for each layer is $t + (t_S - t_F)$. A schematic diagram of this is shown in Fig. 5.7.

The propagation of Eqn. 5.4 is now explicitly a function of time and must be modified by these delays:

$$I(k, d/n_l, \theta_S, t) = \frac{\eta(k, t + \Delta t)}{\kappa(k, t + \Delta t)} \left[1 - \exp\left(-\kappa(k, t + \Delta t) \frac{d}{n_l \cos(\theta_S)}\right)\right]. \tag{5.13}$$

where $\Delta t = (n_l - k)(t_S - t_F)$ is a function of k recalling that the front slab is $k = 0$ and the rear of the target at n_l is the nominal time so that $\Delta t = 0$.

As laminae vary in thickness, and in order to ensure a smooth transition across each lamina, the output intensity from each lamina is calculated incrementally fol-

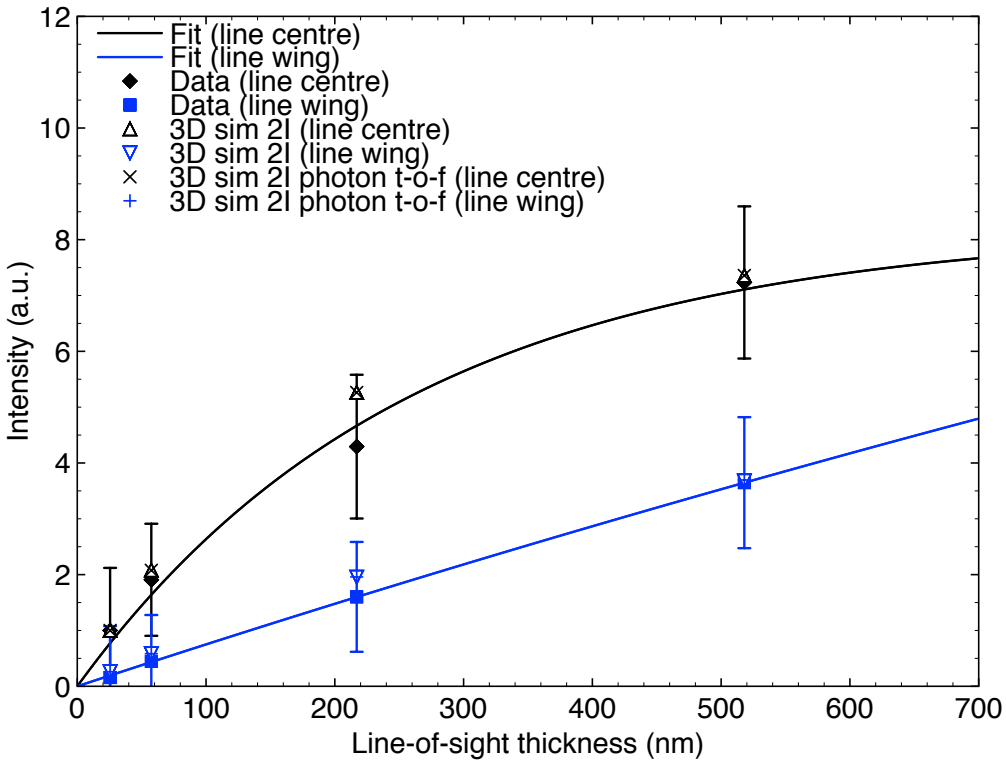

Figure 5.8: The intensity emitted by the four targets, either at a photon energy of 1315 eV (line centre), corresponding to the line centre of line VIII, or at 1325 eV (line wing), corresponding to the region between lines VIII and IX plotted against the line-of-sight thickness d_S. The prediction of space- and time-integrated 3D SCFLY simulations with the laser intensity doubled (normalised to overlap the line-centre data for the 24 nm case) with and without photon time-of-flight (t-o-f) effects are also plotted for comparison. Including these effects has no impact on the spectra.

lowing the procedure of Eqn. 5.7, splitting each lamina into 10 sublaminae of the same emissivity $\eta(k,t)$ and opacity $\kappa(k,t)$. Thus there should be minimal error from "temporal shear" between each lamina due to Δt being too large relative to the internal time-steps, for example if the laminae are widely spaced. Likewise, if $t + \Delta t$ lies between the input 50 time-steps from the SCFLY simulations, it is interpolated between neighbouring time-steps.

Finally, once the space integrated intensity at every time-step has been found on the front surface, it is simply integrated in time as before.

The effect of adding photon time-of-flight effects to the simulations of Fig. 5.4, with a doubled laser intensity, is shown in Fig. 5.8. As expected it is negligible for

the thinner targets where the transit time is near-instantaneous. However, it is also negligible for the thickest target where the travel time for the laser is nearly 2 fs. This corresponds well with the analysis of Ch. 4.2.1 where temporal shifts between emission and absorption, as would be seen if an emitting region at the rear of the target passes through an absorbing region near the front, need to be larger than 10 fs to have any significant effect. There, shifts of 2 fs were negligible.

5.4 Conclusions

In this chapter a full three-dimensional model has been delineated and incorporated into the zero-dimensional simulations of Chs. 3 and 4. The changes introduced by accounting for the angle of the line-of-sight relative to the FEL beam direction is found to be small since the thickness of the target is less than the HWHM of the X-ray spot's spatial profile. Generally, the effect of attenuation through the target is found to be important and it is crucial to ensure that the target receives as small a longitudinal gradient as possible in order to accurately model radiation transfer using the 1D slab solution of Eqn. 3.8. Unlike in Ch. 4 where the extracted opacities were found to be insensitive to variations of the X-ray drive parameters, instead, when attenuation is included, it is paramount to ensure that the intensity on target is high enough such that the absorption quickly saturates within the focal spot, the bound-free opacity concurrently decreases, and the evolution between the front and back are similar. Incorporating this higher beamline transmission reduces the attenuation of the target and results in the three-dimensional model tending to the simpler zero-dimensional case discussed previously. Finally, including photon time-of-flight effects is found not to alter the preceding results.

Chapter 6

Conclusions and Future Work

6.1 Summary and Conclusions

This thesis has presented the results of the first use of X-ray emission spectroscopy from ultra-thin targets as a diagnostic for K-shell opacities. The use of an X-ray FEL ensured the system is well-characterised by just the temporal and spectral profile of the FEL, and facilitates simple modelling using a non-LTE model with just the X-ray drive as the user input.

The system's opacity was extracted from the thickness-dependent emission through fitting to the 1D slab solution of the equation of radiation transfer, and was found to be in good agreement with zero-dimensional atomic-kinetics calculations, as well as simple estimates for the bound-bound opacity.

Whilst a non-LTE model was used for modelling, the solid-density plasma investigated was found to exist in conditions very close to LTE. Furthermore, the transient nature of the plasma's evolution served to gate each K-α line's emission in time, allowing quantitative estimates to be made of the temperature and electron density in the region of the line's emission. Additionally, the emitting and absorbing states for a given K-α line are populated contemporaneously, with the emitting states dic-

tated by the driving FEL and the absorbing given by an LTE population distribution; therefore the fit provided a measure of solid-density LTE opacity.

Since the only user input is the X-ray drive, the effect of altering this in a variety of ways was investigated. The profile was doubled or halved in length, its energy content was doubled or halved, and it was changed to a flat pulse with the same fluence all with no effect on the integrated opacity derived from zero-dimensional simulations for most emission lines. Moreover, increasing the pulse length with the same energy content allowed the system to evolve in conditions closer to LTE due to the consequently lower photoionization rate. The practicality of doing this in reality is limited by the radiative recombination lifetime, which is long reflecting the low fluorescence yield of Mg, and the disassembly time.

Certain approximations made in using the 1D slab solution of the equation of radiation transfer were investigated in more detail. The assumption that the functional form of the time-integrated radiation transfer solution is identical to its instantaneous solution was examined and found to be excellent. Furthermore, adding a linear variation with distance through the target to the opacity or emissivity was also considered and did not affect the previously extracted fits, found by assuming no variation.

A full three-dimensional model was considered which included attenuation of the laser through the target, and the different angles at which the target is heated and the viewed. The effect of traversing a gradient in conditions due to the different heating and viewing directions was found to be minimal, as the longitudinal length was smaller than the transverse size of the focal spot. However, effects due to attenuation were considerable, and in order to accurately model the system with the 1D slab solution, an increase in laser intensity was required, indicating a corresponding increase in the beamline transmission over the published value [88]. This is in agreement with previous work [47]. In the same way as before, the emitted intensity was fitted, and the integrated opacity was found to match the experimental values and those

from 0D simulations with an increased beamline transmission presented in Ch. 4.1.3. Additionally, the effect of photon transit time across the target was included and found to have a negligible effect.

The work of these three chapters indicates that in order to accurately model the entire system, with all emission lines, an increase in the beamline transmission over the measured value of 30% [88] is required in agreement with previous work [47]. Furthermore, if that is the case, a corresponding decrease in the pulse length is required, also in agreement with previous work [47, 81, 101, 102], where the required X-ray pulse length was consistently found to be shorter than the nominal electron bunch duration. Moreover, the work of Ch. 4 found that the measurement of opacity for most lines is robust to a plethora of changes in the X-ray drive pulse parameters, and if one were to do this same experiment again then one would want to make some changes over the parameters chosen in the experiment of Ch. 3. One should aim to use a longer pulse, so that the evolution is as close to LTE as practicable whilst considering that too long a pulse may lead to electron-phonon coupling [54] and disassembly of the plasma before the measurement is complete. One should also bear in mind careful consideration that the X-ray fluence is high enough, such that for thicker targets, the absorption saturates and the heating is as longitudinally uniform as possible.

The shape of the 1D slab solution to the equation of radiative transfer has been shown to exhibit some sensitivity to the time and space integration and to attenuation through the target. A future experiment should include more target thicknesses, particularly around one optical depth where time-integration effects are most pronounced, but also at greater thicknesses. At one optical depth, deviations from the simple solution of Eqn. 3.7, after time and space integration, could be discovered and pinned down in more detail. Additionally, by including some targets with thicknesses much larger than one optical depth, the decrease in emission intensity seen in

Fig. 5.2 could be accredited to a certain thickness and used to better constrain both the beamline transmission and peak intensity on target. Once these are known, the optically thin targets can be used as a constraint on the X-ray pulse length and its differences to the electron bunch duration could be quantified.

Heating isochorically into the HDM regime using an XFEL has already produced profound implications for the modelling of dense plasmas [27, 30, 47, 48, 55]. The work described in this thesis extends this experimental platform into benchmark measurements of the opacity under well known conditions. It affords well-constrained plasma parameters in a facile and tractable way by modelling the simple, single-photon, laser absorption. The electron density and temperature are trivially recovered from the plasma's evolution in time and space. A marked improvement is achieved over traditional methods of measuring opacity, that were discussed in Ch. 2, on multiple fronts. Firstly, the samples are heated isochorically, with minimal longitudinal (and to an extent transverse[1]) gradients and are heated and diagnosed before any hydrodynamic expansion. Secondly, the electron density and temperature are retrieved independently, without discourse to inference from Stark widths [39], line ratios, or isoelectronic dopants [103]. The number of required diagnostics is minimal and an external diagnostic such as X-ray Thomson scattering [104] to verify plasma conditions is not required. Thirdly, the holy grail in all laser-plasma interactions – where the goal is to create HDM in well qualified conditions that may be compared to astrophysical plasmas – is for it to be in LTE. Whilst the creation of atomic vacancies is an intrinsically non-equilibrium process, fortuitously the underlying ground states are in LTE due to the high collisional rates and low fluorescence yield, resulting in an abundance of Auger electrons which rapidly thermalise [47] with the free-electron gas. Consequently, the absorbing states in the plasmas created herein are in LTE. Finally, an X-ray backlighter in this context is superfluous.

[1]Both in terms of line-of-sight, and the ability to model the focal spot.

6.2 Future Work

Opacity measurements on the Z-pinch have spurred a renewed interest in plasmas at solar conditions and the models used to described them. For example, further work [105] to extend the OPAL opacity models [24, 25, 26] to account for the measured discrepancy of Bailey et al. [59] has recently been published. The author of this thesis was heavily involved in a new experiment carried out with the SXR instrument at LCLS, attempting to isochorically heat thin foils of Fe and Ge in the L-shell. It will be interesting to see if the results expounded herein are applicable to these more complicated systems, both in terms of the atomic modelling using SCFLY, but also the method of extracting opacities that is the linchpin of this work. This more complicated system will provide an important acid test as to the wider applicability of emission-based opacity measurements, and could provide another benchmark measurement of iron solar opacities.

With the nascence of new and improved X-ray spectrometers [106, 107, 108] on highly energetic optical lasers such as the National Ignition Facility (NIF) at Lawrence Livermore National Laboratory, USA (LLNL) and the Orion Laser at AWE Aldermaston, UK, benchmark measurements that for decades have been taken as presupposed are being placed on a more rigorous footing. For example, recent measurements [109] using Orion have measured the Stark widths of the He-β line in chlorine and chromium using a high resolution spectrometer with resolving power $E/\Delta E \approx 9000$ [106]. These experiments are challenging in that they must overcome large gradients in temperature and density over which lines are emitted, and distinguish emission lines from different regions *post hoc*, ordinarily through complicated modelling with no measured information on the emitting region's dimensions and gradients. For more dynamic systems, such as ICF implosions, there is a real drive towards shorter gating windows on X-ray streak cameras to enable high-temporal resolution spectroscopic measurements of hot material [107], and high-resolution monochromatic images of

implosions [108]. This provides a tighter constraint on the emitting region, and coupled with the implementation of isoelectronic line ratios allows tighter estimates of the electron temperature [110].

The work in this thesis can be extended to high-resolution measurements of Stark broadened line-widths from a well-defined region, overcoming many of the above problems. For example, modelling with SCFLY, as in Ch. 3, constrains the He-α line to be emitted from a region with $T = 117 \pm 30\,\mathrm{eV}$ and $n_e = 380 \pm 30 \times 10^{21}\,\mathrm{cm}^{-3}$. A line-width measurement using the data in this thesis is in preparation, and will come from a region with conditions constrained to better than 10% in density and 25% in temperature.

As discussed earlier in Ch. 4.1.3, the He-α line of the thinnest (24 nm) target exhibited a lower normalised intensity than expected. It is posited that the reason for this reduction in intensity is because of a lower temperature attained at the end of the laser pulse, due to losses of Auger electrons from the target during the drive. An approximately 1300 eV Auger electron travels at a velocity of $21\,\mathrm{nm\,fs}^{-1}$, and is sufficiently fast to potentially escape from the thinnest 24 nm target by the end of the laser pulse. Furthermore, its most readily available thermalisation channel is not via thermalisation with the free electrons, but rather through a series of collisions with ions leading to a loss of energy and collisional ionization of the impinged upon ions. The thermalisation rate has been investigated in previous work [47] and found to be instantaneous for the $1\,\mu$m plasmas discussed there. A paper is in preparation to model this interaction using the simple 1D diffusion equation and compare with the losses of Auger electrons estimated from spectroscopy. This should afford estimates of the mean-free-path and collisional ionization cross-section.

Finally, the production of optically-thin plasmas enables the measurement of collisional rates in high density plasmas as described in Vinko et al. [53]. Whilst the temperature is too low to collisionally ionize the K-shell, it is high enough to ionize the

L-shell. In the time taken to fill a K-shell hole, another electron can be collisionally ionized from the L-shell changing the ionization stage of the emitting ion. By placing the X-ray photon energy between two edges, for the highest charge state available given the X-ray energy, say K^1L^6, emission may be observed from the next charge state up, K^1L^5, following intermediate collisions. The idea is to clock the collisional rates to the Auger rates by measuring emission below and above an edge. Another paper is in preparation considering the effect of multiple collisions, generating populations with configurations K^1L^4, or K^1L^3, for example, leading to higher energy lines. This should lead to more accurate clocking of the Auger rate to the collisional rate. Further, it will also consider resonantly pumped emission to clock three-body recombination.

To conclude, the work in this thesis describes the application of a successful experimental platform to benchmark measurements of K-shell opacity in hot dense magnesium. These opacities agree very well with atomic-kinetics simulations conducted using SCFLY, and the details of the plasma's evolution allows a diagnosis of the plasma conditions. The creation and verification of optically-thin plasmas opens up a further swathe of benchmark measurements using spectroscopy, from collisional ionization rates to line-widths, in these well-characterised exotic plasmas, and could be used to constrain both the XFEL's beamline transmission and X-ray pulse length.

Appendix A

Derivation of limit as a linear variation in opacity tends to zero

Recovering the limit of Eqn. 4.12 in the limit of $\kappa_1 \to 0$ is more challenging but perfectly possible. The series expansion of the error function as $x \to \infty$ is required:

$$\lim_{x\to\infty} \mathrm{erf}(x) = 1 - \frac{\exp(-x^2)}{\sqrt{\pi}x}. \tag{A.1}$$

Eqn. 4.19 now becomes

$$I_\kappa(d) = \frac{\eta_0}{2}\exp\big(\kappa_0^2/4\kappa_1\big)\sqrt{\frac{\pi}{\kappa_1}}\Big[1 - \frac{\exp(-u_d^2)}{\sqrt{\pi}u_d} - 1 + \frac{\exp(-u_0^2)}{\sqrt{\pi}u_0}\Big]. \tag{A.2}$$

Using

$$u_d = u_0(1 + 2\kappa_1^{3/2}d/\kappa_0), \tag{A.3}$$

and so as $\kappa_1 \to 0$ then $u_d \to u_0$, the second term in the bracket may be expanded:

$$\frac{\exp(-u_d^2)}{\sqrt{\pi}u_d} = \exp\big(-\kappa_1 d^2\big)\exp(-\kappa_0 d)\frac{\exp(-u_0^2)}{\sqrt{\pi}u_d} \approx \exp\big(-\kappa_1 d^2\big)\exp(-\kappa_0 d)\frac{\exp(-u_0^2)}{\sqrt{\pi}u_0}. \tag{A.4}$$

The bracket is then re-expressed as:

$$I_\kappa(d) = \frac{\eta_0}{2}\exp\big(\kappa_0^2/4\kappa_1\big)\sqrt{\frac{\pi}{\kappa_1}}\Big[1-\exp\big(-\kappa_1 d^2\big)\exp(-\kappa_0 d)\Big]\frac{\exp(-u_0^2)}{\sqrt{\pi}u_0}. \tag{A.5}$$

Rearranging, substituting for u_0:

$$I_\kappa(d) = \frac{\eta_0}{2}\exp\big(\kappa_0^2/4\kappa_1\big)\exp\big(-\kappa_0^2/4\kappa_1\big)\frac{2\sqrt{\kappa_1}}{\kappa_0\sqrt{\kappa_1}}\Big[1-\exp\big(-\kappa_1 d^2\big)\exp(-\kappa_0 d)\Big], \tag{A.6}$$

and cancelling yields,

$$I_\kappa(d) = \frac{\eta_0}{\kappa_0}\Big[1-\exp\big(-\kappa_1 d^2\big)\exp(-\kappa_0 d)\Big]. \tag{A.7}$$

Finally, letting the only remaining $\kappa_1 \to 0$ gives the required result of Eqn. 4.12. The process is similar for $\kappa_1 < 0$ starting from Eqn. 4.22.

Bibliography

[1] FLASH website. `http://flash.desy.de/`. 2, 31

[2] V. Ayvazyan, N. Baboi, J. Bähr, V. Balandin, B. Beutner, et al. First operation of a free-electron laser generating GW power radiation at 32 nm wavelength. *The European Physical Journal D*, 37(2):297–303, 2006. 2

[3] LCLS website. `http://lcls.slac.stanford.edu/`. 2

[4] P. Emma, R. Akre, J. Arthur, R. Bionta, C. Bostedt, et al. First lasing and operation of an ångstrom-wavelength free-electron laser. *Nature Photonics*, 4 (9):641–647, 2010. 2, 4, 54, 74

[5] FERMI website. `http://www.elettra.eu/lightsources/fermi.html`. 2

[6] SACLA website. `http://xfel.riken.jp/eng/`. 2

[7] European XFEL website. `http://www.xfel.eu/`. 2

[8] SwissFEL website. `https://www.psi.ch/swissfel/`. 2

[9] PAL-XFEL website. `http://pal.postech.ac.kr/paleng/`. 2

[10] John M J Madey. Stimulated emission of bremsstrahlung in a periodic magnetic field. *Journal of Applied Physics*, 42(5):1906–1913, 1971. 2

[11] Zhirong Huang and Kwang Je Kim. Review of x-ray free-electron laser theory. *Physical Review Special Topics - Accelerators and Beams*, 10(3):034801, 2007. 2, 4

[12] Hiroyuki Daido. Review of soft x-ray laser researches and developments. *Reports on Progress in Physics*, 65(10):1513–1576, 2002. 4

[13] R. Bonifacio, C. Pellegrini, and L. M. Narducci. Collective instabilities and high-gain regime in a free electron laser. *Optics Communications*, 50(6):373–378, 1984. 4

[14] Norman Kroll and Wayne McMullin. Stimulated emission from relativistic electrons passing through a spatially periodic transverse magnetic field. *Physical Review A*, 17(1):300–308, 1978. 4

[15] S. V. Milton. Exponential Gain and Saturation of a Self-Amplified Spontaneous Emission Free-Electron Laser. *Science*, 292(5524):2037–2041, 2001. 4

[16] E. L. Saldin, E. A. Schneidmiller, and M. V. Yurkov. Self-amplified spontaneous emission FEL with energy-chirped electron beam and its application for generation of attosecond x-ray pulses. *Physical Review Special Topics - Accelerators and Beams*, 9(5):1–6, 2006. 5

[17] W F Schlotter, J J Turner, M Rowen, P Heimann, M Holmes, et al. The soft x-ray instrument for materials studies at the linac coherent light source x-ray free-electron laser, 2012. 5, 39

[18] P Debye and E Hückel. Zur theorie der elektrolyte. *Phys. Z*, 24(9):185–206, 1923. 5

[19] John Lindl. Development of the indirect-drive approach to inertial confinement fusion and the target physics basis for ignition and gain. *Physics of Plasmas*, 2 (11):3933, 1995. 5, 22

[20] John D. Lindl, Peter Amendt, Richard L. Berger, S. Gail Glendinning, Siegfried H. Glenzer, Steven W. Haan, Robert L. Kauffman, Otto L. Landen, and Laurence J. Suter. The physics basis for ignition using indirect-drive targets on the National Ignition Facility. *Physics of Plasmas*, 11(2):339, 2004. 5, 22

[21] D. Colombant, M. Klapisch, and A. Bar-Shalom. Increase in Rosseland mean opacity for inertial fusion hohlraum walls. *Physical Review E*, 57(3):3411–3416, 1998. 5, 22, 25, 32

[22] John N. Bahcall, Walter F. Huebner, Stephen H. Lubow, Peter D. Parker, and Roger K. Ulrich. Standard solar models and the uncertainties in predicted capture rates of solar neutrinos. *Reviews of Modern Physics*, 54(3):767–799, 1982. 5

[23] D. B. Guenther, P. Demarque, Y.-C. Kim, and M. H. Pinsonneault. Standard solar model. *The Astrophysical Journal*, 387:372, 1992. 5

[24] C A Iglesias and F J Rogers. Opacities for the solar radiative interior. *The Astrophysical Journal*, 371:408, 1991. 6, 26, 122

[25] C. A. Iglesias and F. J. Rogers. Updated OPAL opacities. *The Astrophysical Journal*, 464, 1996. 6, 26, 122

[26] Forrest J. Rogers, Fritz J. Swenson, and Carlos A. Iglesias. OPAL Equation-of-State Tables for Astrophysical Applications. *The Astrophysical Journal*, 456: 902, 1996. 6, 26, 122

[27] S. M. Vinko, O. Ciricosta, B. I. Cho, K. Engelhorn, H-K Chung, et al. Creation and diagnosis of a solid-density plasma with an X-ray free-electron laser. *Nature*, 482(7383):59–62, 2012. 6, 15, 29, 54, 62, 121

[28] J Bailey, A. L. Carlson, G. Chandler, M S Derzon, R J Dukart, et al. Observation of Kα. X-ray satellites from a target heated by an intense ion beam. *Laser and Particle Beams*, 8(04):555—-562, 1990. 6, 43

[29] Sam M. Vinko. X-ray free-electron laser studies of dense plasmas. *Journal of Plasma Physics*, 81(05):365810501, 2015. 7

[30] O. Ciricosta, S. M. Vinko, H.-K. Chung, B. I. Cho, C. R D Brown, et al. Direct measurements of the ionization potential depression in a dense plasma. *Physical Review Letters*, 109(065002), 2012. 7, 11, 12, 14, 31, 47, 54, 57, 74, 121

[31] J. C. Stewart and K. D. Pyatt, Jr. Lowering of Ionization Potentials in Plasmas. *The Astrophysical Journal*, 144(3):1203–1211, 1966. 8, 10

[32] Thomas R. Preston, Sam M. Vinko, Orlando Ciricosta, Hyun-Kyung Chung, Richard W. Lee, and Justin S. Wark. The effects of ionization potential depression on the spectra emitted by hot dense aluminium plasmas. *High Energy Density Physics*, 9(2):258–263, 2013. 8, 10, 11, 19, 57

[33] Hans R. Griem. *Plasma Spectroscopy*. McGraw-Hill., London, UK, 1964. 8, 10, 23, 56, 59, 62

[34] G. Ecker and W. Kroll. Lowering of the Ionization Energy for a Plasma in Thermodynamic Equilibrium. *Physics of Fluids*, 6(1):62, 1963. 10, 11

[35] R. Florido, R. C. Mancini, T. Nagayama, R. Tommasini, J. A. Delettrez, S. P. Regan, and B. Yaakobi. Measurements of core and compressed-shell temperature and density conditions in thick-wall target implosions at the OMEGA laser facility. *Physical Review E - Statistical, Nonlinear, and Soft Matter Physics*, 83 (6):1–7, 2011. 11

[36] D. A. Haynes Jr, D. T. Garber, C. F. Hooper Jr, R. C. Mancini, Y. T. Lee, D. K. Bradley, J. Delettrez, R. Epstein, and P. A. Jaanimagi. Effects of ion dynamics and opacity on Stark-broadened argon line profiles. *Physical Review E*, 53(1):1042, 1996. 11

[37] S. P. Regan, J. A. Delettrez, R. Epstein, P. A. Jaanimagi, B. Yaakobi, et al. Characterization of direct-drive-implosion core conditions on OMEGA with time-resolved Ar K-shell spectroscopy. *Physics of Plasmas*, 9(4):1357, 2002. 11

[38] L. Welser-Sherrill, R. C. Mancini, J. A. Koch, N. Izumi, R. Tommasini, et al. Spectroscopic study of temperature and density spatial profiles and mix in implosion cores. *AIP Conference Proceedings*, 1058:199–206, 2008. 11

[39] J. D. Kilkenny, R. W. Lee, M. H. Key, and J. G. Lunney. X-ray spectroscopic diagnosis of laser-produced plasmas, with emphasis on line broadening. *Physical Review A*, 22(6):2746–2760, 1980. 11, 27, 121

[40] D. J. Hoarty, P. Allan, S. F. James, C. R. D. Brown, L. M. R. Hobbs, et al. Observations of the Effect of Ionization-Potential Depression in Hot Dense Plasma. *Physical Review Letters*, 110(26):265003, 2013. 11, 12

[41] D. J. Hoarty, P. Allan, S. F. James, C. R. D. Brown, L. M. R. Hobbs, et al. The first data from the Orion laser; measurements of the spectrum of hot, dense aluminium. *High Energy Density Physics*, 9(4):661–671, 2013. 11

[42] Carlos A. Iglesias. A plea for a reexamination of ionization potential depression measurements. *High Energy Density Physics*, 12:5–11, 2014. 12, 13

[43] S. M. Vinko, O. Ciricosta, and J. S. Wark. Density functional theory calculations of continuum lowering in strongly coupled plasmas. *Nature Communications*, 5:1–7, 2014. 12, 14, 57

[44] Sang-Kil Son, Robert Thiele, Zoltan Jurek, Beata Ziaja, and Robin Santra. Quantum-Mechanical Calculation of Ionization-Potential Lowering in Dense Plasmas. *Physical Review X*, 4(3):031004, 2014. 12

[45] S. Bhattacharyya, J. K. Saha, and T. K. Mukherjee. Nonrelativistic structure calculations of two-electron ions in a strongly coupled plasma environment. *Physical Review A*, 91(4):042515, 2015. 12

[46] M. Stransky. Monte Carlo simulations of ionization potential depression in dense plasmas. *Physics of Plasmas*, 23(1):012708, 2016. 12

[47] O Ciricosta, S M Vinko, H. K. Chung, C Jackson, R W Lee, T R Preston, D S Rackstraw, and J S Wark. Detailed model for hot-dense aluminum plasmas generated by an X-ray free electron laser. *Physics of Plasmas*, 23(022707), 2016. 13, 18, 19, 21, 29, 30, 40, 46, 54, 57, 62, 75, 87, 102, 110, 113, 114, 119, 120, 121, 123

[48] O Ciricosta, S M Vinko, B Barbrel, D S Rackstraw, T R Preston, et al. Measurements of continuum lowering in solid-density plasmas created from elements and compounds. *Nature communications*, 7(May):1–6, 2016. 13, 16, 17, 18, 19, 62, 121

[49] J. C. Slater and G. F. Koster. Simplified LCAO method for the periodic potential problem. *Physical Review*, 94(6):1498–1524, 1954. 14

[50] H.-K. Chung, M. H. Chen, and R. W. Lee. Extension of atomic configuration sets of the Non-LTE model in the application to the Kα diagnostics of hot dense matter. *High Energy Density Physics*, 3(1-2):57–64, 2007. 14, 54, 57, 61

[51] H.-K. Chung, M. H. Chen, W. L. Morgan, Y. Ralchenko, and R. W. Lee. FLYCHK: Generalized population kinetics and spectral model for rapid spectroscopic analysis for all elements. *High Energy Density Physics*, 1(1):3–12, 2005. 14, 74

[52] G. J. Phillips, J. S. Wark, F. M. Kerr, S. J. Rose, and R. W. Lee. Escape factors in zero-dimensional radiation-transfer codes. *High Energy Density Physics*, 4 (1-2):18–25, 2008. 15, 34, 49, 95, 101

[53] S. M. Vinko, O. Ciricosta, T. R. Preston, D. S. Rackstraw, C.R.D. Brown, et al. Investigation of femtosecond collisional ionization rates in a solid-density aluminium plasma. *Nature Communications*, 6:6397, 2015. 16, 19, 45, 54, 70, 87, 123

[54] Zhibin Lin, Leonid V. Zhigilei, and Vittorio Celli. Electron-phonon coupling and electron heat capacity of metals under conditions of strong electron-phonon nonequilibrium. *Physical Review B - Condensed Matter and Materials Physics*, 77(7):1–17, 2008. 18, 68, 120

[55] D. S. Rackstraw, S. M. Vinko, O. Ciricosta, B. I. Cho, K. Engelhorn, et al. Opacity effects in a solid-density aluminium plasma created by photo-excitation with an X-ray laser. *High Energy Density Physics*, 11:59–69, 2014. 21, 29, 35, 48, 49, 54, 100, 101, 121

[56] Harris L. Mayer. Opacity calculations, past and future. *Journal of Quantitative Spectroscopy and Radiative Transfer*, 4(5):585–595, 1964. 22

[57] G. A. Rochau, J. E. Bailey, R. E. Falcon, G. P. Loisel, T. Nagayama, R. C. Mancini, I. Hall, D. E. Winget, M. H. Montgomery, and D. A. Liedahl. ZAPP: The Z Astrophysical Plasma Properties collaboration. *Physics of Plasmas*, 21 (5), 2014. 22, 32

[58] J. E. Bailey, G. A. Rochau, C. A. Iglesias, J. Abdallah, J. J. MacFarlane, et al. Iron-plasma transmission measurements at temperatures above 150 eV. *Physical Review Letters*, 99(26):1–4, 2007. 22, 32

[59] J E Bailey, T Nagayama, G P Loisel, G A Rochau, C Blancard, et al. A higher-than-predicted measurement of iron opacity at solar interior temperatures. *Nature*, 517(56), 2015. 22, 26, 27, 32, 72, 122

[60] J. M. Foster, D. J. Hoarty, C. C. Smith, P. A. Rosen, S. J. Davidson, S. J. Rose, T. S. Perry, and F. J. D. Serduke. L -shell absorption spectrum of an open- M -shell germanium plasma: Comparison of experimental data with a detailed configuration-accounting calculation. *Physical Review Letters*, 67(23): 3255–3258, 1991. 22, 26, 32

[61] N. Grevesse and A. J. Sauval. Standard solar composition, 1998. 23

[62] J. E. Bailey, G. A. Rochau, R. C. Mancini, C. A. Iglesias, J. J. MacFarlane, I. E. Golovkin, C. Blancard, Ph Cosse, and G. Faussurier. Experimental investigation of opacity models for stellar interior, inertial fusion, and high energy density plasmas. *Physics of Plasmas*, 16(5), 2009. 23, 24, 27, 28, 32

[63] Franck Delahaye and Marc Pinsonneault. Comparison of Radiative Accelerations Obtained with Atomic Data from OP and OPAL. *The Astrophysical Journal*, 625(1):563–574, 2005. 23

[64] Dimitri Mihalas. *Stellar Atmospheres*. W. H. Freeman and Co., San Francisco, USA, 2 edition, 1978. 25, 35, 56, 59, 62

[65] S. J. Rose. The radiative opacity at the Sun centre - A code comparison study. *Journal of Quantitative Spectroscopy and Radiative Transfer*, 71(2-6):635–638, 2001. 25

[66] Mordecai D. Rosen. The science applications of the high-energy density plasmas created on the Nova laser. *Physics of Plasmas*, 3(5):1803, 1996. 25, 32

[67] C.L.S. Lewis and J. McGlinchey. Quasi-monochromatic, projection radiography of dense laser driven spherical targets. *Optics Communications*, 53(3):179–186, 1985. 26

[68] D. J. Hoarty, J. W O Harris, P. Graham, S. J. Davidson, S. F. James, B. J B Crowley, E. L. Clark, C. C. Smith, and L. Upcraft. Measurements of niobium absorption spectra in plasmas with nearly full M-shell configurations. *High Energy Density Physics*, 3(3-4):325–334, 2007. 26, 32

[69] B. J B Crowley and J. W. Harris. Modelling of plasmas in an average-atom local density approximation: The CASSANDRA code. *Journal of Quantitative Spectroscopy and Radiative Transfer*, 71(2-6):257–272, 2001. 26

[70] David J. Hoarty, C. D. Bentley, B. J B Crowley, S. J. Davidson, S. G. Gales, P. Graham, J. W O Harris, C. A. Iglesias, S. F. James, and C. C. Smith. The effect of line-broadening on the overall width of transition arrays in dense plasmas. *Journal of Quantitative Spectroscopy and Radiative Transfer*, 99(1-3): 283–294, 2006. 26, 32

[71] Carlos A. Iglesias. Enigmatic photon absorption in plasmas near solar interior conditions. *High Energy Density Physics*, 15:4–7, 2015. 26

[72] H. A. Scott and S. B. Hansen. Advances in NLTE modeling for integrated simulations. *High Energy Density Physics*, 6(1):39–47, 2010. 26, 35

[73] Sultana N. Nahar, Anil K. Pradhan, Guo Xin Chen, and Werner Eissner. Highly excited core resonances in photoionization of Fe xvii: Implications for plasma opacities. *Physical Review A - Atomic, Molecular, and Optical Physics*, 83(5): 1–12, 2011. 27

[74] H. R. Griem. Stark Broadening under Extreme Plasma Conditions. *Physica Scripta*, T83(1):142, 1999. 27

[75] T. Nagayama, J. E. Bailey, R. C. Mancini, C. A. Iglesias, S. B. Hansen, et al. Model uncertainties of local-thermodynamic-equilibrium K-shell spectroscopy. *High Energy Density Physics*, 20:17–22, 2016. 27

[76] T. S. Perry, P. T. Springer, D. F. Fields, D. R. Bach, F. J. D. Serduke, et al. Absorption experiments on x-ray-heated mid- Z constrained samples. *Physical Review E*, 54(5):5617–5631, 1996. 27

[77] J. Chalupský, J. Krzywinski, L. Juha, V. Hájková, J. Cihelka, et al. Spot size characterization of focused non-Gaussian X-ray laser beams. *Optics express*, 18 (26):27836–45, 2010. 28, 29, 40, 54, 102

[78] J Chalupsky, P Bohacek, V Hajkova, S.P. Hau-Riege, P.A. Heimann, et al. Comparing different approaches to characterization of focused X-ray laser beams. *Nuclear Instruments and Methods in Physics Research Section A: Accelerators, Spectrometers, Detectors and Associated Equipment*, 631(1):130–133, 2011. 29

[79] D. S. Rackstraw, O. Ciricosta, S. M. Vinko, B. Barbrel, T. Burian, et al. Saturable Absorption of an X-Ray Free-Electron-Laser Heated Solid-Density Aluminum Plasma. *Physical Review Letters*, 015003(114):1–5, 2015. 31, 72, 94, 110

[80] B. Nagler, U. Zastrau, R. R. Fäustlin, S. M. Vinko, T. Whitcher, et al. Turning solid aluminium transparent by intense soft X-ray photoionization. *Nature Physics*, 5(9):693–696, 2009. 31

[81] L Young, E P Kanter, B Krässig, Y Li, A M March, et al. Femtosecond electronic response of atoms to ultra-intense X-rays. *Nature*, 466(7302):56–61, 2010. 31, 114, 120

[82] M. Hoener, L. Fang, O. Kornilov, O. Gessner, S. T. Pratt, et al. Ultraintense x-ray induced ionization, dissociation, and frustrated absorption in molecular nitrogen. *Physical Review Letters*, 104(25):1–5, 2010. 31

[83] Sebastian Schorb, Daniela Rupp, Michelle L. Swiggers, Ryan N. Coffee, Marc Messerschmidt, et al. Size-dependent ultrafast ionization dynamics of nanoscale samples in intense femtosecond x-ray free-electron-laser pulses. *Physical Review Letters*, 108(23):1–5, 2012. 31

[84] T Holstein. Imprisonment of resonance radiation in gases. *Physical Review*, 72 (12):1212–1233, 1947. 34, 49, 101

[85] J.P. Apruzese. Direct solution of the equation of transfer using frequency- and angle-averaged photon-escape probabilities for spherical and cylindrical geometries. *Journal of Quantitative Spectroscopy and Radiative Transfer*, 25(5): 419–425, 1981. 34

[86] S J Rose. The non-LTE excitation/ionization code GALAXY. *Journal of Physics B: Atomic, Molecular and Optical Physics*, 31(9):2129–2144, 1998. 34

[87] Eugene R. Capriotti. Mean Escape Probabilities of Line Photons. *The Astrophysical Journal*, 142:1101, 1965. 34

[88] K Tiedtke, A A Sorokin, U Jastrow, P. Juranić, S Kreis, et al. Absolute pulse energy measurements of soft x-rays at the Linac Coherent Light Source. *Optics Express*, 22(18):21214, 2014. 40, 54, 98, 110, 119, 120

[89] J. Schweppe, R.D. Deslattes, T. Mooney, and C.J. Powell. Accurate measurement of Mg and Al Kα1,2 X-ray energy profiles. *Journal of Electron Spectroscopy and Related Phenomena*, 67(3):463–478, 1994. 43

[90] B.L. Henke, E.M. Gullikson, and J.C. Davis. X-ray interactions: Photoabsorption, scattering, transmission, and reflection at e = 50-30,000 ev, z = 1-92. *Atomic Data and Nuclear Data Tables*, 54(2):181 – 342, 1993. 45

[91] G. Cristoforetti, A. De Giacomo, M. Dell'Aglio, S. Legnaioli, E. Tognoni, V. Palleschi, and N. Omenetto. Local Thermodynamic Equilibrium in Laser-Induced Breakdown Spectroscopy: Beyond the McWhirter criterion. *Spectrochimica Acta Part B: Atomic Spectroscopy*, 65(1):86–95, 2010. 45, 46

[92] Orlando Ciricosta. Plasma evolution and Continuum Lowering in Hot Dense Matter generated by X-ray Free Electron Lasers. D.Phil. Thesis, 2014. 47

[93] G.J. Tallents. Free electron degeneracy effects on collisional excitation, ionization, de-excitation and three-body recombination. *High Energy Density Physics*, 20:9–16, 2016. 47

[94] Python scipy.optimize.curve_fit documentation website. `https://docs.scipy.org/doc/scipy-0.18.1/reference/generated/scipy.optimize.curve_fit.html`, . 51

[95] William H. Press and William T. Vetterling. *Numerical recipes in C: the art of scientific computing*. Cambridge University Press, Cambridge, UK, 2 edition, 1992. 51

[96] A. Bar-Shalom, J. Oreg, W. H. Goldstein, D. Shvarts, and A. Zigler. Supertransition-arrays: A model for the spectral analysis of hot, dense plasma. *Physical Review A*, 40(6):3183–3193, 1989. 57

[97] Los alamos atomic physics code website. `http://aphysics2.lanl.gov/tempweb/lanl/`. 58

[98] H A Kramers. XCIII. On the theory of X-ray absorption and of the continuous X-ray spectrum. *Philosophical Magazine Series 6*, 46(275):836–871, 1923. 74

[99] R. Bonifacio, L. De Salvo, P. Pierini, N. Piovella, and C. Pellegrini. Spectrum, temporal structure, and fluctuations in a high-gain free-electron laser starting from noise. *Physical Review Letters*, 73(1):70–73, 1994. 75

[100] Python scipy.special documentation website. `https://docs.scipy.org/doc/scipy-0.16.0/reference/special.html`, . 97

[101] Orlando Ciricosta, Hyun-Kyung Chung, Richard W. Lee, and Justin S. Wark. Simulations of neon irradiated by intense X-ray laser radiation. *High Energy Density Physics*, 7(3):111–116, 2011. 114, 120

[102] S Düsterer, P. Radcliffe, C. Bostedt, J. Bozek, A. L. Cavalieri, et al. Femtosecond x-ray pulse length characterization at the Linac Coherent Light Source free-electron laser. *New Journal of Physics*, 13(9):093024, 2011. 114, 120

[103] Robin S. Marjoribanks, Fredric Budnik, Gabor Kulcsar, and Liang Zhao. Isoelectronic line intensity ratios for plasma electron temperature measurement (invited). *Review of Scientific Instruments*, 66(1):683, 1995. 121

[104] Siegfried Glenzer and Ronald Redmer. X-ray Thomson scattering in high energy density plasmas. *Reviews of Modern Physics*, 81(4):1625–1663, 2009. 121

[105] Carlos A. Iglesias and Stephanie B. Hansen. Fe xvii Opacity at Solar Interior Conditions. *The Astrophysical Journal*, 835(2):284, 2017. 122

[106] P. Beiersdorfer, E. W. Magee, G. V. Brown, H. Chen, J. Emig, et al. Lineshape spectroscopy with a very high resolution, very high signal-to-noise crystal spectrometer. *Review of Scientific Instruments*, 87(6):063501, 2016. 122

[107] F. Pérez, G. E. Kemp, S. P. Regan, M. A. Barrios, J. Pino, et al. The NIF x-ray spectrometer calibration campaign at Omega. *Review of Scientific Instruments*, 85(11):11D613, 2014. 122

[108] R. C. Mancini, H. M. Johns, T. Joshi, D. Mayes, T. Nagayama, et al. Multiple-view spectrally resolved x-ray imaging observations of polar-direct-drive implosions on OMEGA. *Physics of Plasmas*, 21(12), 2014. 122, 123

[109] P. Beiersdorfer, G. V. Brown, R. Shepherd, P. Allan, C. R D Brown, et al. Lineshape measurements of He- β spectra on the ORION laser facility. *Physics of Plasmas*, 23(10):101211, 2016. 122

[110] M A Barrios, D A Liedahl, M B Schneider, O Jones, G V Brown, et al. Electron temperature measurements inside the ablating plasma of gas-filled hohlraums at the National Ignition Facility. *Physics of Plasmas*, 23(5):056307, 2016. 123